INFORMATION TO USERS

This reproduction was made from a copy of a document sent to us for microfilming. While the most advanced technology has been used to photograph and reproduce this document, the quality of the reproduction is heavily dependent upon the quality of the material submitted.

The following explanation of techniques is provided to help clarify markings or notations which may appear on this reproduction.

1. The sign or "target" for pages apparently lacking from the document photographed is "Missing Page(s)". If it was possible to obtain the missing page(s) or section, they are spliced into the film along with adjacent pages. This may have necessitated cutting through an image and duplicating adjacent pages to assure complete continuity.
2. When an image on the film is obliterated with a round black mark, it is an indication of either blurred copy because of movement during exposure, duplicate copy, or copyrighted materials that should not have been filmed. For blurred pages, a good image of the page can be found in the adjacent frame. If copyrighted materials were deleted, a target note will appear listing the pages in the adjacent frame.
3. When a map, drawing or chart, etc., is part of the material being photographed, a definite method of "sectioning" the material has been followed. It is customary to begin filming at the upper left hand corner of a large sheet and to continue from left to right in equal sections with small overlaps. If necessary, sectioning is continued again—beginning below the first row and continuing on until complete.
4. For illustrations that cannot be satisfactorily reproduced by xerographic means, photographic prints can be purchased at additional cost and inserted into your xerographic copy. These prints are available upon request from the Dissertations Customer Services Department.
5. Some pages in any document may have indistinct print. In all cases the best available copy has been filmed.

University
Microfilms
International

300 N. Zeeb Road
Ann Arbor, MI 48106

8312380

Wicksted, James Peter

RESONANT BRILLOUIN SCATTERING STUDIES OF THE A-EXCITON IN CADMIUM SULPHIDE

City University of New York PH.D. 1983

University
Microfilms
International 300 N. Zeeb Road, Ann Arbor, MI 48106

RESONANT BRILLOUIN SCATTERING STUDIES OF THE A-EXCITON IN CADMIUM SULPHIDE

by

JAMES PETER WICKSTED

A dissertation submitted to the Graduate
Faculty in Physics in partial fulfillment
of the requirements for the degree of
Doctor of Philosophy, The City University
of New York.

1983

This manuscript has been read and accepted for the Graduate Faculty in Physics in satisfaction of the dissertation requirement for the degree of Doctor of Philosophy.

December 15, 1982
date

Chairman of Examining Committee

Dec 15, 1982
date

Executive Officer

Joseph L. Birman
Prof. Joseph L. Birman, CCNY

Robert Callender
Prof. Robert Callender, CCNY

Micha Tomkiewicz
Prof. Micha Tomkiewicz, Brooklyn

Rhoda Berenson
Prof. R. Berenson, Nassau Community

Supervisory Committee

THE CITY UNIVERSITY OF NEW YORK

Abstract

RESONANT BRILLOUIN SCATTERING STUDIES OF THE A-EXCITON IN CADMIUM SULPHIDE

by

James Peter Wicksted

Adviser: Professor Herman Z. Cummins

High resolution resonant Brillouin scattering was performed in the vicinity of the A-exciton in cadmium sulphide. The experimental arrangement, which consisted of a single mode dye laser, triple-pass Fabry-Perot interferometer and a grating spectrometer, enabled Brillouin shift, linewidth and intensity measurements to be made on multi-Brillouin components. These components result from the scattering between acoustic phonons and propagating exciton-polariton modes in the crystalline medium.

In an attempt to identify the correct additional boundary condition (ABC) which is needed in describing the simultaneous propagation of two exciton-polariton modes, a theoretical external differential scattering cross section calculation was developed via a factorization procedure. This calculation allowed a quantitative comparison between experiment and theory.

The important results of this research are now given.

1. The observation of the inner polariton branch participating in the one phonon scattering processes [both interbranch (1-2'), (2-1') and intrabranch (1-1')] between exciton-polaritons and acoustic phonons. These additionally observed Brillouin components have resulted in revised values for the A-exciton parameters.

2. Broadening of both the Stokes LA (2-2') and TA (2-2') linewidths has been observed as a function of incident laser frequency. These measurements, however, suggest that the exciton damping parameter, Γ, may not be a constant but instead a monotonically increasing function of incident frequency ω_I for $\omega_I > \omega_T$.

3. Comparisons between the experimental intensity measurements and the theoretical external scattering cross sections for both Stokes LA (2-2') and TA (2-2') components suggest that the additional boundary condition formulated by Ting et al(23) results in the best agreement between experiment and theory.

4. The intensity ratio between the Stokes LA (1-1') component and the Stokes LA (2-2') component is 100 times smaller than theoretically predicted even though the general trend of the LA (1-1') intensity as a function of incident frequency follows these same theoretical predictions for any of the three ABCs.

5. Least square fits between theoretical and experimental reflectivity expressions were also made. Each ABC results in a reasonably good fit with experiment when a dead layer is included in the analysis.

ACKNOWLEDGEMENTS

I am indebted to Professor Herman Z. Cummins for his continued support, encouragement and patient guidance during the course of this research.

I am extremely grateful to Dr. Mitsugu Matsushita for his assistance in all the resonant Brillouin scattering (RBS) experiments. In addition, I acknowledge the diligent work Dr. Matsushita performed on the construction of a theoretical scattering efficiency calculation which has been used in this thesis for comparison with the experimental RBS results.

I am also grateful to Dr. Takeshi Shigenari for both his help with the reflectivity experiments and his analysis of the data.

I thank Professor J. L. Birman and Dr. Ashok Puri for many helpful discussions on the theory of RBS.

I acknowledge the friendship and assistance of former members of this light scattering group: Drs. M. Matsushita, E. S. Koteles, W. Yao, R. G. Waters, M. Copic, J. S. Hwang and B. Y. Gu.

I am pleased and privileged to have known the current members of the light scattering group: Drs. Dennis Neal and Takeshi Shigenari, Mr. Mohammed Awal, Mr. Oscar Mesquita, Mr. Xing-Ze Lu and Mr. Shen-Li Qiu. Their help and encouragement, especially during the writing of this dissertation, was truly appreciated.

Special thanks are also given to Mrs. Frances Tritt and my sister, Diane Wicksted, for typing this thesis.

TO MY MOTHER, HELEN WICKSTED, MY SISTER, DIANE,
MY FAMILY AND FRIENDS

IN MEMORY OF MY FATHER, JAMES C. WICKSTED

TABLE OF CONTENTS

Chapter | Page

ABSTRACT iii

ACKNOWLEDGEMENTS v

LIST OF TABLES xiii

LIST OF FIGURES xiv

I. INTRODUCTION 1

- A. THE POLARITON CONCEPT 1
- B. SPATIAL DISPERSION 2
  - 1. Definition and the Non-Local Response of the Medium 2
  - 2. Excitonic Spatial Dispersion and the Necessity of an Additional Boundary Condition 3
- C. ADDITIONAL BOUNDARY CONDITIONS 4
- D. RESONANT BRILLOUIN SCATTERING 8
  - 1. Prediction of the Theory 8
  - 2. Previous RBS Experiments 9
    - a. Zincblende Structure 9
    - b. Wurtzite Structure 11
    - c. Other Crystal Structures 13
- E. PRESENT STUDY - CdS 14
- F. CONTENTS OF OTHER CHAPTERS 15

II. CdS STRUCTURE AND PROPERTIES 17

- A. UNIT CELL, GROUP SYMMETRY AND THE CHARACTER TABLE 17
- B. NORMAL VIBRATIONAL MODES 17
- C. ENERGY BANDS 24

D. EXCITON STATES 30

1. Anisotropy 31

2. K-Linear Term Effects 31

3. Exchange Interaction Effects 32

III. SCATTERING OF POLARITON MODES VIA THERMALLY EXCITED ACOUSTIC MODE FLUCTUATIONS IN A LOCAL MEDIUM - CLASSICAL APPROACH 34

A. INTRODUCTION 34

B. LOCAL CLASSICAL OSCILLATOR MODEL IN AN ABSORBING MEDIUM 35

1. Electronic Motion 35

a. Equation of Motion 35

b. Complex Dielectric Function and the Polariton Dispersion Curves 38

2. Acoustic Modes 39

a. Acoustic Wave Equations 39

b. Acoustic Strain Linear Response Function 42

3. Coupling of the Polariton with the Strain 43

4. Internal Scattering Cross Section 45

C. TRANSMISSION OF THE ELECTROMAGNETIC WAVE BETWEEN VACUUM AND THE ABSORBING MEDIUM 46

1. Transmissivity and Reflectivity Expressions 46

a. Vacuum to Medium 46

b. Medium to Vacuum 48

D. EXTERNAL SCATTERING CROSS SECTION 49

IV. RESONANT SCATTERING OF EXCITON-POLARITONS VIA PHONONS IN SPATIALLY DISPERSIVE MEDIA-QUANTUM MECHANICAL APPROACH 50

- A. INTRODUCTION 50
- B. EXCITON THEORY 50
  - 1. The Hamiltonian 50
  - 2. Exciton Wavefunction and Energy Levels 51
  - 3. Application to the n = 1 A-Exciton in CdS 52
- C. EXCITON-POLARITON THEORY 56
  - 1. The Hamiltonian 56
  - 2. Exciton-Polariton Dispersion Equation 56
  - 3. Polariton-Phonon Interaction 58
    - a. General Expression 58
    - b. Deformation Potential Interaction 62
    - c. Piezoelectric Interaction 63
- D. RESONANT BRILLOUIN SCATTERING 64
  - 1. General Considerations 64
  - 2. Kinematics and the Brillouin Shift 65
  - 3. Transition Probability (Scattering Rate of Polaritons) 71
  - 4. Internal Scattering Cross Section 72
  - 5. External Scattering cross Section 72
    - a. General Expressions for the Three ABCs 72
    - b. Transmissivity and Reflectivity Expressions 74
    - c. External Scattering Cross Section Expression 76

V. EXPERIMENT 81

A. INTRODUCTION 81

B. RBS EXPERIMENTS 81

1. Experimental Setup 81

2. Apparatus 85

3. Experimental Procedure 90

C. REFLECTIVITY EXPERIMENTS 94

1. Experimental Setup 94

2. Experimental Procedure 97

VI. RESULTS 99

A. INTRODUCTION 99

B. RBS RESULTS 99

1. Brillouin Shifts 99

2. Brillouin Linewidths 100

3. External Scattering Cross Sections 107

C. REFLECTIVITY RESULTS 124

D. ABSORPTION MEASUREMENTS 126

VII. DISCUSSION 141

A. INTRODUCTION 141

B. DISCUSSION OF THE RBS RESULTS 141

C. DISCUSSION ON THE REFLECTIVITY RESULTS 143

D. GENERAL REMARKS 144

E. SUMMARY OF RESULTS AND POSSIBLE EXTENSIONS OF THE THEORETICAL CALCULATIONS AND EXPERIMENTAL INVESTIGATIONS 154

VIII. APPENDIX 158

IX. REFERENCES 161

LIST OF TABLES

Table		Page
2-1	Character Table and Basis Functions for the Group C_{6v}	20
2-2	Frequencies (cm^{-1}) of Normal Optic Modes in CdS	21
2-3	Elastic Stiffness Constants for C_{6v} Symmetry	25
2-4	Scattering Tensor, Eigenvalues and Eigenvectors of Phonons Traveling in the Direction $\hat{q}$ in the Hexagonal Crystal Class C_{6v}	26
2-5	Brillouin Scattering Tensor Components of a Wurtzite Crystal for Light Incident Along [100] and Scattered Along [100] with Phonon Propagation Along [100]	27
2-6	Piezoelectric Constants for C_{6v} Symmetry	28
4-1	Values of the n= 1 A-Exciton in CdS for $k \perp c$	53
5-1	List of Apparatus	86
6-1	Best Fit Values of the Exciton Parameters for the n = 1 A-Exciton in CdS	137
6-2	Values Used in the Expressions for the Deformation Potential and Piezoelectric Interactions	138
6-3	Values Used for the Classical Oscillator Description of the B-Exciton	139
6-4	Best Fit Values for Γ and $\bar{\varepsilon}_b$ Resulting from the Reflectivity Analysis for Each of the Three ABCs	140
7-1	Best Fit Values for Γ, $\bar{\varepsilon}_b$, ℓ and n Resulting from the Reflectivity Analysis for Each of the Three ABCs	157

LIST OF FIGURES

Figure Page

2-1 Unit Cell of CdS 19

2-2 Band Structure of CdS 29

2-3 Exciton Levels of the n = 1 A-Exciton in CdS as a Function of the Direction of $\vec{k}$ 33

3-1 Schematic Representation of a Backward RBS Experiment Involving a Semi-Infinite, Isotropic, Homogeneous, Absorbing Local Medium 36

3-2 Schematic Diagram of the Transverse Polariton Dispersion Curves in a Local Medium 40

4-1 Schematic Representation of a Backward RBS Experiment Involving a Semi-Infinite Spatially Dispersive Medium 54

4-2 Schematic Diagram of the Transverse Exciton-Polariton Dispersion Curves in a Spatially Dispersive Medium 59

4-3 Exciton Strength Functions for Both Mode-1 and Mode-2 Polaritons as a Function of Incident Frequency 67

4-4 Schematic Representation of the Exciton-Polariton Dispersion Curves and the Kinematics Involved in a Backward RBS Experiment 69

4-5 Numerically Calculated Vacuum to Medium Transmissivities of Mode-1 and Mode-2 Polaritons for Various ABCs as a Function of Incident Frequency 77

4-6 Transmissivity Product of the Incident and Scattered Mode-2 Polaritons as a Function of Incident Frequency 79

Figure Page

5-1 Schematic of RBS Experimental Arrangement 83

5-2 Comparative Illustration Showing a Brillouin Spectrum Analyzed with; (a) Double-Grating Spectrometer and (b) Fabry-Perot Interferometer and Grating Spectrometer in Series 92

5-3 Schematic of Reflectivity Experimental Arrangement 95

6-1 Brillouin Spectrum of CdS with Incident Frequency ω_I Equal to 20612.3 cm^{-1} 101

6-2 Brillouin Spectrum of CdS with Incident Frequency ω_I Equal to 20613.6 cm^{-1} 103

6-3 Brillouin Shifts of Observed One Phonon Stokes and Anti-Stokes Peaks as a Function of Incident Frequency 105

6-4 Approximate Experimental Linewidths of the Stokes TA (2-2') Brillouin Components as a Function of Incident Frequency 108

6-5 Digitally Recorded Brillouin Spectrum Showing Both Rayleigh and Stokes Brillouin Lines Fitted to Lorentzian Lineshapes 110

6-6 Log_{10} Illustration of the Theoretical Internal and External Scattering Cross Sections for LA (2-2') Scattering as a Function of Incident Frequency ω_I 114

6-7 Log_{10} Illustration of the Theoretical Internal and External Scattering Cross Section for the TA (2-2') Scattering as a Function of Incident Frequency ω_I 116

Figure Page

6-8 Log_{10} Comparison of the Theoretical External Scattering Cross Section for the Stokes LA(2-2') Scattering for Various ABCs with the Experimentally Measured Brillouin Intensity 118

6-9 Log_{10} Comparison of the Theoretical External Scattering Cross Section for the Stokes TA(2-2') Scattering for Various ABCs with the Experimentally Measured Brillouin Intensity 120

6-10 Log_{10} Comparison of the Theoretical External Scattering Cross Section for the Stokes LA(1-1') Scattering for Various ABCs with the Experimentally Measured Brillouin Intensity 122

6-11 Non-Linear Least Squares Fit of the Theoretical Reflectivity Expression Using ABC1 to the Experimental Reflectivity Expression 127

6-12 Non-Linear Least Squares Fit of the Theoretical Reflectivity Expression Using ABC2 to the Experimental Reflectivity Expression 129

6-13 Non-Linear Least Squares Fit of the Theoretical Reflectivity Expression Using ABC3 to the Expreimental Reflectivity Expression 131

6-14 Comparison Between Theoretical and Experimental Optical Density Expressions 135

Figure Page

7-1 Non-Linear Least Square Fit of the Theoretical Reflectivity Expression Using ABC1 Plus a Dead Layer to the Experimental Reflectivity Expression 145

7-2 Non-Linear Least Square Fit of the Theoretical Reflectivity Expression Using ABC2 Plus a Dead Layer to the Experimental Reflectivity Expression 147

7-3 Non-Linear Lest Square Fit of the Theoretical Reflectivity Expression Using ABC3 Plus a Dead Layer to the Experimental Reflectivity Expression 149

7-4 Log_{10} Comparison of the Theoretical External Scattering Cross Section for the Stokes LA (2-2') Scattering Using Various ABCs and Assuming a Constant Deformation Potential Interaction with the Experimentally Measured Brillouin Intensity 151

CHAPTER I

INTRODUCTION

In 1972, Brenig, Zeyher and Birman(1) (BZB) extended the theory of resonant Raman scattering to include light scattering from acoustic phonons by considering the role of exciton-polaritons as intermediate states for Brillouin scattering occurring near an exciton resonance. This theory, known as resonant Brillouin scattering (RBS), opened new fields of research on crystals which exhibit spatial dispersion. Subsequent experiments were quite successful in illustrating many of the kinematic predictions of the theory. However, other important theoretical results concerned with polariton life-times and additional boundary conditions (ABC) remained experimentally unresolved.

The present research discussed in this thesis is experimentally designed to explore these additional results of the theory in the wurtzite semiconductor cadmium sulphide. This is made possible by the incorporation of higher resolution apparatus into the RBS experiments.

Before continuing with the theoretical and experimental discussions on RBS, some introductory discussion is necessary concerning the polariton concept, spatial dispersion, and the necessity of an additional boundary condition.

A. THE POLARITON CONCEPT(2,3)

Polaritons are composite quasi-particles which are formed by the coupling of light to polarization modes in a dielectric medium. Two examples of the polarization (crystalline) modes are phonons and excitons.

Huang(4) in 1951 and Poulet(5) in 1955 explored the mixing of electromagnetic waves with polar optical phonons classically. A quantum mechanical treatment was given in 1956 by Fano.(6) In 1958, the bilinear coupling between photons and stationary (infinite mass) excitons was carried out via second quantization theory by Hopfield.(7) The coupling of photons to propagating excitons was first treated quantum mechanically by Pekar(8) in 1957 and later treated classically by Hopfield and Thomas(9) in 1963.

The subject of polariton-mediated light scattering has been discussed in several review articles.(10-14) In this thesis, the scattering of acoustic phonons by photon-exciton polaritons in the vicinity of an exciton resonance will be studied. Such scattering processes are particularly interesting when the excitons considered have finite effective mass. In this case, the exciton energy dispersion results in the medium becoming strongly spatially dispersive.

B. SPATIAL DISPERSION(2)

1. Definition and the Non-local Response of the Medium

The variation of the susceptibility (or dielectric) tensor of a medium with wavevector is referred to as spatial dispersion.

Consider an electromagnetic wave of frequency ω and wavevector $\vec{k}$ propagating in such a medium which is also assumed to be homogeneous, linear and isotropic. The induced polarization $\vec{P}\ (\vec{k}, \omega)$ can be related to the electric field $\vec{E}\ (\vec{k}, \omega)$ of the wave through the susceptibility

$$\vec{P}\ (\vec{k},\omega) = \chi(\vec{k},\omega)\ \vec{E}\ (\vec{k},\omega) \tag{1.1}$$

The physical significance of the dependence of the susceptibility on $\vec{k}$ can be seen by first writing

$$\vec{E}(\vec{x},\omega) = \int\frac{d\vec{k}}{(2\pi)^3} \quad \vec{E}(\vec{k},\omega) \exp\,(i\vec{k}\cdot\vec{x}) \tag{1.2}$$

which is the electric field at position $\vec{x}$ in the medium. If a similar expression is assumed for $\vec{P}(\vec{x},\omega)$ and if we let

$$\chi(\vec{x}-\vec{x}',\omega) = \int\frac{d\vec{k}}{(2\pi)^3} \quad \chi(\vec{k},\omega) \exp\,[i\vec{k}\cdot(\vec{x}-\vec{x}')] \tag{1.3}$$

then Eq. (1.1) becomes

$$\vec{P}\,(\vec{x},\omega) = \int d\vec{x}' \quad \chi(\vec{x}-\vec{x}',\omega) \quad \vec{E}(\vec{x}',\omega) \tag{1.4}$$

This result imples that if χ depends on k, then the polarization at $\vec{x}$ depends not only on the magnitude of the electric field at $\vec{x}$ but also on the value of the field in a neighborhood surrounding $\vec{x}$. Thus, the spatially dispersive medium exhibits a non-local response to the electric field.

2. Excitonic Spatial Dispersion and the Necessity of an Additional Boundary Condition

In 1957, Pekar$^{(8)}$ investigated the effects of excitonic spatial dispersion in crystalline solids. Utilizing the wavevector dependent kinetic energy expression of an exciton with finite translational effective mass, Pekar developed a differential equation of motion for the polarization of a single dipole active exciton:

$$\left(\frac{\partial^2}{\partial t^2} + \omega_o - \frac{\hbar\omega_o}{m^*}\nabla^2 + \Gamma\,\frac{\partial}{\partial t}\right) \vec{P}(\vec{x},t) = \alpha_o\omega_o^2\,\vec{E}(\vec{x},t) \tag{1.5}$$

where m* is the effective translational mass of the exciton and $\vec{E}(\vec{x},t)$ is a macroscopic electric field which drives the polarization. The other parameters ω_o, Γ, α_o are the exciton resonance frequency, damping constant and oscillator strength respectively. Assuming plane wave solutions for $\vec{P}$ and $\vec{E}$, Eq. (1.5) results in an expression equivalent to Eq. (1.1) with the non-local susceptibility (known as the dielectric approximation model)(9) given by

$$\chi(\vec{k},\omega) = \chi_b + \frac{\alpha_o\omega_o^2}{\omega_o^2-\omega^2+\frac{\hbar\omega_o}{m^*}k^2-i\omega\Gamma} \qquad (1.6)$$

where χ_b is a background susceptibility. The combination of Eq. (1.6) with Maxwell's equations results in the exciton-polariton dispersion curves which will be discussed in detail in Chap. IV..

As Pekar originally discovered, two propagating polariton modes can simultaneously exist in a spatially dispersive medium with the same frequency and polarization (see Fig. 4-2). For light normally incident on the boundary of this medium with frequency $\omega>\omega_L$, the amplitudes of these two transmitted polariton modes and of the reflected wave cannot be ascertained solely from Maxwell's boundary conditions. An additional boundary condition (ABC) is needed to determine the amplitudes of the two transmitted modes.

C. ADDITIONAL BOUNDARY CONDITIONS(15)

A brief history on the origin of the three most frequently discussed ABCs will now be given.

The first ABC, present by Pekar,(8) is based on the condition that the total exciton polarization must vanish at the crystal boundary:

$$\sum_{i=1}^{2} P_{Ex_i} = 0 \text{ at } x = 0 \qquad (1.7)$$

where the x-axis is perpendicular to the crystal surface, and P_{Ex_i} denotes the exciton polarization associated with the $i^{\underline{th}}$ transmitted wave. Pekar asserted that Eq. (1.7) should be the ABC to supplement the Maxwell boundary conditions after showing that the crystal boundaries turned out to be nodal surfaces for the exciton wavefunction, as well as for the dipole moment associated with the exciton.

The first experimental evidence of an excitonic spatially dispersive medium was observed in reflectivity measurements performed by Hopfield and Thomas(9) at the n=1 A-exciton state in cadmium sulphide. The low reflectivity maximum observed in these studies in addition to the anomalous spike seen near the longitudinal exciton frequency could not be explained by the simple classical dielectric model (this model is represented by Eq. (1.6) with m* set equal to infinity). These authors then incorporated spatial dispersion into their analysis by utilizing the dielectric approximation for the nonlocal susceptibility along with the Pekar ABC [Eqs. (1.6) and (1.7)]. They also incorporated a "dead" layer into their analysis. This "dead" layer was considered to be an approximation of a repulsive image potential that an exciton encounters as it approaches the crystal surface and, thus, a region in which the exciton could not exist. Using this approach, a very clear account of the anomalous structure seen in the CdS reflectivity could be given. [However, it should be noted that reflectivity experiments are very sensitive to the crystal surface quality. For example, certain samples have shown the anomalous spike while others have not.(16)]

Subsequently, Birman and Sein,(17) Maradudin and Mills,(18) Agrawal et al(19) and others(20,21) independently explored the ABC problem with Maxwell's equations rather than from a phenomenological approach. These groups discovered that once a particular non-local susceptibility is chosen, the resulting ABC can be determined through either an integral or differential equation formulation of the electrodynamics of the non-local medium with no further assumptions being necessary. For example, when the dielectric approximation for the susceptibility [Eq. (1.6)] is chosen, the resulting ABC is(17-19)

$$\sum_{i=1}^{2} \frac{P_{Ex_i}}{(n_{c_i}-n_e)(n_{c_i}^2-\varepsilon_b)} = 0 \quad \text{at } x = 0 \qquad (1.8)$$

where n_{c_i} is the refractive index of the $i^{\underline{th}}$ transmitted polariton mode, ε_b is a background dielectric constant and

$$n_e \equiv \frac{1}{\omega} \left[\frac{m^* c^2}{\hbar\omega_o} \{\omega^2-\omega_o^2 + i\omega\Gamma\}\right]^{1/2}$$

where n_e is just the refractive index for the uncoupled exciton. It should therefore be noted that the ABC given by Pekar in Eq. (1.7) is not a mathematical consequence of the dielectric approximation given by Eq. (1.6).

A more microscopic approach for finding ABCs was given by Zeyher et al(22) in 1972. This approach suggested that different ABCs for exciton-polaritons can arise from different assumptions about the reflection of an exciton at the crystal surface. The wavefunction describing the center of mass motion of the exciton can be approximately expressed as:

$$\Psi_{\vec{k}}\ (\vec{r},\omega) \sim \theta(x)\ \ [e^{ik_x x} + r_e\, e^{-ik_x x}]\ e^{ik_y y}\ e^{ik_z z} \qquad (1.9)$$

where r_e is the exciton reflection coefficient and $\theta(x)$ is a step function. These authors showed that for tightly bound (Frenkel) excitons which are totally reflected from the crystal surface, $r_e = -1$ and the ABC which was originally proposed by Pekar [Eq. (1.7)] is obtained. However, for excitons absorbed at the crystal surface, $r_e = 0$ and the ABC given in Eq. (1.8) results. Ting et al$^{(23)}$ showed that for Wannier excitons whose wave-functions can be approximated by letting $r_e = 1$ in the above expression, the following ABC results:

$$\sum_{i=1}^{2} n_{c_i} P_{Ex_i} = 0 \quad \text{at } x=0 \qquad (1.10)$$

The three abcs [Eqs. (1.7), (1.8), (1.10)] are now listed below and expressed in terms of the electric field amplitudes E_i associated with the two transmitted polariton modes:

ABC 1 [Pekar;$^{(8)}$ Zeyher, Brenig and Birman$^{(22)}$]

$$\sum_{i=1}^{2} (n^2_{c_i} - \varepsilon_b)\ \ E_i = 0 \qquad (1.11)$$

ABC 2 [Ting, Frankel and Birman;$^{(23)}$ Agranovich and Ginzburg$^{(20)}$]

$$\sum_{i=1}^{2} n_{c_i}(n^2_{c_i} - \varepsilon_b)\ E_i = 0 \qquad (1.12)$$

ABC 3 [Birman and Sein;(17) Agrawal, Pattanayak and Wolf;(19) Maradudin and Mills(18)]

$$\sum_{i=1}^{2} \frac{E_i}{(n_{c_i}-ne)} = 0$$

$$n_e \equiv \frac{1}{\omega} \left[\frac{m^*c^2}{\hbar\omega_o} \{\omega^2-\omega_o^2+i\omega\Gamma\}\right]^{1/2} \qquad (1.13)$$

D. RESONANT BRILLOUIN SCATTERING

1. Predictions of the Theory

The predictions of the resonant Brillouin scattering theory presented by Brenig, Zeyher and Birman(1) will now be given with the use of Fig. 4-4. The upper (1) and lower (2) dispersion curves shown in this figure are the two exciton-polariton branches. The derivation of the exciton-polariton dispersion relation resulting in these curves along with the discussion of the Brillouin scattering kinematics will be given in Chap. IV.

As the incident laser frequency ω_I is scanned upwards through the exciton resonance, (i) there should be a rapid increase in Brillouin shift due to the curvature of the lower polariton branch near ω_o in addition (ii) to an increase in the Brillouin linewidth, while for ω_I above the onset of the upper polariton branch ($\omega_I>\omega_2$), (iii) a Brillouin octet resulting from intermediate states on both exciton-polariton branches replaces the usual Brillouin doublet which is observed well below ω_o. It should be noted that since the two polariton branches are very sensitive to the exciton parameters (see Chap. IV) the dependence of the Brillouin shifts and widths on incident frequency should also be very sensitive to these parameters - the former particularly on the exciton mass and the latter on the exciton damping constant. The damping constant value is important in the estimation of polariton lifetimes. Finally, (iv) the scattering cross section for the different Brillouin components should be sensitive to the ABCs and be strongly frequency dependent in the exciton resonance region.

2. Previous RBS Experiments(11-13)

I will now briefly summarize previous RBS experiments performed on crystals of various crystal structures. It should be noted from the discussion in the preceding subsection, that the experimental measurements of Brillouin shifts and widths as functions of frequency will result in values for the exciton parameters while cross section measurements should provide information concerning ABCs.

a. Zincblende Structure

In 1977, Ulbrich and Weisbuch(24) employed a tunable near-infrared dye laser as an exciting source to study the 1S exciton resonance formed by the Γ_6 conduction band and Γ_8 valence band in the III-V compound gallium arsenide. Utilizing a [100] backscattering configuration and analyzing the scattered light with a grating spectrometer, they were able to observe near resonance, the enhancement of the Brillouin intensity, the Brillouin shift dispersion and the multi-Brillouin components resulting from the interbranch and intrabranch longitudinal acoustic (LA) phonon scattering between two exciton-polariton branches. A two branch model was also used to explain the RBS experiments performed in the [110] direction where now both transverse and longitudinal phonon scattering between polariton branches was observed, although the former (TA) is normally "forbidden" by deformation potential section rules. Similar results, by the same group, were obtained from the RBS experiments performed on the II-VI compound CdTe.(11)

A three polariton branch model, however, was needed to explain the RBS data obtained from the semiconductor ZnSe. Sermage and Fishman,(25) also utilizing a tunable dye laser and a grating spectrometer, performed RBS experiments in both [100] and [110] backscattering configurations, the latter direction once again showing both TA and LA phonon participation.

For crystals of zincblende structure, the degenerate Γ_8 valence band results in two distinct exciton bands, each of which can couple with an incoming photon yielding overall a three exciton-polariton branch system. These two excitons are distinguishable via their effective translational masses, one exciton having a larger mass than the other. Both of these "light" and "heavy" excitons have been observed to participate in the RBS data of ZnSe. However, only the heavy exciton contributes to the RBS process in GaAs.

It should be also be noted that only one phonon scattering processes were observed in all the RBS data on cubic zincblende crystals.

b. Wurtzite Structure

Perhaps the crystal which has had its Raman and Brillouin components most extensively studied in the region of an exciton resonance is the II-VI semiconductor CdS. Even prior to the RBS predictions by BZB, Pine(26) had investigated the Brillouin spectrum of CdS by temperature tuning its 1S A-exciton toward a fixed-frequency (6323A°) laser. He observed a strong resonance enhancement in the LA Brillouin cross section as the frequency of this exciton was lowered (via increasing crystal temperature) towards the laser frequency. This temperature tuning technique was also utilized by Bruce and Cummins(27) who observed both resonant dispersion and enhancement of the LA Brillouin component while the A-exciton's frequency was lowered toward the 4880A° line of an argon laser. However, the two branch features predicted by BZB could not be observed due to severe broadening effects at the temperature required to achieve resonance. Both of these studies used Fabry-Perot interferometry to analyze the scattered light.

In 1977, Winterling and Koteles(28) utilized an experimental setup similar to the one used in the GaAs studies (dye laser and grating spectrometer) to perform RBS experiments from both the n=1 A and B-exciton resonances in CdS. For the A-exciton, both LA and TA phonons were observed in the backscattering setup used with incident laser wavevector perpendicular to the hexagonal c-axis. Only intrabranch scattering involving the outer exciton-polariton branch could be observed in these one phonon scattering processes. Inner branch participation, however, was witnessed in a two-phonon scattering process(29) which occurred when the incident laser frequency was above the longitudinal exciton frequency. These two-phonon effects are possible due to the anisotropic and piezoelectric properties of CdS (the latter effect also being responsible for the observation of the "forbidden" TA phonon which was first observed in CdS(30) - see Chap. II, Sec. B). The B-exciton was also investigated by this same group.(31) These RBS experiments proved to be extremely interesting since this exciton resonance was shown to exhibit either a two or three branch behavior for the incident laser light polarized either parallel or perpendicular to the crystal c-axis. This three branch behavior results from terms linear in wavevector in the B-exciton energy which produces a mixing among its ground states. As in the A-exciton case, both TA and LA one phonon scattering was observed, although no two phonon scattering processes were seen.

Yu and Evangelisti(32) have also carried out an investigation of RBS in CdS. They have considered the role of the ABCs in determining the cross section, as proposed by BZB, and have suggested a new model for the CdS surface including, following Hopfield and Thomas, a surface "dead layer" with a large damping constant with which they were able to fit their cross section data reasonably well.

Broser and Rosenzweig(33) have recently performed RBS experiments on CdS while the crystal was subjected to high magnetic fields ($\vec{H} \perp \hat{c}$).

Due to the field induced mixing and splitting of the allowed $\Gamma_5{}^T$ and forbidden Γ_6 states of the A-exciton (see Chap. II, Sec. D) a three polariton branch model was used to fit the Brillouin shift data. The LA Stokes line corresponding to outer branch scattering at $H = 0$ was seen to split into three sub-lines with increasing magnetic field. For a fixed field, the Brillouin shifts of these three lines were theoretically fitted by considering interbranch and intrabranch LA phonon scattering between the two outer polariton branches only. These fits resulted in the determination of the singlet ($\Gamma_5{}^T$) – triplet (Γ_6) energy splitting. Corresponding splitting of the TA Stokes-line could not be resolved in these experiments.

Cadmium selenide is another II-VI wurtzite semiconductor in which RBS has been investigated by Hermann and Yu.(34) In addition to observing similar LA and TA scatterings as in the case of CdS, non-wavevector conserving scattering processes involving defects were also observed near the A-exciton in CdSe. No two phonon scattering processes were observed, however. A two branch model was used to fit the measured Brillouin shifts which resulted solely from outer polariton branch scatterings.

c. Other Crystal Structures

The layered semiconductor HgI_2 was investigated near its A-exciton by Goto and Nishina.(35) This semiconductor, like CdS, is highly anisotropic with single LA phonon scattering being observed in the [001] direction while both LA and TA scattering processes were witnessed in the [201] direction. All Brillouin shift data was fitted using a two-branch model.

The n = 2 P yellow exciton state in the cubic crystal Cu_2O has recently been investigated by So(36) using RBS. This exciton state, however, is only weakly dipole allowed and does not couple very strongly to photons. Only the photon-like inner polariton branch was observed throughout the resonance region of this exciton state.

E. PRESENT STUDY - CdS

The motivation to study CdS stems from past RBS and reflectivity experiments which were described earlier in this chapter. These studies have illustrated very clearly the spatial dispersive features associated with the A (as well as the B) exciton.

The purpose of the current research will now be discussed. First, it should be noted that most of the RBS experiments reviewed in Sec. D employed a grating spectrometer for the spectral analysis of the scattered light which precluded measurements of linewidth. Additionally, for CdS, no inner polariton branch participation was observed in the one-phonon RBS spectra. In order to extend these previous RBS investigations, higher resolution is clearly desirable. This can be accomplished by placing a triple pass Fabry-Perot interferometer in series with a tandem grating spectrometer. A single mode dye laser is used to excite the exciton resonance while the crystal temperature is maintained at 4.2°K in order to reduce phonon related broadband background emission. Using this experimental technique, accurate measurements of

Brillouin shifts resulting from scattering between both polariton branches can be obtained, yielding more accurate determinations of the exciton parameters (e.g., effective mass, transverse frequency, LT splitting). In addition, linewidth measurements of various Brillouin components can be recorded yielding information on polariton lifetimes.

Second, the work of Yu and Evangelisti can be extended by measuring both reflectivity and Brillouin scattering spectra from the same CdS sample, as was previously done by Bruce and Cummins. Since the electromagnetic boundary conditions enter into both the reflectivity and the Brillouin scattering cross section, self consistent fits to both sets of data can provide a more rigorous test of proposed ABCs than can cross section data alone.

F. CONTENTS OF OTHER CHAPTERS

The properties of the CdS crystal, including its normal modes, energy levels and exciton series are discussed in Chap. II. In Chap. III, a polariton formed from the coupling between an eletromagnetic wave and a local polar electronic resonance is examined in a classical dielectric medium. A nonlinear coupling between this polariton and the strain associated with a longitudinal acoustic mode is established. An expression for the internal differential scattering cross section describing the polariton-acoustic mode scattering process is obtained. A similar analysis is made in Chap. IV, but with the polariton-phonon scattering process occurring in a spatially dispersive medium and with a quantum mechanical (rather than classical) approach. In both chapters, the connection between the internal and external differential scattering cross sections is established via the factorization procedure:

$$\left(\frac{d\sigma}{d\Omega}\right)_{EXT} = \frac{T(\omega_I)T'(\omega_s)}{n_s^2\ (\omega_s)} \quad \left(\frac{d\sigma}{d\Omega}\right)_{INT} \tag{1.14}$$

Here $T(\omega_I)$ and $T'(\omega_s)$ are the incident and scattered transmissivity factors relating photons outside the crystal to polaritons inside. These factors are especially important for the spatially dispersive medium since they both are extremely sensitive to the ABCs. The $n_s^2(\omega_s)$ term in the denominator of Eq. (1.14) is the refractive index of the scattered polariton which results from the solid angle correction factor:

$$\left(\frac{d\Omega^{INT}}{d\Omega^{EXT}}\right) = \frac{1}{n_s^2(\omega_s)} \tag{1.15}$$

The experimental arrangements for the RBS and reflectivity experiments are described in Chap. V. In Chap. VI, the results of the RBS and reflectivity experiments performed near the A-exciton in CdS are presented. These results are then discussed in Chap. VII together with suggestions for future experiments.

CHAPTER II

CdS STRUCTURE AND PROPERTIES

A. UNIT CELL, GROUP SYMMETRY AND THE CHARACTER TABLE

Cadmium sulphide crystallizes in the wurtzite structure which belongs to the C_{6V}^{4} space group.(37) As shown in Fig. 2-1, the wurtzite unit cell contains four basis ions: two cadmium ions (cations) located at (0, 0, 0) and (a/3, 2a/3, c/2) and two sulphur ions (anions) located at (0, 0, u) and (a/3, 2a/3, u+c/2). The conventional hexagonal axes $(\hat{a}_1, \hat{a}_2, \hat{a}_3)$ have been used with lattice parameters $a = 4.16\text{Å}$, $c = 6.75\text{Å}$ and $u = 0.375c$. Each basis ion represents a hexagonal Bravais lattice where every cation has four anions as nearest neighbors positioned at the corners of a tetahedron. Both the cations and anions have site symmetry C_{3V}.

The symmetries of normal modes in the long wavelength limit, as well as the symmetries of electronic bands at the zone-center can be determined by neglecting translations and considering only the symmetry operations of the macroscopic point group C_{6V}. The effects of spin are described by the crystal double group, the character table of which is given in Table 2-1.

B. NORMAL VIBRATIONAL MODES

The presence of four ions per unit cell in CdS results in twelve normal vibrational modes. A group theoretical analysis using Table 2-1 predicts that the twelve Brillouin zone-center modes have the following symmetries: $2\Gamma_1 + 2\Gamma_4 + 2\Gamma_5 + 2\Gamma_6$. An inspection of the character table shows that both the components of a vector as well as the elements of the polarizability tensor transform according to the non-degenerate Γ_1 and the doubly degenerate Γ_5 representations. Two of these $(\Gamma_1 + \Gamma_5)$ account for all three acoustic modes, while the second pair accounts for both infrared and Raman active optic modes. Further inspection of the character table shows that the two doubly degenerate Γ_5 modes are also Raman active and the two Γ_4 modes are both infrared and Raman inactive.

The ionic displacement (phonon polarization) for the Γ_1 and Γ_2 modes is along the z-axis (c-axis), while for the doubly degenerate Γ_5 and Γ_6 modes the displacements are in the xy plane. The infrared active Γ_1 and Γ_5 modes result from the anions and cations moving in opposite phase, while the Γ_5 and Γ_2 modes result from like ions moving in opposite phase.

The frequencies of the normal optic modes$^{(40)}$ have been measured experimentally by infrared absorption,$^{(41)}$ infrared reflectivity,$^{(42)}$ fluorescence,$^{(43)}$ and Raman scattering.$^{(44)}$ The results of the Raman scattering experiments are shown in Table 2-2. Note that for infrared active modes (Γ_1 and Γ_5), the macroscopic electric field associated with the longitudinal phonons lifts the degeneracy of the transverse and longitudinal phonons.

The frequencies of the normal acoustic modes are very much smaller than those of the normal optic modes near the zone-center. Thus, the Brillouin spectrum is restricted to a spectral region which is much smaller than that of the Raman spectrum.

The properties of the long wavelength acoustic mode can be derived by considering the crystal as an elastic continuum and applying the classical theory of elasticity.$^{(45, 46)}$ The generalized Hooke's law relating the stress and strain tensors are:

$$S_{ij} = C_{ijk\ell}\, s_{k\ell} \qquad (i, j, k, \ell = 1, 2, 3) \qquad (2.1)$$

where the S_{ij} are the components of the second-rank stress tensor, $s_{k\ell}$ are the components of the second-rank strain tensor associated with the acoustic mode and $C_{ijk\ell}$ are the elastic stiffness constants. The

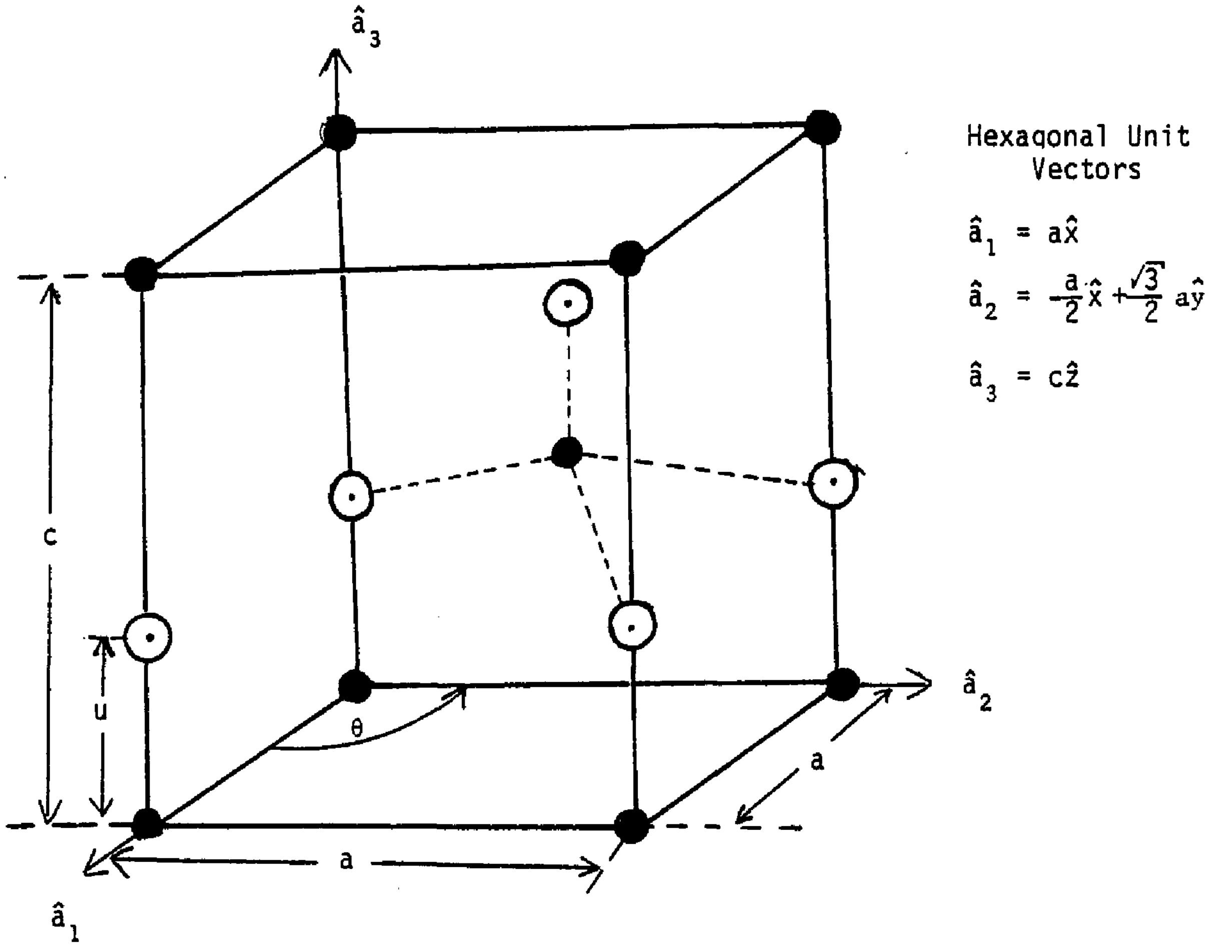

Hexagonal Unit Vectors

$\hat{a}_1 = a\hat{x}$

$\hat{a}_2 = -\frac{a}{2}\hat{x} + \frac{\sqrt{3}}{2}a\hat{y}$

$\hat{a}_3 = c\hat{z}$

Fig. 2-1 Unit cell of CdS

Structure: wurtzite

Space Group: C_{6v}^4

Lattice Parameters: $a = 4.16\text{Å}$ $c = 6.75\text{Å}$

$u \simeq 2.53\text{Å}$ $\theta = 120°$

Ions		Positions	Site Symmetries
2 Cadmium	●	(0,0,0)a, (a/3,2a/3,c/2)	C_{3v}
2 Sulfur	⊙	(0,0,u), (a/3,2a/3,u+c/2)	C_{3v}

TABLE 2-1 CHARACTER TABLE AND BASIS FUNCTIONS FOR THE GROUP C_{6V} [a]

Γ	E	$\bar{E}$	$\bar{C}_2$ C_2	$2C_3$	$2\bar{C}_3$	$2C_6$	$2\bar{C}_6$	$3\sigma_d$ $3\bar{\sigma}_d$	$3\sigma_v$ $3\bar{\sigma}_v$	Basis Functions	
Γ_1	1	1	1	1	1	1	1	1	1	x^2+y^2, z^2	z
Γ_2	1	1	1	1	1	1	1	-1	-1		R_z
Γ_3	1	1	-1	1	1	-1	-1	1	-1	x^3-3xy^2	
Γ_4	1	1	-1	1	1	-1	-1	-1	1	y^3-3yx^2	
Γ_5	2	2	-2	-1	-1	1	1	0	0	(xz,yz)	(x,y) (Rx,Ry)
Γ_6	2	2	2	-1	-1	-1	-1	0	0	x^2-y^2, xy	
Γ_7	2	-2	0	1	-1	$\sqrt{3}$	$-\sqrt{3}$	0	0	$\{\phi(\frac{1}{2},-\frac{1}{2}), \phi(\frac{1}{2},\frac{1}{2})\}$	
Γ_8	2	-2	0	1	-1	$-\sqrt{3}$	$\sqrt{3}$	0	0	$\Gamma_7 x \Gamma_3$	
Γ_9	2	-2	0	2	2	0	0	0	0	$\{\phi(\frac{3}{2},-\frac{3}{2}), \phi(\frac{3}{2},\frac{3}{2})\}$	

[a] Character table taken from Ref. 38, p. 67.

Basis function $\phi(J, m)$ means a function which transforms like an eigenstate of the angular momentum operator $\vec{J}$ of total angular moment J and z component m.

TABLE 2-2. FREQUENCIES (cm^{-1}) OF NORMAL OPTIC MODES

IN CdS (From Ref. 44)

Optic Mode		Frequency (cm^{-1})
($q \perp c$)	Γ_1 (TO)	228
($q \parallel c$)	Γ_1 (LO)	305
($q \perp c$ and $q \parallel c$)	Γ_5 (TO)	235
($q \perp c$)	Γ_5 (LO)	305
	Γ_6	44
	Γ_6	252

components of the strain are defined by

$$s_{k\ell} = \frac{1}{2}\left(u_{k\ell} + u_{\ell k}\right) \qquad (2.2)$$

where $u_{k\ell}$ is the gradient for the local displacement vector u_k.

The general form for the equation of motion of a displacement u_i in an elastic continuum is:

$$\rho \ddot{u}_i = C_{ijk\ell} \frac{\partial^2 u_k}{\partial x_j \partial x_\ell} \qquad (2.3)$$

where ρ is the crystal density and damping is ignored. We seek plane wave solutions for u_i of the form $\exp i(\vec{q}\cdot\vec{x} - \omega t)$:

$$\rho\omega^2 u_i = C_{ijk\ell}\, q_j u_k q_\ell \qquad (2.4)$$

For a particular crystal symmetry and a given direction for the wavevector q, the above equation can be diagonalized and will yield three velocity eigenvalues along with three displacement eigenvectors.

In the case of CdS, if we choose q to be in the x-direction, then with the help of Table 2-3, Eq. 2.4 simplifies to the following three uncoupled equations for u_1, u_2, u_3 (u_x, u_y, u_z):

$$\rho\omega^2 u_1 = C_{11} u_1 q_1^2 \qquad \text{(longitudinal)} \qquad (2.5)$$

$$\rho\omega^2 u_2 = C_{66} u_2 q_1^2 \qquad \text{(transverse)} \qquad (2.6)$$

$$\rho\omega^2 u_3 = C_{44} u_3 q_1^2 \qquad \text{(transverse)} \qquad (2.7)$$

with corresponding velocity eigenvalues:

$$C_{LA} = \sqrt{C_{11}/\rho} \qquad (2.8)$$

$$C_{TA_1} = \sqrt{\frac{C_{11} - C_{12}}{2\rho}} \qquad (2.9)$$

$$C_{TA_2} = \sqrt{C_{55}/\rho} \qquad (2.10)$$

Eigenvalues and eigenvectors for other q directions are listed in the first and last columns of Table 2-4.

The effect of the sound waves on the optical properties of the crystal is determined via the elastooptic effect which relates the distortion in the dielectric tensor to the strain associated with the acoustic mode:

$$\Delta\varepsilon_{ij} = -\varepsilon_{ii}\varepsilon_{jj}P_{ijk\ell}u_{k\ell} \qquad (2.11)$$

where $P_{ijk\ell}$ are the Pockel's elastooptic coefficients and the xyz axes are chosen to correspond to the principal axes of the dielectric tensor.

Brillouin scattering tensors can be obtained with the use of Eqs. 2.4 and 2.11. This has been done for all the crystal classes by Cummins and Schoen.(47) The third column in Table 2-4 lists the Brillouin scattering tensors for acoustic modes with two selected directions of the phonon wavevector q in the hexagonal crystal class C_{6v}.

The polarization selection rules are now easily derived for Brillouin scattering from a CdS crystal. If, for example, a backscattering geometry is considered with the incident light propagating in the x-direction, it then turns out that the wavevector q of the phonon must also propagate in the x-direction in order to conserve crystal momentum. Using Table 2-4, it is found that only the longitudinal acoustic phonon will contribute to the Brillouin scattering (see Table 2-5 for selection rules).

In addition, for non-centrosymmetrical crystals, the strain of the acoustic mode can also contribute to the polarization accompanying this mode through the piezoelectric effect:

$$P_i = e_{ijk}\, u_{jk} \qquad (i,\ j,\ k = 1,\ 2,\ 3) \qquad (2.12)$$

where e_{ijk} are the piezoelectric stress constants. This results in an electric field which is parallel to the direction of the acoustic wavevector q (known as the longitudinal electric field).(57)

$$E_{\text{long}} = \frac{4\pi}{\varepsilon q} q_i e_{ijk} u_{jk} \tag{2.13}$$

For the light scattering geometry considered earlier for the CdS crystal, $q_i = q_1$ (q_x) and $u_{jk} \approx u_j q_k = u_j q_1$ if plane wave solutions are assumed as before for the displacement vector $\vec{u}$:

$$E_{\text{long}} = \frac{4\pi i}{\varepsilon q} (q_1)^2 e_{1j1} u_j ; \; i = \sqrt{-1} \tag{2.14}$$

The only non-zero piezoelectric constant is e_{131}(e_{15} in contracted notation; see Table 2-6). Thus, the component of the displacement vector is u_3 which corresponds to a transverse acoustic mode.

The piezoelectrically induced longitudinal electric field associated with the TA phonon couples very strongly with an exciton (near resonance) via the Fröhlich interaction. This coupling allows the TA phonon to participate in the resonant Brillouin scattering of exciton-polaritons (see Chap. IV). It is known as forbidden scattering since the selection rules illustrated in Table 2-5 (based on the Pockel's coefficients) indicated that no TA phonon could participate in the Brillouin scattering for the backscattering geometry under consideration.(48)

C. ENERGY BANDS

The band structure of CdS(39) at $\vec{k}=0$ is given in Fig. 2-2 showing the symmetries of the lowest conduction band (Γ_1) and the two highest valence bands (Γ_1 and Γ_5). In the presence of spin-orbit splitting, the doubly degenerate Γ_5 valence band splits into Γ_9 and Γ_7 symmetries with Γ_9 lying higher in energy than Γ_7 while the conduction and lower valence bands, both having Γ_1 symmetry, become Γ_7. The Γ_7 conduction band and the Γ_9 valence band are two-fold spin degenerate and have extrema at the center of the Brillouin zone. The two Γ_7 valence bands have a k-linear term associated with their structure for $\vec{k} \perp \hat{c}$ (see Section D).

TABLE 2-3 ELASTIC STIFFNESS CONSTANTS FOR C_{6v} SYMMETRY

(From Ref. 45, p141)

$$\left|\begin{array}{ccc:ccc}
C_{11} & C_{12} & C_{13} & & & \\
C_{21} & C_{22} & C_{23} & & & \\
C_{31} & C_{32} & C_{33} & & & \\
\hdashline
 & & & C_{44} & & \\
 & & & & C_{55} & \\
 & & & & & C_{66}
\end{array}\right|$$

Values for CdS
from Ref. 58
(in units 10^{10} N/m^2)

$C_{22} = C_{11} = 9.07$

$C_{12} = C_{21} = 5.81$

$C_{13} = C_{31} = C_{32} = C_{23} = 5.10$

$C_{55} = C_{44} = 1.504$

$$C_{66} = \frac{C_{11}-C_{12}}{2} = 1.63$$

TABLE 2-4 SCATTERING TENSOR χ, EIGENVALUES ρv^2 AND EIGENVECTORS $\hat{u}$ OF PHONONS TRAVELING IN THE DIRECTION $\hat{q}$ IN THE HEXAGONAL CRYSTAL CLASS C_{6v}

$\hat{q}$	ρv^2	χ	$\hat{u}$
[100] x-phonon	C_{11}	$\begin{pmatrix} \varepsilon_o^2 P_{11} & 0 & 0 \\ 0 & \varepsilon_o^2 P_{12} & 0 \\ 0 & 0 & \varepsilon_e^2 P_{31} \end{pmatrix}$	[100] Longitudinal
	C_{66}	$\begin{pmatrix} 0 & \varepsilon_o^2 (P_{11}-P_{12})/2 & 0 \\ \varepsilon_o^2 (P_{11}-P_{12})/2 & 0 & 0 \\ 0 & 0 & 0 \end{pmatrix}$	[010] transverse
	C_{44}	$\begin{pmatrix} 0 & 0 & \varepsilon_o \varepsilon_e P_{44} \\ 0 & 0 & 0 \\ \varepsilon_o \varepsilon_e P_{44} & 0 & 0 \end{pmatrix}$	[001] transverse
[110] x+y phonon	$\frac{C_{11}-C_{12}}{2}$	$\frac{1}{2}\begin{pmatrix} \varepsilon_o^2 (P_{11}+P_{12}) & \varepsilon_o^2 (P_{11}-P_{12}) & 0 \\ \varepsilon_o^2 (P_{11}-P_{12}) & \varepsilon_o^2 (P_{11}+P_{12}) & 0 \\ 0 & 0 & 2\varepsilon_e^2 P_{31} \end{pmatrix}$	[110] longitudinal
	C_{11}	$\frac{1}{2}\begin{pmatrix} \varepsilon_o^2 (P_{11}-P_{12}) & 0 & 0 \\ 0 & \varepsilon_o^2 (P_{12}-P_{11}) & 0 \\ 0 & 0 & 0 \end{pmatrix}$	$[1\bar{1}0]$ transverse
	C_{44}	$\frac{1}{\sqrt{2}}\begin{pmatrix} 0 & 0 & \varepsilon_o \varepsilon_e P_{44} \\ 0 & 0 & \varepsilon_o \varepsilon_e P_{44} \\ \varepsilon_o \varepsilon_e P_{44} & \varepsilon_o \varepsilon_e P_{44} & 0 \end{pmatrix}$	[001] transverse

P_{ij} = Pockel's coefficients

$\varepsilon_o, \varepsilon_e$ = dielectric constants: ordinary and extraordinary

TABLE 2-5 BRILLOUIN SCATTERING TENSOR COMPONENTS OF A WURTZITE CRYSTAL (C_{6v}) FOR LIGHT INCIDENT ALONG [100] AND SCATTERED ALONG [$\bar{1}$00] WITH PHONON PROPAGATION ALONG [100]

$\hat{u}$	$x\|yy\|\bar{x}$	$x\|yz\|\bar{x}$	$x\|zy\|\bar{x}$	$x\|zz\|\bar{x}$
[100] Longitudinal	$\varepsilon_o^2 P_{12}$	0	0	$\varepsilon_e^2 P_{31}$
[010] Transverse	0	0	0	0
[001] Transverse	0	0	0	0

TABLE 2-6 PIEZOELECTRIC CONSTANTS FOR C_{6v} SYMMETRY

(From Ref 45, p 124)

$$\begin{vmatrix} 0 & 0 & 0 & 0 & e_{15} & 0 \\ 0 & 0 & 0 & e_{24} & 0 & 0 \\ e_{31} & e_{32} & e_{33} & 0 & 0 & 0 \end{vmatrix}$$

values for CdS
from Ref. 59
(in units C/m^2)

$e_{15} = e_{24} = -0.21$
$e_{31} = e_{32} = -0.25$
$e_{33} = 0.49$

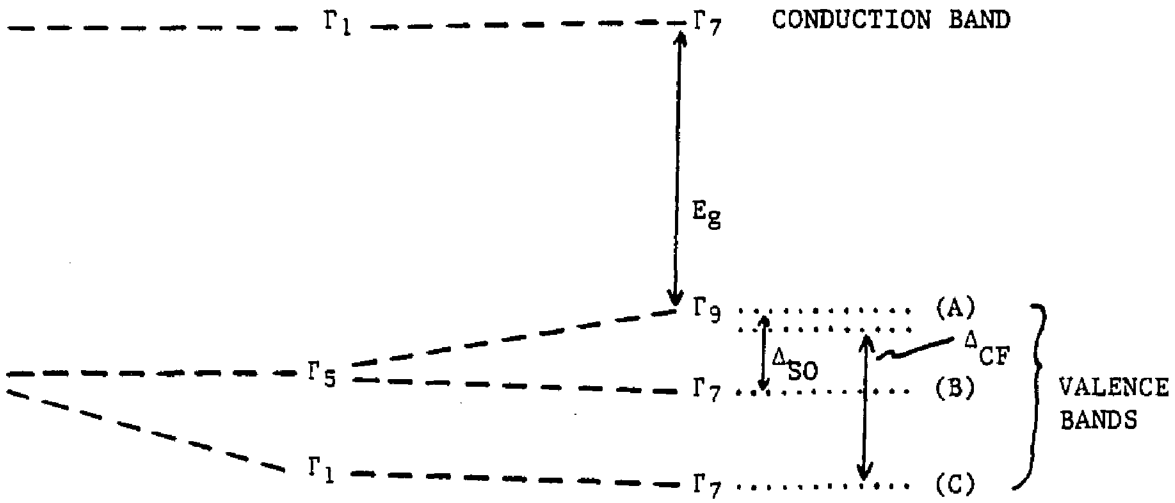

FIG. 2-2. BAND STRUCTURE OF CdS

CdS: $E_g = 2.582$ eV (Band Gap)

$\Delta_{SO} = 0.016$ eV (Spin-Orbit)

$\Delta_{CF} = 0.07$ eV (Crystal Field)

D. EXCITON SERIES

An electron in the Γ_7 conduction band can combine with a hole from either the Γ_9, upper Γ_7 or lower Γ_7 valence band forming the A, B or C exciton series respectively. (The hydrogenic-like energy levels of the coulomb-bound electron-hole system.) The first indication of a possible hydrogenic exciton series in CdS was observed in absorption measurements by Gross et al.(49) and in reflectivity measurements by Dutton(50) and Thomas and Hopfield.(51)

The 1S-state of the A-exciton series has overall symmetry $\Gamma_1 \times \Gamma_9 \times \Gamma_7 = \Gamma_5 + \Gamma_6$ where both the Γ_5 and Γ_6 are twofold degenerate at $\vec{k} = 0$. The Γ_5 level, which transforms like P_x and P_y (i.e., like x and y), is accessible from the group symmetry by a dipole allowed transition(52) and has been observed as a strong absorption(53) line and a sharp reflectivity peak(51) when the incident electromagnetic wave is polarized perpendicular to the c-axis ($\vec{E} \perp \hat{c}$). The Γ_6 level is a pure triplet state (electron and hole spins are parallel) which has been observed in absorption experiments as a weak "forbidden" transition(53) when $\vec{E} \,||\, \hat{c}$.

The 1S state of the B (and also C) exciton series has symmetry $\Gamma_1 \times \Gamma_7 \times \Gamma_7 = \Gamma_1 + \Gamma_2 + \Gamma_5$, where Γ_1 (transforms like z) and Γ_2 (pure spin triplet) are nondegenerate at $\vec{k} = 0$. As expected for the Γ_1 and Γ_5 symmetries, the n = 1 B-exciton state has been observed in reflectivity and absorption experiments as a dipole allowed transition for both $\vec{E} \,||\, \hat{c}$ and $\vec{E} \perp \hat{c}$ polarizations. Several additional features observed in the A and B exciton series will now be discussed.

1. Anisotropy

The deviation from cubic symmetry in wurtzite structures is reflected in the fact that the conduction and valence bands have constant energy surfaces which are ellipsoidal. This introduces an anisotropic effect in CdS which is small enough to be treated as a first order perturbation on the exciton energy levels; it mainly lifts the hydrogenic ℓ and m degeneracies leaving the s levels unshifted(53).

2. K-Linear Term Effects

Group theory shows that energy bands of Γ_7 symmetry should be of the form(54)

$$E = A(k_x^2 + k_y^2) + Bk_z^2 \pm C(k_x^2 + k_y^2)^{1/2} \tag{2.15}$$

the third term, linear in k, represents the splitting of the two spin states by an amount

$$2C\,(k_x^2 + k_y^2)^{1/2} \tag{2.16}$$

for wavevectors perpendicular to the c-axis ($\vec{k} \perp \hat{c}$). The existence of such a term in the second valence band has been used to explain the anomalous structure of the n = 1 B-exciton reflectivity curve in CdS.(55)

This effect has been further substantiated by recent resonant Brillouin scattering experiments near the B-exciton.(31) However, similar experiments performed in the vicinity of the n = 1 A-exciton in CdS have not shown such a k-linear effect.

3. Exchange Interaction Effects(56,61)

The splitting of the Γ_5 and Γ_6 levels of the A-exciton is primarily due to the exchange interaction. The short range (analytic) part of the exchange effect leads to the splitting of the dipole allowed Γ_5 state from the spin triplet Γ_6 state. There is also a long range (nonanalytic) exchange contribution which results in the longitudinal-transverse splitting of the Γ_5 state. The latter effect is dependent on the direction of the exciton wavevector k. For $\vec{k}||\hat{c}$, Γ_5 consists of two degenerate transverse modes; but for $\vec{k} \perp \hat{c}$, Γ_5 has both longitudinal and transverse modes (denoted by Γ_{5_L} and Γ_{5_T} respectively (see Fig. 2-3)). Whenever k is not precisely parallel to the xy plane, some transverse modes become mixed with the longitudinal mode. This enables the longitudinal mode to be observed as an essentially allowed absorption line.(53)

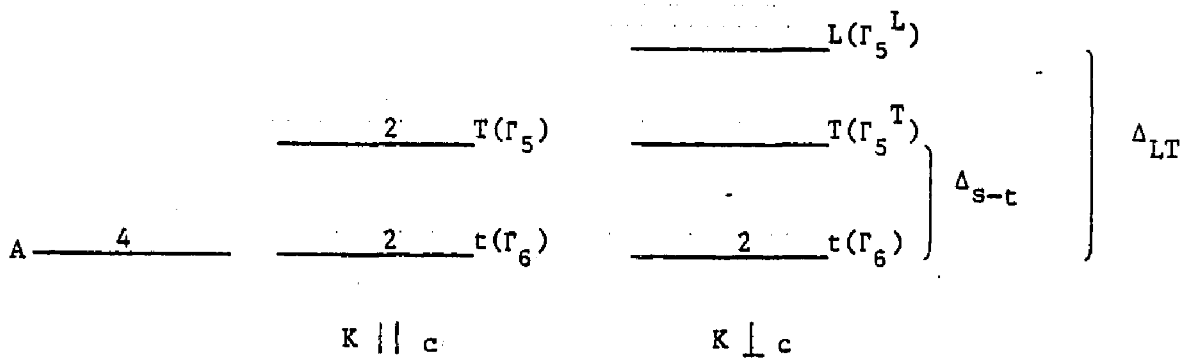

$\Delta_{s-t} \cong 1.6\ \mathrm{cm}^{-1}$ (Ref. 33)

$\Delta_{LT} = 15.4\ \mathrm{cm}^{-1}$ (Ref. 60)

FIG. 2-3 Exciton levels of the n = 1 A-Exciton in CdS as a function of the direction of K (from Ref. 61, p. 27).

CHAPTER III

SCATTERING OF POLARITON MODES VIA THERMALLY EXCITED ACOUSTIC MODE FLUCTUATIONS IN A LOCAL MEDIUM-CLASSICAL APPROACH

A. INTRODUCTION (57)

In this chapter, a simple classical approach to the theory of light scattering of polaritons by thermally induced strain fluctuations is presented. The polariton is formed by the coupling of a macroscopic electromagnetic wave with a localized polar electronic degree of freedom in the medium. The internal motion of this electronic state (which is equivalent to an infinite mass exciton) may be described by an electrically charged harmonic oscillator.

The medium will be a semi-infinite, isotropic, homogeneous, absorbing elastic continuum which is in thermal equilibrium. The properties of propagating acoustic modes described by the elastic wave equation will be briefly reviewed, and the infinite-crystal linear response function for the strain associated with these lattice vibrations will be derived.

A small non-linear coupling between the polariton and the strain is introduced resulting in an anharmonic term in the polariton equation of motion. A non-linear polarization P_{NL} is obtained which is proportional to both the strain and the incident macroscopic electric field. It is this non-linear polarization which radiates the inelastically scattered light, producing both Stokes and anti-Stokes Brillouin components.

In general

$$P_{NL} = \chi^{(2)} u_{xx} E_{\ell}$$

where $\chi^{(2)}$ is a second order susceptibility, u_{xx} is the amplitude of the strain responsible for the inelastic light scattering and E_{ℓ} is the complex amplitude of the incident monochromatic electric field. The power spectrum of the complex Fourier components of the strain $u_{xx}(q,\omega)$ are given by the fluctuation-dissipation theorem (also known as the Nyquist theorem):

$$< u_{xx}(q,\omega)\ u^*_{xx}(q,\omega)>_{\omega} = \frac{k_B T}{\pi\omega}\ \mathrm{Im}\ \chi\ (q,\omega) \tag{3.1}$$

where $\chi\ (q,\omega)$ is the linear response function of the strain $u_{xx}(q,\omega)$.

Only backscattering of normally incident light by the medium will be studied. The scattering geometry is shown in Figure 3-1. We note that for the incident electric field propagating in the x-direction with y-polarization, the only allowed Brillouin scattering is by the longitudinal acoustic mode propagating in the x-direction $\{x[yy]\bar{x}\}$. This is true for hexagonal as well as isotropic crystal classes.

B. LOCAL CLASSICAL OSCILLATOR MODEL IN AN ABSORBING MEDIUM (2, 62)

1. Electronic Motion

a. Equation of Motion

Following the treatment by Burstein and Mills (2) on resonant Raman scattering, the internal electronic motions may be treated as a collection of damped, non-interacting harmonic oscillators with internal displacement r, reduced mass μ, electronic resonance frequency ω_0, and effective charge e^*. The equation of motion is

FIG. 3-1 Schematic representation of a backward RBS experiment involving a semi-infinite, isotropic homogeneous, absorbing local medium.

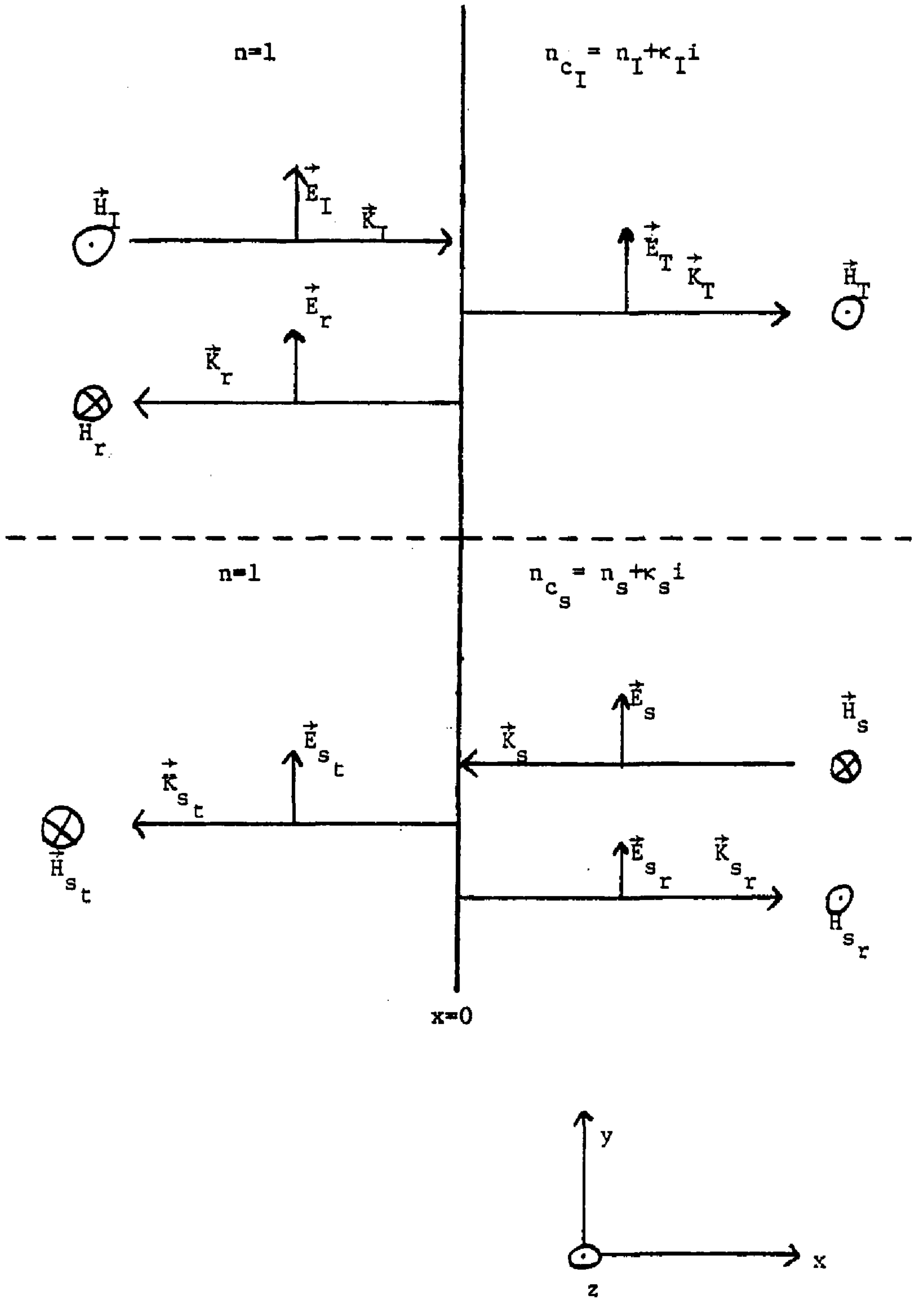

n=1
$n_{c_I} = n_I + \kappa_I i$
$\vec{H}_I$
$\vec{E}_I$
$\vec{K}_I$
$\vec{E}_T$
$\vec{K}_T$
$\vec{H}_T$
$\vec{E}_r$
$\vec{K}_r$
H_r
n=1
$n_{c_s} = n_s + \kappa_s i$
$\vec{E}_s$
$\vec{H}_s$
$\vec{K}_s$
$\vec{E}_{s_t}$
$\vec{K}_{s_t}$
$\vec{H}_{s_t}$
$\vec{E}_{s_r}$
$\vec{K}_{s_r}$
H_{s_r}
x=0
y
x
z

$$\mu(\ddot{\vec{r}} + \Gamma\dot{\vec{r}} + \omega_o{}^2\vec{r}) = e^*\vec{E} \tag{3.2}$$

(r may be considered as the relative coordinate for the electron and hole in a localized exciton state) where $\vec{E}$ is a macroscopic electric field. If the electric field oscillates with frequency ω, then

$$\vec{r} = \frac{e^*\vec{E}}{\mu(\omega_o{}^2-\omega^2-i\omega\Gamma)} \tag{3.3}$$

The total polarization $\vec{P}$ contains a contribution due to the oscillators as well as a contribution from the background dielectric polarization:

$$\vec{P} = \frac{e^*}{V_c}\,\vec{r} + \frac{\varepsilon_b-1}{4\pi}\;\vec{E} \tag{3.4}$$

where V_c is a unit cell volume occupied by a single oscillator and ε_b is the "background" dielectric constant which includes contributions to ε from all other electronic states of the medium.

Substituting Eq. (3.4) into Eq. (3.5) gives:

$$\vec{P} = \frac{(e^*)^2\vec{E}}{\mu V_c(\omega_o{}^2-\omega^2-\ i\omega\Gamma)} + \frac{\varepsilon_b-1}{4\pi}\,\vec{E} \tag{3.5}$$

b. Complex Dielectric Function and the Polariton Dispersion Curves

Since the medium is isotropic, $\vec{r}$, $\vec{E}$ and $\vec{P}$ all point in the same direction. If they also have time and space dependence of the form:

$$\exp\ i(\vec{k}_c\cdot\vec{r} - \omega t)$$

then we obtain the result

$$\varepsilon_c = 1 + \frac{4\pi P}{E} = \varepsilon_b + \frac{4\pi(e^*)^2}{\mu V_c(\omega_o{}^2-\omega^2-i\omega\Gamma)} \tag{3.6}$$

where ε_c is the complex dielectric function.

From Maxwell's equations, the relationship between the dielectric function ε_c and the wave vector k_c for transverse plane-wave fields

$(\vec{k}\underline{|}\vec{E})$ is:

$$\varepsilon_c = \left(\frac{ck_c}{\omega}\right)^2 \qquad (3.7)$$

Combining Eqs. (3.6) and (3.7) yield the polariton dispersion relation:

$$\left(\frac{ck_c}{\omega}\right)^2 = \varepsilon_b + \frac{4\pi(e^*)^2}{\mu V_c(\omega_0{}^2-\omega^2-i\omega\ \Gamma)} \qquad (3.8)$$

This relation results in the polariton dispersion curves shown in Fig. 3-2 which are summarized as follows $(\Gamma = 0)$;

(i) $0 \le \omega \le \omega_0$, k is real for the lower transverse polariton branch. For $\omega \ll \omega_0$, $\omega = \frac{ck}{\sqrt{\varepsilon_b + 4\pi\alpha_0}}$ where $\alpha_0 \equiv \frac{(e^*)^2}{(\mu V_c\omega_0{}^2)}$

(ii) $\omega \to \omega_0$, $k \to +\infty$ Transverse exciton frequency, $\omega_0 = \omega_T$.

(iii) $\omega_0(=\omega_T) \le \omega \le \omega_L$, k is pure imaginary. No propagating mode.

(iv) $\omega = \omega_L \simeq \left(\frac{2\pi(e^*)^2}{\mu V_c\omega_0{}^2\varepsilon_b} + 1\right)\omega_0$ when K = 0

ω_L - longitudinal frequency

(v) $\omega > \omega_L$, k is real for the upper transverse polariton branch.

for $\omega \gg \omega_L$, $\omega \simeq \frac{ck}{\sqrt{\varepsilon_b}}$

2. Acoustic Modes

a. Acoustic Wave Equations

For the model considered here (isotropic medium with acoustic mode propagating in the x-direction) Eq. (2.4) simplifies to the following three equations for u_1, u_2, u_3, (u_x, u_y, u_z)

$$\rho\omega^2 u_1 = C_{11}u_1q_1{}^2 \qquad \text{(longitudinal)} \qquad (3.9)$$

$$\rho\omega^2 u_2 \quad \frac{C_{11}-C_{12}}{2} \quad u_2q_1{}^2 \qquad \text{(transverse)} \qquad (3.10)$$

$$\rho\omega^2 u_3 \quad \frac{C_{11}-C_{12}}{2} \quad u_3q_1{}^2 \qquad \text{(transverse)} \qquad (3.11)$$

FIG. 3-2 Schematic diagram of photon and local polar electronic state. Dot-dash line and broken line at ω_T represent the uncoupled, propagating photon and localized electronic state. Solid lines show the transverse polariton mode. The parameter values used are given in Table 4-1 with $\Gamma = 1.0\text{cm}^{-1}$ and the m^* value set equal to infinity.

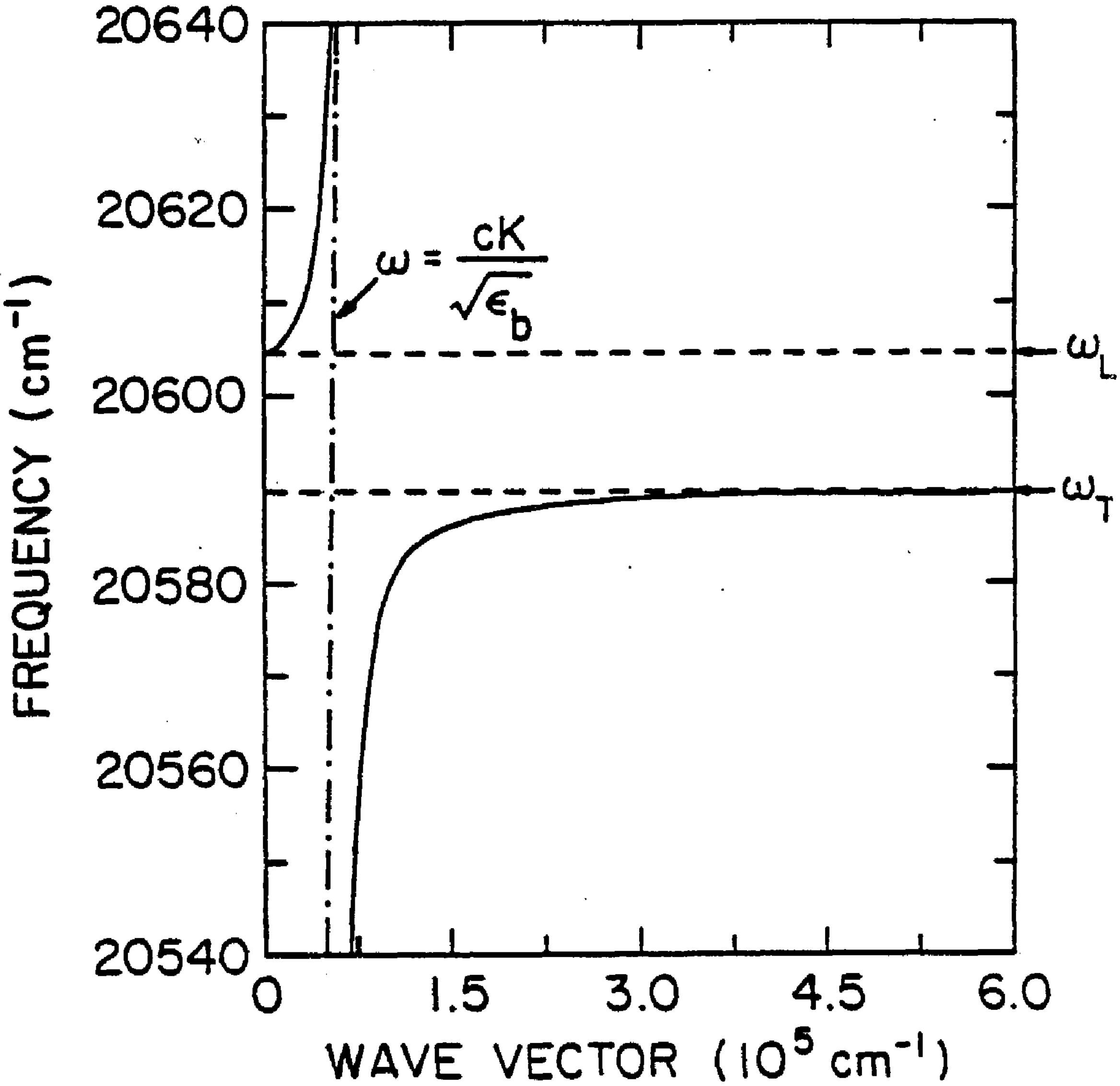
20640
20620
20600
20580
20560
20540
FREQUENCY (cm^{-1})
0
1.5
3.0
4.5
6.0
WAVE VECTOR (10^5 cm^{-1})
$\omega = \frac{cK}{\sqrt{\epsilon_b}}$
ω_L
ω_T

with corresponding velocity eigenvalues:

$$c_{LA} = \sqrt{\frac{C_{11}}{\rho}} \tag{3.12}$$

$$c_{TA} = \sqrt{\frac{C_{11}-C_{12}}{2\rho}} \tag{3.13}$$

b. Acoustic Strain Linear Response Function (63)

As noted in the introduction (section A), we need only concern ourselves with the longitudinal acoustic mode. The response function is determined by the response of the displacement gradient (strain) to an externally applied stress.

$$S_{xx}^{ext} \exp(iqx - i\omega t) \qquad q \equiv q_x$$

The generalized force is defined to be

$$F_{xx} = \bar{V}\, S_{xx}^{ext}$$

where $\bar{V}$ is the crystal volume.

The equation of motion for the longitudinal acoustic displacement including the applied stress is:

$$\rho \ddot{u}_x = C_{11} \frac{\partial^2 u_x}{\partial x^2} + \frac{\partial}{\partial x} [S_{xx}^{ext} \exp(iqx-i\omega t)] \tag{3.14}$$

we again assume plane wave solutions for u_x of the form $\exp(iqx-i\omega t)$

$$-\rho\omega^2 u_x = -q^2 C_{11} u_x + iq\, S_{xx}^{ext} \qquad (3.15)$$

solving for u_x:

$$u_x = \frac{iq\, S_{xx}^{ext}}{(C_{11}q^2 - \rho\omega^2)} \qquad (3.16)$$

The strain associated with u_x is

$$u_{xx} = \frac{\partial u_x}{\partial x} = iq\, u_x \qquad (3.17)$$

assuming plane wave solutions again.

The linear response function is

$$\chi(q,\omega) = \frac{u_{xx}}{F_{xx}} = \frac{u_{xx}}{\bar{V}\, S_{xx}^{ext}} = \frac{iqu_x}{\bar{V}\, S_{xx}^{ext}} \qquad (3.18)$$

Substitution of the expression (3.16) for u_x results in:

$$\chi(q,\omega) = \frac{-q^2}{\bar{V}(C_{11}q^2 - \rho\omega^2)} = \frac{q^2}{\rho\bar{V}(c_s{}^2 q^2 - \omega^2)} \qquad (3.19)$$

where c_s is the longitudinal sound velocity

$$c_s = \sqrt{\frac{C_{11}}{\rho}}$$

Combining Eqs. (3.1) and (3.19) give the following results for the power spectrum of the thermal fluctuations of the longitudinal strain u_{xx}:

$$< u_{xx}(q,\omega)\; u_{xx}^{*}(q,\omega) >_{\omega} = \frac{k_B T q}{2\omega c_s \rho \bar{V}} \{\delta(\omega - c_s q) - \delta(\omega + c_s q)\} \qquad (3.20)$$

{Delta functions result from the assumption of zero damping.}

3. Coupling of the Polariton with the Strain(14)

We now introduce a nonlinear coupling between the polariton and the elastic strain. This can be accomplished by including an anharmonic term $-2\eta u_{xx} r$ on the right hand side in the electronic-polariton equation of motion (3.2). (This is the only term necessary when considering deformation potential interactions.)

$$\mu(\ddot{r} + \Gamma\dot{r} + \omega_0{}^2 r) = -2\,\eta u_{xx} r + e^* E_I \tag{3.21}$$

A laser field in the medium at frequency ω_I and wavevector k_I will couple with the electronic motion, resulting in a polariton, while both the polariton and the strain will undergo thermal vibrations at general frequencies ω with wavevectors q. We now consider single Fourier components of the laser and strain fields at ω_I and ω respectively, and components of the polariton field at both ω and ω_I.

Laser Field

$$\frac{E_I}{2} \exp\ i(k_I x - \omega_I t) + c\cdot c\cdot \tag{3.22}$$

Strain Field

$$\frac{u_{xx}(q,\omega)}{2} \exp\ i(qx - \omega t) + c\cdot d\cdot \tag{3.23}$$

Polariton Field

$$\frac{r(q,\omega)}{2} \exp\ i(qx - \omega t) + \frac{r(k_I,\ \omega_I)}{2} \exp\ i(k_I x - \omega_I t) + c\cdot c\cdot \tag{3.24}$$

where $r(k_I,\ \omega_I)$ solves Eq. (3.21) with $\eta = 0$

$$r(k_I,\ \omega_I) = \frac{e^* E_I}{\mu} \frac{1}{(\omega_0{}^2 - \omega_I{}^2 - i\omega_I \Gamma)} \tag{3.25}$$

Inserting Eqs. (3.22 - 3.24) into (3.21) and considering only the mixing process for the down shifted (Stokes) contribution gives the result

$$\mu(\omega_0{}^2 - \omega_s{}^2 - i\omega_s \Gamma)\ \frac{r(k_s,\omega_s)}{2} \exp\ i(k_s x - \omega_s t)$$

$$= \frac{-\eta}{2} u^*_{xx}(q,\omega) \quad r(k_I,\omega_I) \exp\ i[(k_I - q) - (\omega_I - \omega)t]$$

where $\omega_s = \omega_I - \omega$ (Stokes) (3.26)

Solving for $r(k_s, \omega_s)$ allows the Stokes nonlinear polarization to be obtained:

$$P_s(k_s\omega_s) = \frac{-\eta(e^*)^2 u^*_{xx}(q,\omega)E_I}{V_c\mu^2(\omega_o{}^2-\omega_s{}^2-i\omega_s\Gamma)(\omega_o{}^2-\omega_I{}^2-i\omega_I\Gamma)} \exp\ i[k_I-k_s-q]\ x \qquad (3.27)$$

where the expression (3.25) for $r(k_I, \omega_I)$ has been used.

4. Internal Scattering Cross Section

The backscattered electric field generated by the Stokes nonlinear polarization has been shown to be of the form(64)

$$E_s \propto e^{-i\omega_s t} \int d\vec{q} \int d\vec{r} \exp i[\vec{k}_I-\vec{k}_s-\vec{q}]\cdot\vec{r}\ [V_c P_{NL}(q)] \qquad (3.28)$$

Here, $P_{NL}(q)$ is given by Eq. (3.28) without the exponential.

The internal spectral differential scattering cross section can be calculated from E_s. This has been derived by several authors:(57, 63-66)

$$\left(\frac{d^2\sigma}{d\Omega d\omega_s}\right)_{int} = \frac{\omega_I\omega_s{}^3}{c^4}\left(\frac{n_s}{n_I}\right)\frac{A\bar{V}(V_c)^2}{(2\pi)^3}\int dq\ \frac{\langle P^*_{NL}(q)\ P_{NL}(q)\rangle_{\omega s}}{|k_I+k_s-q|^2|E_I|^2} \qquad (3.29)$$

Here, A is the cross sectional area of the incident laser beam inside the medium and $\bar{V}$ is the total volume of the medium ($\bar{V}$ will be taken to be infinite. However, this volume will be canceled by another $\bar{V}$ in the acoustic response function). We now write $P_{NL}(q)$ as follows:

$$P_{NL}(q) = \chi^{(2)}(\omega_I,\ \omega)\ \frac{u^*_{xx}(q,\omega)E_I}{V_c} \qquad (3.30)$$

where we define $\chi^{(2)}(\omega_I,\omega)$ using Eq. (3.27)

$$\chi^{(2)}(\omega_I,\omega) = \frac{-\eta(e^*)^2}{\mu^2(\omega_o{}^2-\omega_s^2-i\omega_s\Gamma)(\omega_o^2-\omega_I^2-i\omega_I\Gamma)} \qquad (3.31)$$

Substituting Eqs. (3.20) and (3.30) into Eq. (3.29) and doing the q-integration yields:

$$\left(\frac{d^2\sigma}{d\Omega d\omega_s}\right)_{int} = \frac{\omega_I\omega_s^3}{2(2\pi)^3c^4}\ \frac{n_s}{n_I}\ |\chi(\omega_I,\omega)|^2\ \frac{Ak_BT}{c_s^3\rho}\ L(\omega) \tag{3.32}$$

where $\chi(\omega_I,\omega)$ is given by Eq. (3.31) and

$$L(\omega) = \frac{1}{(k_I{}'+k_s{}'-\frac{\omega}{c_s})^2 + (k_I{}''+k_s{}'')^2} \quad \text{(Stokes)}$$

$$+ \frac{1}{(k_I{}'+k_s{}'+\frac{\omega}{c_s})^2 + (k_I{}''+k_s{}'')^2} \quad \text{(Anti-Stokes)} \tag{3.33}$$

Here, k' (k'') is the real (imaginary) part of the polariton wavevector and $\omega = \omega_I - \omega_s$.

The internal differential scattering cross section is simply obtained by integrating Eq. (3.32) over ω_s (that is, by integrating Eq. (3.33) over ω_s). Since

$$\int_{-\infty}^{\infty} d\omega_s\ L(\omega) = \frac{2c_s\pi}{k_I{}''+k_s{}''} \tag{3.34}$$

we obtain for the differential scattering cross section (inside the medium):

$$\left(\frac{d\sigma}{d\Omega}\right)_{int} = \frac{\omega_I\omega_s^3}{(2\pi)^3c^4}\ \frac{n_s}{n_I}\ \frac{|\chi^{(2)}(\omega_I,\omega)|^2}{(k_I{}''+k_s{}'')}\ \pi\ \frac{Ak_BT}{c_s^2\rho} \tag{3.35}$$

C. TRANSMISSION OF THE ELECTROMAGNETIC WAVE BETWEEN VACUUM AND THE ABSORBING MEDIUM

1. Transmissivity and Reflectivity Expressions

a. Vacuum to Medium.(67)

For the geometry of Fig.3-1, Maxwell's equations result in the following boundary conditions:

E - Tangential

$$E_I + E_r = E_t \tag{3.36}$$

H - tangential

$$E_I - E_r = n_{c_I} E_t \tag{3.37}$$

where $n_{c_I} = n_I + i\kappa_I$

The reflection and transmission coefficients resulting from Eqs. (3.36) and (3.37) are

$$r_I = \frac{E_r}{E_I} = \frac{1-n_{c_I}}{1+n_{c_I}} \; ; \; t_I = \frac{E_t}{E_I} = \frac{2}{1+n_{c_I}} \tag{3.38}$$

In order to determine the transmissivity and reflectivity expressions, we must first evaluate the time averaged Poynting vectors for the incident, reflected and transmitted waves. These result from using the general expression:(62)

$$\bar{S}_\alpha = \frac{c}{8\pi} \, R_e(E_\alpha H_\alpha^*) \tag{3.39}$$

Thus, with the use of Eqs. (3.36) and (3.37) and Fig. 3-1,

$$\bar{S}_I = \frac{c}{8\pi} |E_I|^2 \tag{3.40}$$

$$\bar{S}_r = \frac{c}{8\pi} |E_r|^2 \tag{3.41}$$

$$\bar{S}_t = \frac{c}{8\pi} n_I |E_t|^2 \tag{3.42}$$

The reflectivity and transmissivity are now defined as

$$R_I = \frac{\bar{S}_r}{\bar{S}_I} \quad ; \quad T_I = \frac{\bar{S}_t}{\bar{S}_I} \tag{3.43}$$

and with the use of Eqs. (3.38)-(3.42), these become:

$$R_I = |r_I|^2 = \frac{(n_I-1)^2 + \kappa_I^2}{(n_I+1)^2 + \kappa_I^2} \tag{3.44}$$

$$T_I = n_I |t_I|^2 = \frac{4n_I}{(n_I+1)^2 + \kappa_I^2} \tag{3.45}$$

It is clear in this case that $T_I + R_I = 1$

b. Medium to Vacuum

Maxwell's equations now become (see lower half of Fig.3-1).

E - trangential

$$E_{s_t} = E_s + E_{s_r} \tag{3.46}$$

H - tangential

$$E_{s_t} = n_{c_s}(E_s - E_{s_r}) \tag{3.47}$$

where now $n_{c_s} = n_s + i\kappa_s$

The reflection and transmission coefficients now become

$$r_s = \frac{n_{c_s}-1}{n_{c_s}+1} \quad ; \quad t_s = \frac{2n_{c_s}}{n_{c_s}+1} \tag{3.48}$$

along with the time average Poynting vectors

$$\bar{S}_s = \frac{c}{8\pi} n_s |E_s|^2 \tag{3.49}$$

$$\bar{S}_{s_r} = \frac{c}{8\pi} n_s |E_{s_r}|^2 \tag{3.50}$$

$$\bar{S}_{s_t} = \frac{c}{8\pi} |E_{s_t}|^2 \tag{3.51}$$

The reflectivity and transmissivities for this case are

$$R_s = |r_s|^2 = \frac{(n_s-1)^2+\kappa_s^2}{(n_s+1)^2+\kappa_s^2} \tag{3.52}$$

$$T_s = \frac{|t_s|^2}{n_s} = \frac{4(n_s^2+\kappa_s^2)/n_s}{(n_s+1)^2+\kappa_s^2} \tag{3.53}$$

In this case,

$$T_s + R_s = 1 + \frac{4\kappa_s^2/n_s}{(n_s+1)^2+\kappa_s^2} \tag{3.54}$$

The extra term appearing on the right side of Eq. (3.54) can be understood if one calculates the total time averaged Poynting vector on both sides of the boundary.(68)

$$\bar{S}_s(x=0^+) = \frac{c}{8\pi} R_e[(E_s + E_{s_r})\ (n^*_{c_s}E^*_s - n^*_{c_s}E^*_{s_r})] \tag{3.55}$$

$$\bar{S}_s(x=0^-) = \frac{c}{8\pi} R_e|E_{s_t}|^2 = \frac{c}{8} n_s T_s\ |E_s|^2 \tag{3.56}$$

The $\bar{S}_s$ $(x = 0^-)$ expression is just equal to the $\bar{S}_{s_t}$ expression given in Eq. (3.51). If Eq. (3.55) is expanded out, then after some algebra, Eq. (3.55) becomes

$$\bar{S}_s(x=0+) = \frac{c}{8\pi} n_s|E_s|^2 \left(1-R_s + \frac{4\kappa_s^2/n_s}{(n_s+1)^2+\kappa_s^2}\right) \tag{3.57}$$

One can see that with the use of Eq. (3.54), $\bar{S}_s(x = 0^+)$ and $\bar{S}_s(x = 0^-)$ are equal. Thus, the additional term in Eq. (3.54) results from the interference between E_s and E_{s_r} in the absorbing medium. Such a term is not present in a non-absorbing medium.

In the limit where κ_s is small one can approximate T_s as follows:

$$T_s \approx 1-R_s = \frac{4n_s}{(n_s+1)^2+\kappa_s^2} \tag{3.58}$$

since the additional term in Eq. (3.54) goes as $\kappa_s{}^2$. This approximate form for T_s will be used for the remainder of this chapter.

D. EXTERNAL SCATTERING CROSS SECTION

The external scattering cross section for the scattering of polariton modes by thermally excited acoustic mode fluctuations can now be obtained by substituting Eqs. (3.35), (3.45) and (3.58) into Eq. (1.14). The resulting external scattering cross section is:

$$\left(\frac{d\sigma}{d\Omega}\right)_{ext} = \frac{T(\omega_I)\ T(\omega_s)\omega_I\omega_s^3|\chi^{(2)}(\omega_I,\omega)|^2\ Ak_BT}{8\pi^2c^4n_In_s\left(k_I'' + k_s''\right)\ c_s^2\ \rho} \tag{3.59}$$

CHAPTER IV

RESONANT SCATTERING OF EXCITON-POLARITONS VIA PHONONS IN SPATIALLY DISPERSIVE MEDIA-QUANTUM MECHANICAL APPROACH

A. INTRODUCTION

In this chapter the resonant scattering of exciton-polaritons via acoustic phonons is discussed from a quantum mechanical point of view. A backscattering geometry will again be considered (Fig. 4-1). The medium is now considered to be spatially dispersive as well as homogeneous, absorbing and semi-infinite in extent. For this case, if the incident laser frequency is above the longitudinal frequency of the exciton state, two transverse polariton modes can propagate in the medium. An additional boundary condition (ABC) must therefore be included along with Maxwell's boundary conditions to describe this phenomenon.

In Sec. B., we briefly summarize the exciton Hamiltonian, wavefunction and energy eigenvalues. In the following section the exciton is allowed to couple to a photon field resulting in the exciton-polariton dispersion equation. Polariton-lattice interactions are then discussed.

In Sec. D., a general form for the three ABCs most frequently cited in the literature is given and a theoretical expression for the external differential scattering cross section is derived for the RBS process. This expression is dependent on the ABC as well as the incident laser frequency and can be used for direct comparisons with experimental RBS measurements. Such comparisons are made in Chap. VI.

B. EXCITON THEORY(69)

1. The Hamiltonian

An exciton consists of an electron and hole which are bound together by an effective coulomb interaction. In the effective mass approximation, the energy levels of the exciton states are solutions of the Hamiltonian:

$$H_{ex} = H_e(\vec{P}_e) + H_h(\vec{P}_h) - \frac{e^2}{\varepsilon|\vec{r}_e-\vec{r}_h|} \tag{4.1}$$

where ε is the dielectric constant and $H_e(H_h)$ is the electron (hole) kinetic energy term.

If both the conduction and valence bands are spherical with band extrema at $\vec{K} = 0$, Eq. (4.1) becomes:

$$H_{ex} = - \frac{\hbar^2}{2\mu} \nabla_r^2 - \frac{\hbar^2}{2m^*} \nabla_R^2 - \frac{e^2}{\varepsilon r} + E_g \tag{4.2}$$

where the center of mass and internal motion of the exciton have been separated by the transformation

$$\vec{R} = \frac{m_e^*\vec{r}_e + m_h^*\vec{r}_h}{m^*} \; ; \quad \vec{r} = \vec{r}_e - \vec{r}_h \tag{4.3}$$

where $m^* = m_e^* + m_h^*$ is the translational mass, $\mu = \frac{m_e^* \; m_h^*}{m^*}$ is the reduced mass and E_g is the band gap energy.

2. Exciton Wavefunction and Energy Levels.

The solutions of Eq. (4.2) are

$$\psi_{ex}(\vec{r}_e,\vec{r}_h) = \exp\,(i\vec{k}\cdot\vec{R})\; \phi_{n\ell}(\vec{r})\; u_{c_o}(\vec{r}_e)\; u_{vo}(\vec{r}_h) \tag{4.4}$$

The plane wave reflects the free-particle motion of the center of mass; $u_{c_o}(\vec{r}_e)$ $[u_{v_o}(\vec{r}_h)]$ is the Bloch function for the electron (hole) having the periodicity of the lattice, and $\phi_{n\ell}(\vec{r})$ is the hydrogenic envelop function describing the spatial extent of the relative electron-hole motion.

The exciton energy eigenvalues are of the form:

$$E_n(\vec{k}) = E_g + \frac{\hbar^2k^2}{2m^*} - \frac{R^*}{n^2} \; ; \; n = 1,\ 2,\ 3,\ \ldots\ldots \tag{4.5}$$

with the exciton Rydberg defined as

$$R^* = \frac{\mu e^4}{2\hbar^2\varepsilon^2} \tag{4.6}$$

3. Application to the n = 1 A-Exciton in CdS

In Chap. II, it was noted that the anisotropic property associated with the energy bands in CdS could be neglected when considering the S-states of the A, B, and C exciton series. However, anisotropy must be included in the expression for the center of mass motion. For example, in order to properly describe the total energy of the n = 1 A-exciton state, Eq. (4-5) must take the following form:

$$E_{n=1}(\vec{k}) = \hbar\omega_o + \frac{\hbar^2k^2}{2}\left(\frac{\sin^2\theta}{m^*_{A\perp}} + \frac{\cos^2\theta}{m^*_{A||}}\right) \tag{4.7}$$

where $\omega_o \equiv E_g - R^*$ is the transverse exciton frequency (i.e., frequency of the $\Gamma_5{}^T$ state shown in Fig. 2-3), θ is the angle between the exciton wavevector $\vec{k}$ and the c-axis ($\hat{c}||\hat{z}$) and $m^*_{A\perp}$ ($m^*_{A||}$) is the effective exciton mass perpendicular (parallel) to the c-axis.

For the scattering geometry considered $\hat{k}||\hat{x}$ (θ=90°), Eq. (4.7) becomes

$$E_{n=1}(\vec{k}) = \hbar\omega_{ex}(\vec{k}) = \hbar\omega_o + \frac{\hbar^2k^2}{2m^*} \tag{4.8}$$

where m^* will now be denoted as $m^*_{A\perp}$ and $\omega_{ex}(\vec{k})$ is the k-dependent exciton frequency. Values of the parameters describing the n = 1 A-exciton are given in Table 4-1.

TABLE 4-1 VALUES OF THE $n = 1$ A-EXCITON IN CdS FOR $\vec{k} \perp \hat{c}$

Dielectric Constant (60)	
ε_b	9.3
Binding Energy (51)	
R^*(eV)	0.03
Effective Mass (60)	
m^*(m_e)	0.89
Oscillator Strength (60)	
$4\pi\alpha_o$	0.0139
Transverse Frequency (60)	
ω_o(cm^{-1})	20589.5

FIG. 4-1 Schematic representation of a backward RBS experiment involving a semi-infinite spatially dispersive medium. Wavy, solid and broken lines denote photons, polaritons and acoustic phonons, respectively. The rectangle numbered 2 represents the polariton-phonon interaction.

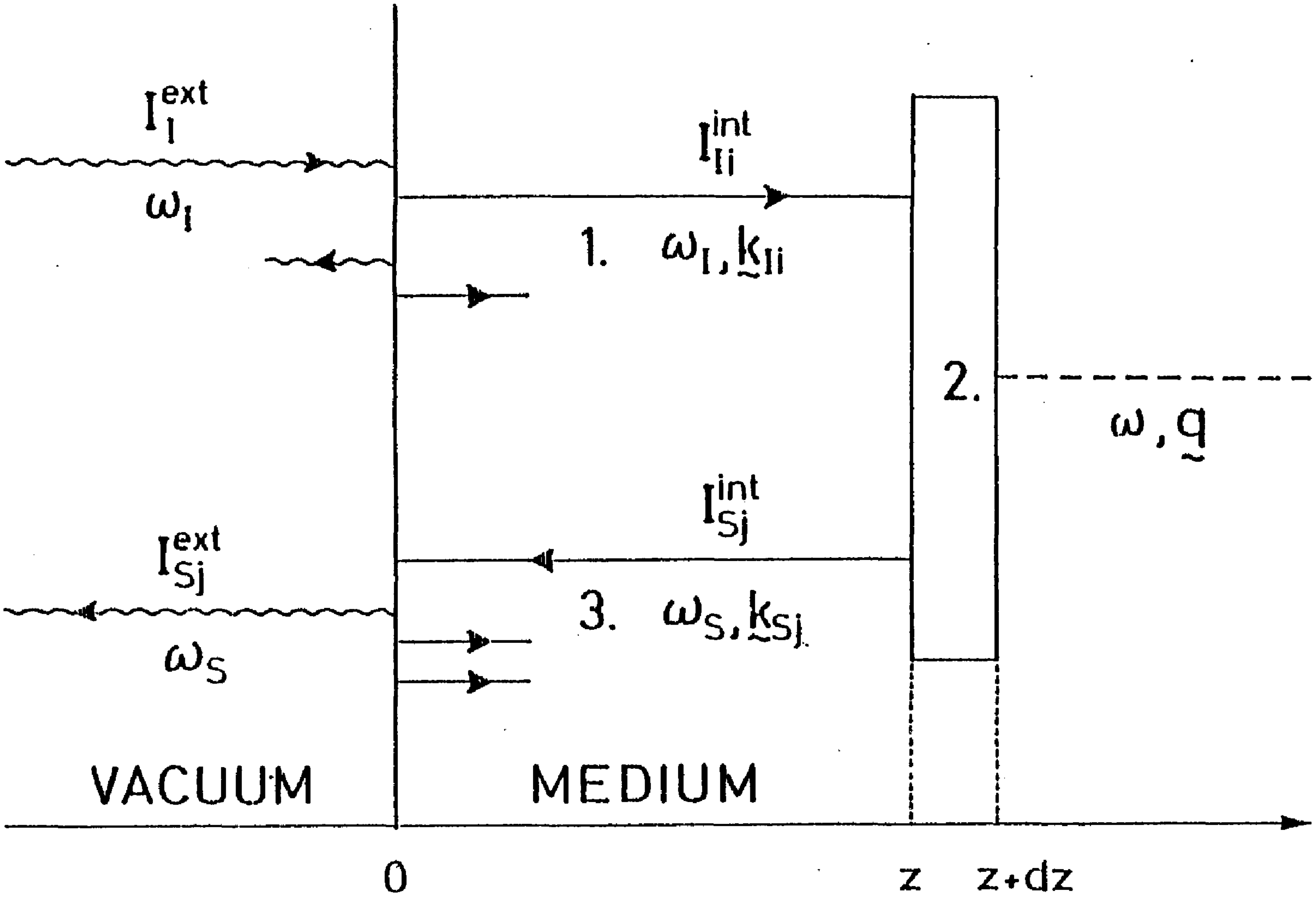
I_l^{ext}
ω_l
I_{li}^{int}
1. $\omega_l, \underset{\sim}{k}_{li}$
2.
$\omega, \underset{\sim}{q}$
I_{Sj}^{int}
I_{Sj}^{ext}
3. $\omega_S, \underset{\sim}{k}_{Sj}$
ω_S
VACUUM
MEDIUM
0
z
z+dz

C. EXCITON-POLARITON THEORY

1. The Hamiltonian

When transitions between the conduction and valence bands are dipole allowed, the exciton formed between these bands can couple strongly with the radiation field via its polarization. The diagonalization of the Hamiltonian:

$$H = H_{ex} + H_{rad} + H_{ex-rad} \tag{4.9}$$

must now be made to determine the correct normal modes of the crystal. These coupled exciton-photon normal modes are known as exciton-polaritons. The different contributions to the polariton Hamiltonian Eq. (4.9) are listed below:

(i) $$H_{ex} = \sum_{\vec{k}} \hbar\, \omega_{ex}(\vec{k})\, [b^{+}_{\vec{k}} b_{\vec{k}} + \tfrac{1}{2}] \qquad \text{(exciton)} \tag{4.10a}$$

where $\hbar\omega_{ex}(\vec{k})$ is the A-exciton energy [see Eq. (4.5)]

(ii) $$H_{rad} = \sum_{\vec{k}} \hbar\, \tilde{c}\, k\, [a^{+}_{k} a_{k} + \tfrac{1}{2}] \qquad \text{(photon)} \tag{4.10b}$$

where $k = |\vec{k}|$ and $\tilde{c} = c/\sqrt{\varepsilon_b}$

(iii) (exciton-photon) (4.10 c)

$$H_{ex-rad} = \sum_{\vec{k}} \Big\{ \hbar \left(\frac{4\pi\alpha_o\omega_o^2}{\varepsilon_b}\right)^{\frac{1}{2}} \left(\frac{\omega_E(\vec{k})}{4\tilde{c}k}\right) i\,(b_{\vec{k}} - b^{+}_{-\vec{k}})(a^{+}_{\vec{k}} + a_{-\vec{k}})$$
$$+ \frac{\pi\alpha_o\omega_o^2\hbar}{\varepsilon_b\tilde{c}k} (a^{+}_{\vec{k}} + a_{-\vec{k}})\,(a_{\vec{k}} + a^{+}_{-\vec{k}}) \Big\}$$

Here $a^{+}_{\vec{k}}$, $a_{\vec{k}}$ ($b^{+}_{\vec{k}}$, $b_{\vec{k}}$) are the creation and annihilation operators for the radiation (exciton) field.

2. Exciton-Polariton Dispersion Equation

Since the exciton-photon interaction Hamiltonian is bilinear in the creation and annihilation operators of the photon and exciton [see Eq.

(4.10c)], the total polariton Hamiltonian Eq. (4.9) can be diagonalized ($\hbar = 1$). This procedure was first reported by Hopfield.$^{(7)}$ The result of the diagonalization process is the exciton-polariton dispersion equation (transverse modes):

$$\left(\frac{\tilde{c}k}{\omega}\right)^2 = 1 + \frac{4\pi\alpha_o\omega_o^2/\varepsilon_b}{\omega_{ex}^2(\vec{k}) - \omega^2} \qquad (4.11)$$

where α_0 is the oscillator strength of the exciton, $\omega_0 = \omega_{ex}(0)$ is the transverse exciton frequency, ε_b is the background dielectric constant, $\omega_{ex}(\vec{k})$ is the k-dependent exciton frequency, and ω is the polariton (normal mode) eigenfrequency.

Substituting Eq. (4.8) into Eq. (4.11) and keeping terms up to k^2 yields:

$$\left(\frac{\tilde{c}k}{\omega}\right)^2 = 1 + \frac{4\pi\alpha_o\omega_o^2/\varepsilon_b}{\omega_o^2 + \frac{\omega_o k^2}{m^*} - \omega^2} \qquad (4.12)$$

The dispersion equation now has two independent normal mode solutions, $\omega_1(\vec{k})$ and $\omega_2(\vec{k})$ for a given wavevector $\vec{k}$. The dispersion curves resulting from Eq. (4.12) are shown in Fig. 4-2 and are summarized below:

(i) For $\omega \ll \omega_0$; only one transverse polariton branch (mode) exists:

$$\omega_2(\vec{k}) = \frac{ck}{\sqrt{\varepsilon_b + 4\pi\alpha_o}}$$

(ii) For $\omega_0 < \omega < \omega_L$ (ω_L - longitudinal exciton frequency); the $\omega_2(\vec{k})$ branch deviates from its linear slope in (i) and starts to take on a more exciton-like behavior.

(iii) $\omega_L < \omega$; there are now two transverse polariton branches propagating in the medium [shown in Fig. 4-2 as $\omega_1(\vec{k})$ and $\omega_2(\vec{k})$]

(iv) $\omega_L << \omega$; the "inner" polariton branch $\omega_1(\vec{k})$ behaves very much like a photon, $\omega_1(\vec{k}) = \frac{ck}{\sqrt{\varepsilon_b}}$, where the "outer" polariton branch shows a typical exciton behavior $\omega_2(\vec{k}) = \omega_\circ + \frac{k^2}{2m^*}$

3. Polariton-Phonon Interaction

a. General Expression

The polariton-phonon interaction is known to arise predominantly from the exciton-phonon interaction Hamiltonian, the general form being given by:

$$H_{ex-ph} = i(\bar{V})^{-\frac{1}{2}} \sum_{\vec{q},\vec{k}} \Gamma_\circ(\vec{q})\; b^+_{\vec{k}+\vec{q}} b_{\vec{k}} (c_{\vec{q}} - c^+_{-\vec{q}}) \qquad (4.13)$$

where $\Gamma_o(\vec{q})$ denotes the exciton-phonon interaction kernel, $c_{\vec{q}}$ $(c^+_{-\vec{q}})$ is the phonon annihilation (creation) operator, $\bar{V}$ is the crystal volume, and $i = \sqrt{-1}$

In order to derive the general expression for the polariton-phonon interaction, the exciton operators $b^+_{\vec{k}+\vec{q}}$, $b_{\vec{k}}$ must be expressed in terms of polariton operators. Since it was noted that the exciton-polariton dispersion Eq. (4.12) has two independent solutions $\omega_i(\vec{k})(i = 1,2)$ for a given wavevector $\vec{k}$, there must be two independent polariton annihilation (creation) operators, $\alpha_{\vec{k}1}$ and $\alpha_{\vec{k}2}$ $[\alpha^+_{(\vec{k}+\vec{q})1}$ and $\alpha^+_{(\vec{k}+\vec{q})2}]$ both of which satisfy the usual boson commutation relations.

A transformation from exciton to polariton operators has been performed by Hopfield(7) allowing the polariton-phonon interaction to be written as:

FIG. 4-2 Schematic diagram of photon and exciton dispersion curves. Broken lines represent the uncoupled exciton and photon propagating in the medium. Solid lines show the two exciton-polariton modes $[\omega_1(\vec{k})$ and $\omega_2(\vec{k})]$. The parameter values used are given in Table 4-1 with $\Gamma = 1.0\mathrm{cm}^{-1}$.

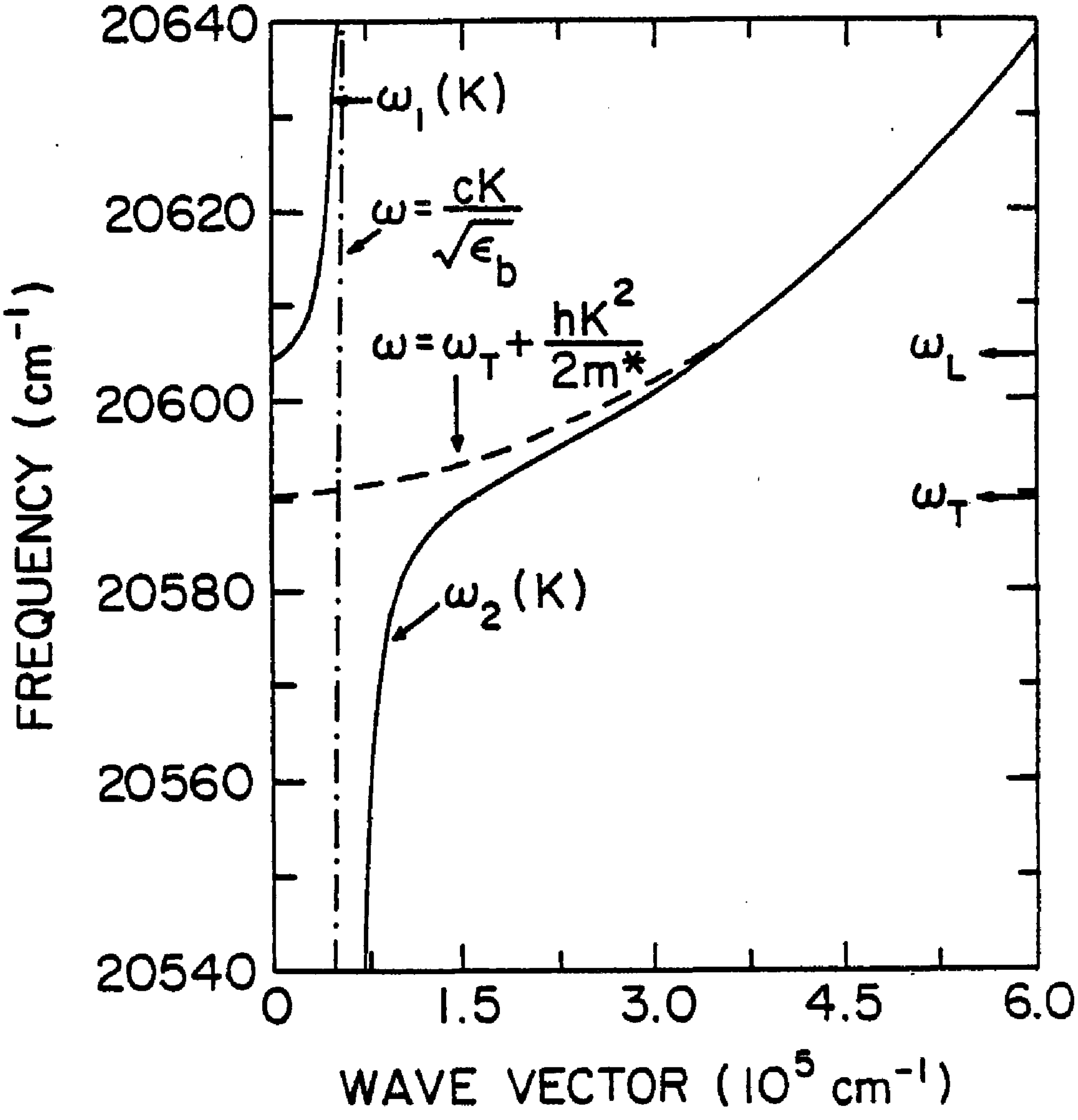
20640
20620
20600
20580
20560
20540
FREQUENCY (cm^{-1})
0
1.5
3.0
4.5
6.0
WAVE VECTOR (10^5 cm^{-1})
$\omega_1(K)$
$\omega = \frac{cK}{\sqrt{\epsilon_b}}$
$\omega = \omega_T + \frac{hK^2}{2m^*}$
$\omega_2(K)$
ω_L
ω_T

$$H_{\text{Pol-ph}}^{j\leftarrow i} = \frac{(i)^{j-i+1}}{2}(\bar{V})^{-\frac{1}{2}} \sum_{\vec{q},\vec{k}} \Gamma_\circ(\vec{q})\, A_{ij}(\vec{k},\vec{k}+\vec{q})$$

$$\times\, \alpha^{+}_{(\vec{k}+\vec{q})_j}\, \alpha_{\vec{k}_i}\, (c_{\vec{q}} - c^{+}_{-\vec{q}}) \tag{4.14}$$

where

$$A_{ij}(\vec{k},\vec{k}+\vec{q}) = \tfrac{1}{2} A_i^{\frac{1}{2}}(\vec{k}) \left[1 + \frac{\omega_{ex}(\vec{k})\ \omega_{ex}(\vec{k}+\vec{q})}{\omega_i(\vec{k})\ \omega_j(\vec{k}+\vec{q})}\right] A_j^{\frac{1}{2}}(\vec{k}+\vec{q})$$

This Hamiltonian mediates the scattering of an incident mode-i polariton to a scattered mode-j polariton via the creation or annihilation of one phonon. It is equivalent to the expression given by Burstein et al.(70)

The factor $A_i(\vec{k})$ is known as the exciton strength function and is generally written:

$$A_i(\vec{k}) = \frac{4\pi\alpha_\circ\omega_\circ^2\omega_{ex}(\vec{k})\omega_i(\vec{k})}{[\omega_{ex}^2(\vec{k})-\omega_i^2(\vec{k})]^2} \Bigg/ \left(\epsilon_b + \frac{4\pi\alpha_\circ\omega_\circ^2\omega_{ex}^2(\vec{k})}{[\omega_{ex}^2(\vec{k})-\omega_i^2(\vec{k})]^2}\right) \tag{4.15}$$

It provides a direct quantitative measure of the exciton content in the polarization mode $\omega_i(\vec{k})$, $(i = 1, 2)$. It can be described as the ratio of the mean square exciton polarization associated with a polariton of frequency $\omega_i(\vec{k})$ to the mean square exciton polarization associated with an exciton of frequency $\omega_{ex}(\vec{k})$ (see Eq. 4-26 below). The numerator of this ratio can be obtained in terms of the total energy density of the polariton (both the mechanical and electromagnetic-contributions,see Appendix A, Eq. (A.14)). The denominator is similarly obtained in terms of the mechanical (exciton) energy density.

In the following two subsections, specific expressions for the exciton-acoustic phonon matrix element $\Gamma_\circ(\vec{q})$ will be obtained for the deformation potential and piezoelectric interactions.

b. Deformation Potential Interaction(11, 71-73)

The strain associated with an acoustic phonon perturbs the periodic potential acting on the electrons in a crystal, resulting in a small shift in the electronic energy bands. The proportionality constant between this energy shift and the strain is defined as the deformation potential.

The deformation potential exciton-acoustic phonon Hamiltonian is expressed as:

$$H^{dp}_{ex-ph} = (D^{e}_{ij} + D^{h}_{ij})\, u_{ij} \tag{4.16}$$

where the second rank tensor $D^{e}_{ij}(D^{h}_{ij})$ is the deformation potential for the electron (hole) and u_{ij} is the strain.

As noted in Chap. II, Table 2-5, for a medium with hexagonal symmetry (wurtzite CdS with C_{6v} symmetry), only the longitudinal acoustic phonon will be allowed via the deformation potential interaction to participate in the backscattering geometry $\{x|yy|\bar{x}\}$. Thus, Eq. (4.16) becomes:

$$H^{dp}_{ex-ph} = (D^{e} + D^{h})\, u_{xx} \tag{4.17}$$

where $u_{xx} = iq\,(\hbar/2\rho\omega_{q})^{\frac{1}{2}},\ q \equiv q_{x}$

In this case, the exciton-phonon matrix element for the deformation potential interaction becomes:

$$\Gamma_{o}^{dp}(q) = (\hbar/2\rho c_{LA})^{\frac{1}{2}} \sqrt{q}\,(D^{e} + D^{h}) \tag{4.18}$$

where ρ is the crystal density and c_{LA} is the longitudinal sound velocity.

c. Piezoelectric Interaction(11, 59, 73)

As discussed in Chap. II, in piezoelectric crystals the strain field associated with an acoustic phonon can produce an electric field via the piezoelectric effect. The longitudinal component of this induced electric field can interact with excitons resulting in the piezoelectric exciton-phonon interaction. This interaction is similar to the Fröhlich interaction between excitons and LO phonons.

Examining the case of the wurtzite semiconductor CdS, the piezoelectric exciton-phonon interaction Hamiltonian is:(73)

$$H^{pe}_{ex-ph} = \frac{4\pi e}{\varepsilon_b}\{e_{15}\sin\theta(u_z\sin\theta + u_x\cos\theta) + e_{31}u_x\sin\theta\cos\theta + e_{33}u_z\cos^2\theta\} \times [\exp(i\vec{q}\cdot\vec{r}_e) - \exp(i\vec{q}\cdot\vec{r}_h)] \tag{4.19}$$

where θ is the angle between $\vec{q}$ and the z-axis (which is also the c-axis) u_z and u_x are the components of the phonon displacement (x-axis lies in $\vec{q}$-z plane), and e_{15}, e_{31}, e_{33} are the non-zero piezoelectric components (see Chap. II, Table 2-6).

Considering again the case where $\vec{q}\,||\,\hat{x}$ (θ = 90°), one finds that only the transverse phonon displacement u_z can participate in the scattering:

$$H^{pe}_{ex-ph} = \frac{4\pi e}{\varepsilon_b}\, e_{15}u_z[\exp(i\vec{q}\cdot\vec{r}_e) - \exp(i\vec{q}\cdot\vec{r}_h)] \tag{4.20}$$

The matrix element for this piezoelectric exciton-phonon interaction is:

$$\Gamma^{pe}_{o}(q) = \left(\frac{4\pi e}{\varepsilon_b}\right) e_{15}\left(\frac{\hbar}{2\rho c_{TA}}\right)^{\frac{1}{2}} \frac{(Q_e-Q_h)}{\sqrt{q}} \tag{4.21}$$

The factor $[Q_e - Q_h]$ involves the Fourier component of the exciton envelop wavefunction(72) taken in the direction of propagation of the piezoelectric active phonon. Considering matrix elements where the initial and final states are 1S exciton states (e.g., 1S A-exciton in CdS):

$$[Q_e - Q_h] \cong \left(\frac{m_e^* - m_h^*}{m_h^* + m_e^*} \right) \frac{q^2 a_B^2}{2} \tag{4.22}$$

where a_B is the exciton Bohr radius.

Substituting Eq. (4.22) into Eq. (4.21) yields

$$\Gamma_o^{pe}(q) = \frac{2\pi e \, a_B^2}{\varepsilon_b} \, e_{15} \left(\frac{\hbar}{2\rho c_{TA}} \right)^{\frac{1}{2}} q^{\frac{3}{2}} \, \frac{m_e^* - m_h^*}{m_h^* + m_e^*} \tag{4.23}$$

D. RESONANT BRILLOUIN SCATTERING

1. General Considerations

As illustrated in Fig.4-1, the RBS process in the medium consists of three steps. Step 1 (step 3) is concerned with the attenuation of the incident (scattered) polariton while step 2 is the polariton-phonon scattering process. The damping process in steps 1 and 3 is believed to be due to the additional scattering of the polaritons via phonons and/or impurities, the effect of which is incorporated into an exciton damping constant Γ (the attenuation of polaritons is usually attributed to the damping of excitons).

The damping constant Γ can be phenomenologically included in the dispersion equation by making the following replacement for the square of the exciton frequency.(74)

$$\omega_{ex}^2(\vec{k}) \rightarrow \omega_{ex}^2(\vec{k},\omega) = \omega_{ex}^2(\vec{k}) - i\omega\Gamma \tag{4.24}$$

Combining this with Eq. (4.8) and substituting into Eq. (4.11) yields:

$$\left(\frac{k}{\omega} \right)^2 = \varepsilon_b + \frac{4\pi\alpha_o \omega_o^2}{\omega_o^2 + Bk^2 - \omega^2 - i\omega\Gamma} \tag{4.25}$$

where $B \equiv \frac{\hbar\omega_o 2\pi}{m^*}$ (ω_o, ω, Γ, k are all in units of cm^{-1}). This is just the polariton dispersion equation derived by Hopfield and Thomas.(9)

The exciton strength function can also be modified to include Γ by extending the method reported by D. L. Mills and E. Burstein(2) to the case of spatial dispersion

$$A_i(\vec{k}_i) = \frac{2\kappa_i \omega_{ex}(\vec{k})}{\Gamma - 2B\omega n_i \kappa_i} \left[n_i + \frac{2\omega\kappa_i(1+B\kappa_i^2)}{\Gamma - 2B\omega n_i \kappa_i} \right]^{-1} \tag{4.26}$$

Here $n_i = \frac{c}{\omega}\,\mathrm{Re}[k_i(\omega)]$ and $\kappa_i = \frac{c}{\omega}\,\mathrm{Im}[k_i(\omega)]$. As can be seen in Fig.4-3, even below the exciton resonance ($\omega<\omega_o$) most of the energy of the polariton resides in the exciton. Eq. (4.26) reduces to Eq. (4.15) when $\Gamma \to 0$.

We note that both the dispersion equation (4.25) and the exciton strength function (4.26)(see Figs.4-2 and 4-3) are relatively insensitive to Γ as long as $\Gamma < \Gamma_c$. Here Γ_c is a critical value of the exciton damping constant given by:(74)

$$\Gamma_c = 4(\pi\alpha_o B\omega_o^2)^{\frac{1}{2}} \tag{4.27}$$

and is essentially the value where the $\mathrm{Im}[k_i(\omega)] = \mathrm{Re}[k_i(\omega)]$. For values of $\Gamma > \Gamma_c$, excitons and photons behave as if there were essentially no interaction between them(75) (for CdS, $\Gamma_c = 11.5\mathrm{cm}^{-1}$).

The following three subsections (2-4) describe the kinematics and the internal scattering cross section (via perturbation theory) of the RBS process. In section 5, the transmissivity factors of the incident and scattered photons at the vacuum-medium boundary are evaluated in addition to the solid angle correction factor for the scattered photons.

2. Kinematics and the Brillouin Shift

The strong absorption in a medium near an exciton resonance region necessitates the use of a backscattering geometry for the RBS studies.

The laws of conservation of energy and momentum become +

$$\omega_s - \omega_I = \pm \omega \qquad (4.28)$$

$$k_{sj} - k_{Ii} = \pm q \qquad (4.29)$$

Here ω_I, k_{Ii} and ω_s, k_{sj} represent the frequencies and wavevectors of the incident mode-i and scattered mode-j polaritons respectively. The +(-) sign corresponds to anti-Stokes (Stokes) scattering. For Brillouin scattering

$$\omega = c_s q \qquad (4.30)$$

where c_s is the acoustic sound velocity. The conservation of momentum [Eq. (4.29)] does not hold exactly since the wavevectors are complex.

In Fig. (4-4), the exciton-polariton dispersion curves have been drawn for the backscattering geometry case first discussed by BZB. The kinematics [Eqs. (4.28) and (4.29)] are represented by the arrows which illustrate both Stokes (downward slopes) and anti-Stokes (upward slopes) scatterings for incident frequency ω_I. Note the possibility of a Brillouin octet for $\omega_I > \omega_L$ (compared to the normal Brillouin doublet for ω_I well below ω_L).

By combining Eqs. (4.28) - (4.30), an expression for the Brillouin shift is found ($\Gamma < \Gamma_c$)

$$\Delta\omega = \omega_s - \omega_I = \pm c_s \{k'_{Ii}(\omega_I) + k'_{sj}(\omega_s)\} \qquad (4.31)$$

where k'(k") is now defined as the real (imaginary) part of k. This expression can be solved numerically by an iterative procedure using the dispersion equation [Eq. (4.25)]. By fitting this expression to the Brillouin shift data, accurate values for the parameters ε_b, m^*, ω_0, α_0 can be determined. (see Chap. VI).

+ The polariton is now regarded as a forced harmonic oscillator with a real frequency and a complex frequency dependent wavevector ($k_{Ii}(\omega_I)$).

FIG. 4-3 Exciton strength functions of both mode-1 and mode-2 polaritons as a function of frequency. The number labeled on each curve specifies the polariton mode. The parameter values used are given in Table 4-1 with $\Gamma = 1.0\mathrm{cm}^{-1}$.

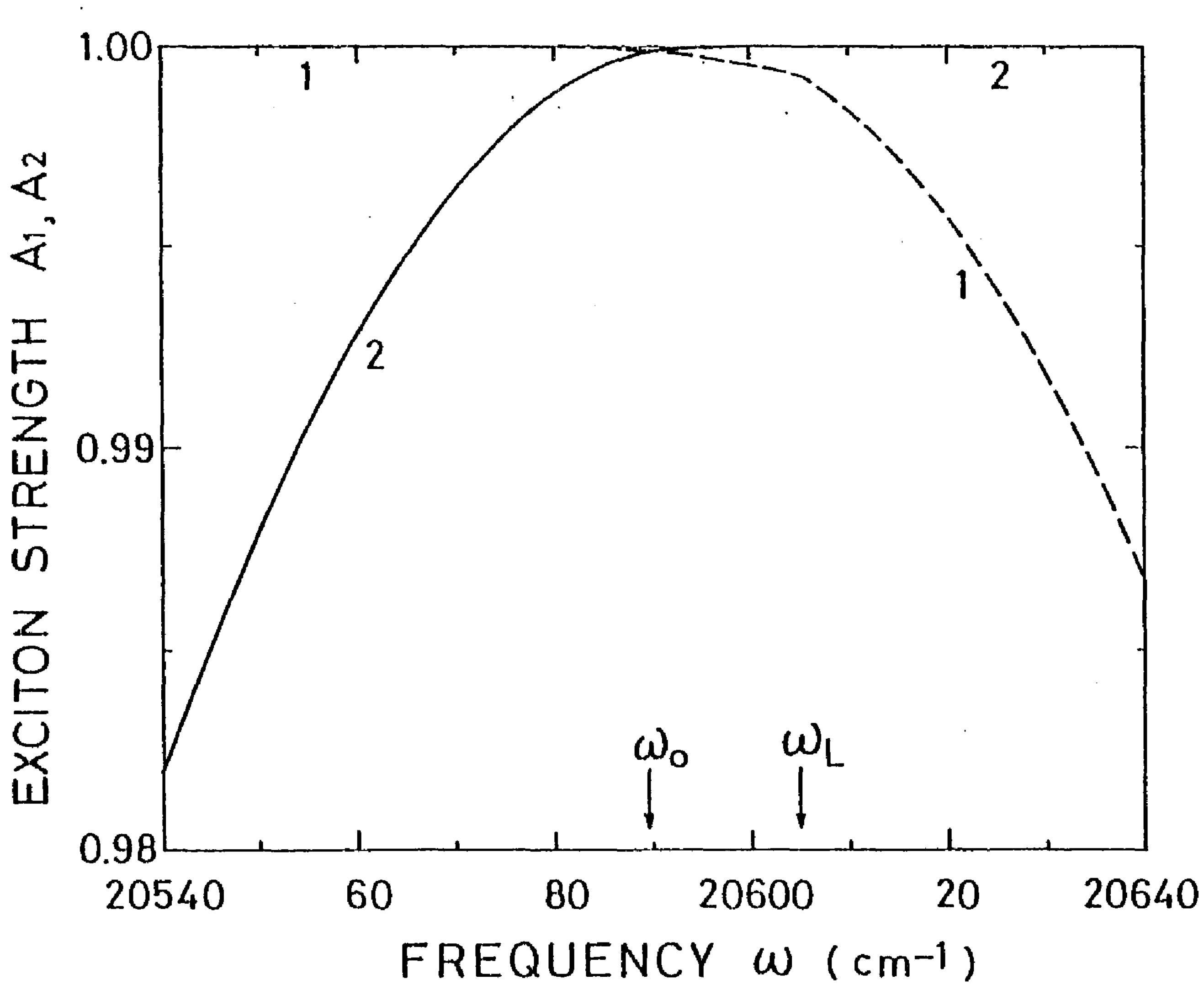
EXCITON STRENGTH A_1, A_2
1.00
0.99
0.98
1
2
2
1
ω_o
ω_L
20540
60
80
20600
20
20640
FREQUENCY ω (cm^{-1})

FIG. 4-4 Schematic representation of the exciton-polariton dispersion curve and the kinematics involved in backward Brillouin scattering. Dots indicate the initial polariton states. The arrows illustrate Stokes (downward) and anti-Stokes (upward) scatterings with incident frequency ω_I.

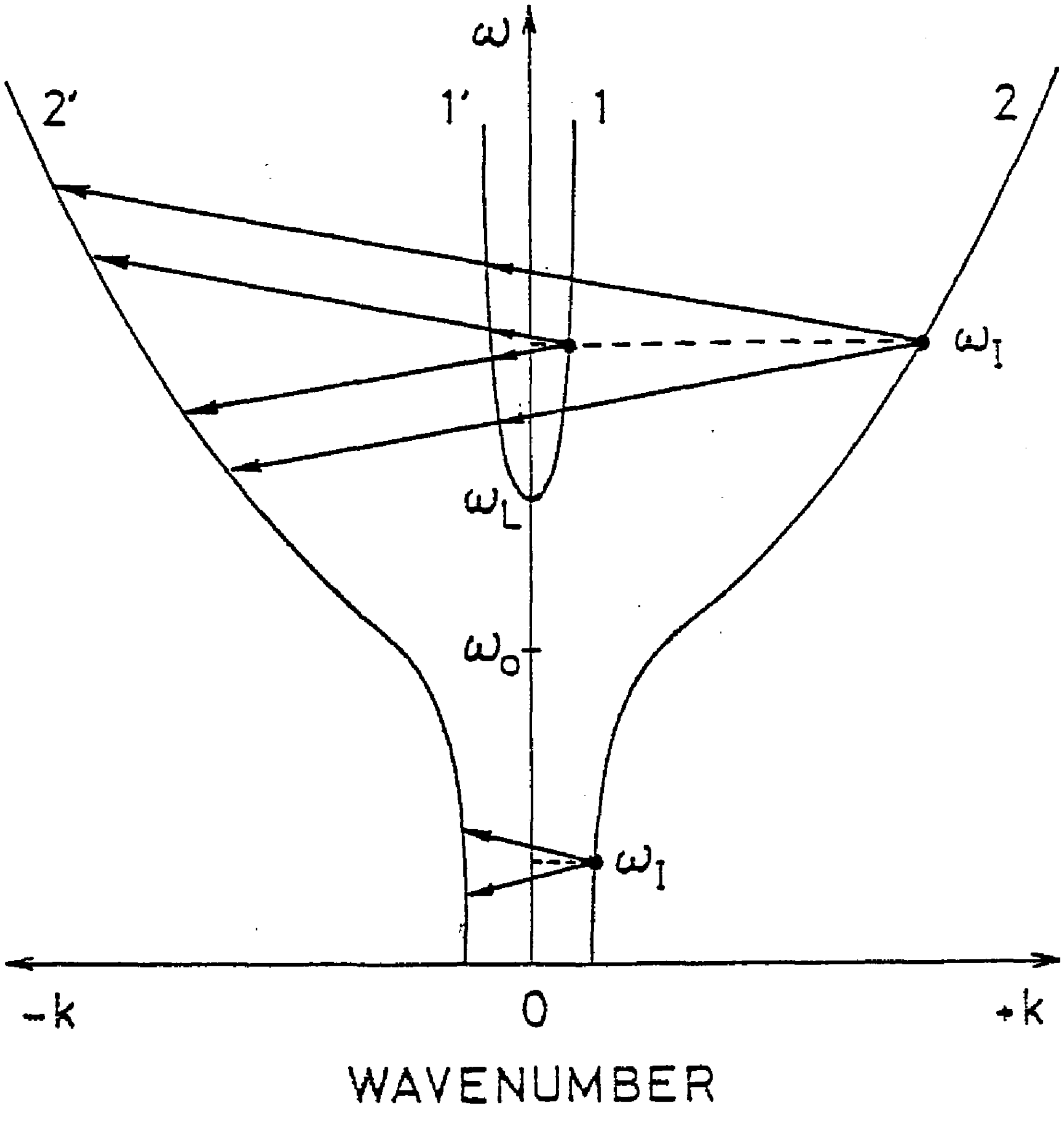
ω
2'
1'
1
2
ω_I
ω_L
ω_o
ω_I
-k
0
+k
WAVENUMBER

3. Transition Probability (Scattering Rate of Polaritons)

An expression for the rate at which polaritons are scattered into a solid angle $d\Omega_{int}$ within the medium has been derived by Burstein et al.(70) This result (which was originally derived for the infinite mass exciton case) is now generalized to the case of spatial dispersion.

$$\left(\frac{d^2N_s}{d\Omega dt}\right)_{int}^{j\leftarrow i} = \frac{2\pi}{\hbar^2} \left|\langle\vec{k}+\vec{q}|H_{pol-ph}^{j\leftarrow i}|\vec{k}\rangle\right|^2 \rho_j(\omega_s)\bar{n}_{Ii}\, V_s \times \begin{cases} 1+n_{ph}(\omega_I-\omega_s) \\ n_{ph}(\omega_s-\omega_s) \end{cases} \quad (4.32)$$

where $\bar{n}_{Ii}$ is the number of incident polaritons per unit volume; N_S is the number of scattered polaritons from mode-i to mode-j; n_{ph} is the occupation number for the acoustic phonons and $\rho_j(\omega_s)$ is the density of states of the mode-j polaritons.

This expression [Eq. 4.32)] represents the application of Fermi's Golden Rule for first order perturbation theory to Eq. (4.14).

The density of states can be written as:.

$$\rho_j(\omega_s) = \frac{\bar{V}}{(2\pi)^3} \frac{(k'_{sj})^2}{|V_{Gj}(\omega_s)|} \quad (4.33)$$

where $v_{Gj}(\omega_s)$ is the group velocity of the mode-j polaritons.

For the backscattering geometry case, the scattering volume V_s may be written as:

$$V_s = \frac{A}{2(k''_{Ii}+k''_{sj})} \quad (4.34)$$

where A is the cross sectional area illuminated by the laser and $2k''_j$ is the attenuation coefficient of the polariton. Substituting Eqs. (4.33) and (4.34) into (4.32) and using the explicit form of the polariton-phonon interaction given by Eq. (4.14) yields:

$$\left(\frac{d^2N_s}{d\Omega dt}\right)_{int}^{j\leftarrow i} = \frac{\pi\, \bar{n}_{Ii}}{(2\pi)^3\hbar^2} \frac{A(k'_{sj})^2|\Gamma_o(q)|^2|A_{ij}(k_{sj},k_{ji})|^2}{|V_{Gj}(\omega_s)|\quad(k''_{Ii}+k''_{sj})} \quad (4.35)$$

$$\times \begin{cases} (n_{ph}+1) & \text{Stokes} \\ n_{ph} & \text{anti-Stokes} \end{cases}$$

4. Internal Scattering Cross Section

The rate of removal of energy from the incident mode-i polariton beam (per unit solid angle per unit time) via the scattering process is:

$$\hbar\omega_I \left(\frac{d^2N_s}{d\Omega dt}\right)^{j\leftarrow i}_{int} \tag{4.36}$$

The mean intensity of the incident mode-i polariton beam inside the crystal is:

$$\hbar\omega_I \; v_{Ei}(\omega_I) \; \bar{n}_{Ii} \tag{4.37}$$

where $v_{E_i}(\omega_I)$ is the energy velocity of the mode-i polariton with frequency ω_I.

Substituting the expression for $\left(\frac{d^2N_s}{d\Omega dt}\right)^{j\leftarrow i}_{int}$ into Eq. (4.36) and then taking the ratio of Eq. (4.36) to Eq. (4.37) results in the internal differential scattering cross section:

$$\left(\frac{d\sigma}{d\Omega}\right)^{j\leftarrow i}_{int} = \frac{A(k'_{sj})^2}{8\pi^2\hbar^2} \frac{|\Gamma_o(q)|^2 \; |A_{ij}(k_{sj},k_{Ii})|^2}{V_{Ei}(\omega_I)|V_{Gj}(\omega_s)| \; (k''_{Ii}+k''_{sj})} \times \begin{cases} [1+n_{ph}(\omega_I-\omega_s)] & \text{Stokes} \\ n_{ph}(\omega_s-\omega_I) & \text{anti-Stokes} \end{cases} \tag{4.38}$$

where both Stokes and anti-Stokes scatterings have been included.

The analytic expression for the energy velocity is given in Appendix A.

5. External Scattering Cross Section

a. General Expression for the Three ABCs

As mentioned in Chap. I, the spatially dispersive medium requires along with Maxwell's boundary conditions, an additional boundary condition to fully describe the electrodynamics governing the simultaneous propagation of two exciton-polariton modes.

The three ABCs most extensively discussed in the literature are listed in Chap. I [Eqs. (1.11) to (1.13)].

These three ABCs can now be written in a very simple general form:

$$a_1 E_1 + a_2 E_2 = 0 \qquad (4.39)$$

where $a_i = n_{c_i}{}^2 - \varepsilon_b$ for ABC 1

$a_i = n_{c_i} (n_{c_i}^2 - \varepsilon_b)$ for ABC 2

$a_i = \dfrac{1}{n_{c_i} - n_e}$ for ABC 3

$i = 1,2$

b. Transmissivity and Reflectivity Expressions

The expressions for the transmissivity and reflectivity of photons (polaritons) traveling across the vacuum-spatial dispersive medium boundary (see Fig.4-1) requires both Maxwell's boundary conditions and an ABC since two polariton modes (for $\omega_I > \omega_L$) can simultaneously propagate in the medium.

Considering the vacuum to medium case first and dealing exclusively with normal incidence, Maxwell's boundary conditions become

$$E_{I_o} + E_{R_o} = E_{T_1} + E_{T_2} \tag{4.40}$$

$$E_{I_o} - E_{R_o} = n_{c_1} E_{T_1} + n_{c_2} E_{T_2} \tag{4.41}$$

where E_{I_o} (E_{R_o}) is the electric field amplitude in vacuum for the incident (reflected) photon and E_{T_1} (E_{T_2}) is the transmitted mode-1 (mode-2) polariton inside the medium.

Combining Eqs. (4.39), (4.40), and (4.41), yield:

$$E_{T_1} = \frac{2a_2}{a_2(1+n_{c_1})-a_1(1+n_{c_2})} \; E_{I_o} \tag{4.42}$$

$$E_{T_2} = \frac{2a_1}{a_2(1+n_{c_1})-a_1(1+n_{c_2})} \; E_{I_o} \tag{4.43}$$

$$E_{R_o} = \frac{a_2(1-n_{c_1})-a_1(1-n_{c_2})}{a_2(1+n_{c_1})-a_1(1+n_{c_2})} \; E_{I_o} \tag{4.44}$$

As in Chap. III, the transmissivity and reflectivity are defined as follows:

$$T \equiv \frac{R_e \bar{S}_T}{R_e \bar{S}_I} \; ; \quad R = \frac{R_e \bar{S}_R}{R_e \bar{S}_I} \tag{4.45}$$

where

$$\bar{S}_I = \frac{c}{8\pi} \, |E_{I_o}|^2 \; ; \quad \bar{S}_R = \frac{c}{8\pi} \, |E_{R_o}|^2$$

However, the calculation of the transmitted Poynting vector is not trivial for the case of spatial dispersion since both the electromagnetic waves and the finite mass excitons (polarization waves) can propagate energy. This expression is derived in Appendix A using a generalized Poynting theorem [see Eq. (A.13)]

$$R_e \bar{S}_{T_i} = \frac{cn_i}{8\pi} \frac{\Gamma}{\Gamma - 2B\omega n_i \kappa_i} \left| E_{T_i} \right|^2 \tag{4.46}$$

Here $n_i = R_e(n_{c_i})$ and $\kappa_i = I_m\ (n_{c_i})$;

Using Eqs. (4.42) - (4.46), the transmissivities (for both polariton modes) and the reflectivity in the vacuum to medium case are

$$T_1 = \frac{n_1 \Gamma}{\Gamma - 2B\omega n_1 \kappa_1} \left| \frac{2a_2}{a_2(1+n_{c_1}) - a_1(1+n_{c_2})} \right|^2 \tag{4.47}$$

$$T_2 = \frac{n_2 \Gamma}{\Gamma - 2B\omega n_2 \kappa_2} \left| \frac{2a_1}{a_2(1+n_{c_1}) - a_1(1+n_{c_2})} \right|^2 \tag{4.48}$$

$$R = \left| \frac{a_2(1-n_{c_1}) - a_1(1-n_{c_2})}{a_2(1+n_{c_1}) - a_1(1+n_{c_2})} \right|^2 \tag{4.49}$$

A similar method is used for the calculation of the transmissivity and reflectivities in the medium to vacuum case (keeping in mind that for $\omega_s > \omega_L$, two reflected polariton modes will be produced at the surface). The transmissivity expression for the mode-i scattered polariton is

$$T_i' = \frac{\Gamma - 2B\omega n_i \kappa_i}{n_i \Gamma} \left| \frac{2(a_1 - a_2) n_{c_i}}{a_2(1+n_{c_1}) - a_1(1+n_{c_2})} \right|^2 \tag{4.50}$$

and the reflectivity expressions for the two reflected polariton modes are:

$$R_1^i = \frac{n_1(\Gamma - 2B\omega n_i \kappa_i)}{n_i(\Gamma - 2B\omega n_1 \kappa_1)} \left| \frac{a_2 - a_i}{a_1 - a_2} + \frac{2a_2 n_{c_i}}{a_2(1+n_{c_1}) - a_1(1+n_{c_2})} \right|^2 \tag{4.51}$$

$$R_2^i = \frac{n_2(\Gamma-2B\omega n_i\kappa_i)}{n_i(\Gamma-2B\omega n_2\kappa_2)} \left|\frac{a_1-a_i}{a_1-a_2} + \frac{2a_1 n_{c_i}}{a_2(1+n_{c_1})-a_1(1+n_{c_2})}\right|^2 \qquad (4.52)$$

Fig. 4-5 shows the curves resulting from the two transmissivity expressions [Eqs. (4.47) and (4.48)] for various ABCs using CdS parameters$^{(60)}$ in Table 4-1.

Fig. 4-6 shows the transmissivity product, $T_2(\omega_I)\,T_2'(\omega_S)$ as a function of incident frequency ω_I for various ABCs and for longitudinal acoustic phonon scattering in CdS.

c. External Scattering Cross Section Expression

The external scattering cross section resulting from polaritons scattering from mode-i to mode-j in the medium is obtained by substituting Eq. (4.38) into Eq. (1.14):

$$\left(\frac{d\sigma}{d\Omega}\right)_{ext}^{j\leftarrow i} = \frac{T_i(\omega_I)T_j'(\omega_s)\ A|\Gamma_o(q)|^2|A_{ij}(k_{s_j},k_{I_i})|^2}{n_j^2(\omega_s)8\pi^2\hbar^2\ V_{Ei}(\omega_I)|\ V_{Gj}(\omega_s)|(k_{Ii}''+k_{sj}'')} \qquad (4.53)$$

$$\times \begin{cases}[1+n_{ph}(\omega_I-\omega_s)] & \text{Stokes}\\ n_{ph}(\omega_s-\omega_I) & \text{anti-Stokes}\end{cases}$$

where $n_{ph}(\omega) = [\exp\left(\frac{\hbar\omega}{k_B T}\right) - 1]^{-1}$

The $n_j^2(\omega_s)$ in the denominator results from the solid angle correction factor [see Eq. (1.15)].

Eq. (4.53) above is dependent on both the incident laser frequency ω_I and the ABCs and can be used for both deformation potential and piezoelectric exciton-phonon interactions [Eqs. (4.18) and (4.23)].

In Chap. VI, Eq. (4.53) will be compared with RBS intensity measurements resulting from different polariton-phonon scatterings [e.g., scattering of a longitudinal acoustic phonon between the outer (2-2') polariton branches].

FIG. 4-5 Numerically calculated vacuum to medium transmissivities of mode-1 and mode-2 polaritons for various ABCs as a function of frequency. The number labeled on each curve corresponds to the ABC specified in Eq. 4-39. Parameter values from Table 4-1 are used with $\Gamma = 1.0\text{cm}^{-1}$.

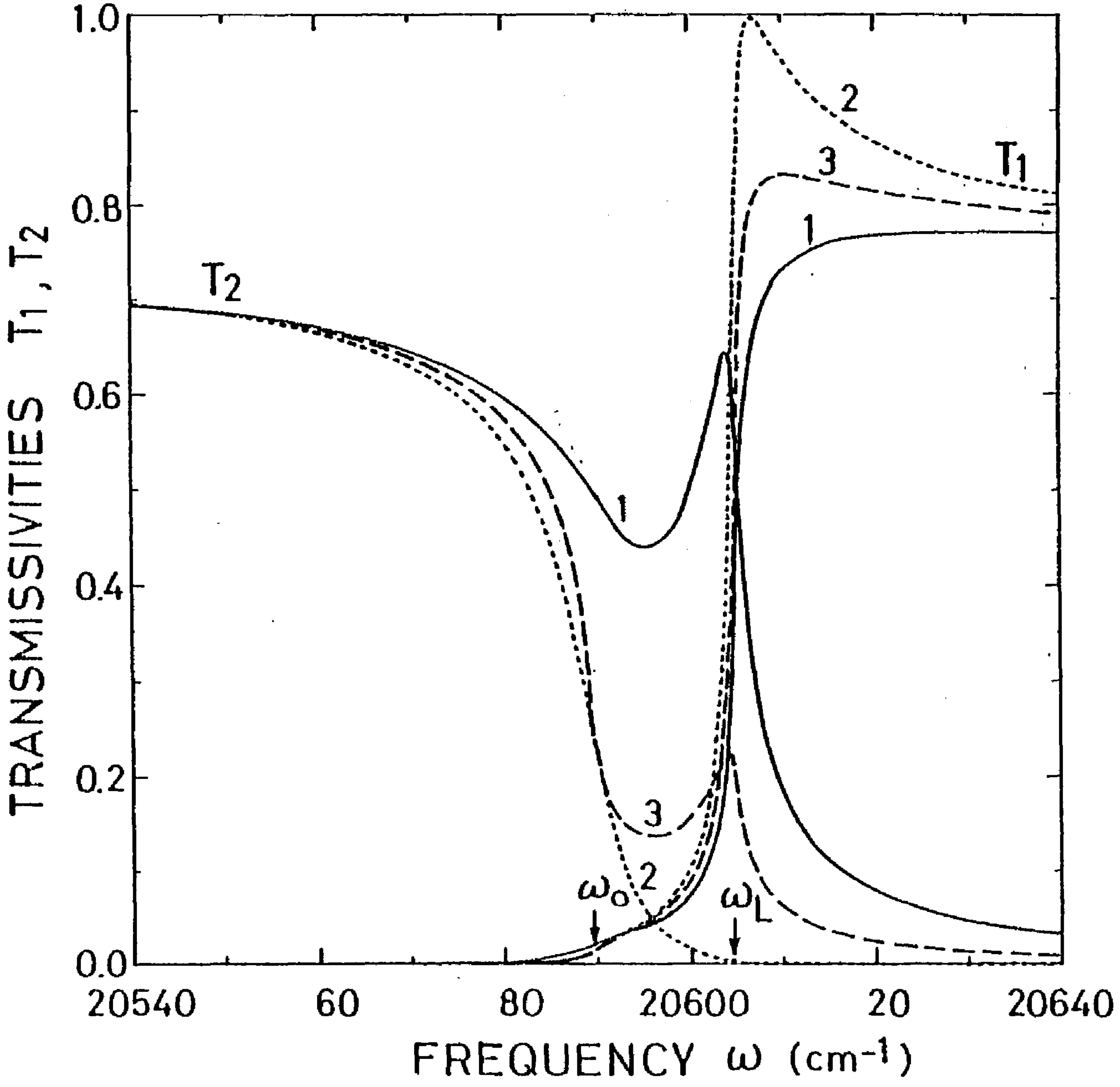
TRANSMISSIVITIES T_1, T_2
1.0
0.8
0.6
0.4
0.2
0.0
20540
60
80
20600
20
20640
FREQUENCY ω (cm^{-1})
T_2
T_1
1
2
3
1
2
3
ω_o
ω_L

FIG. 4-6 The transmissivity product of the incident and scattered mode-2 polaritons, $T_2(\omega_I)\ T_2'\ (\omega_s)$, as a function of incident frequency ω_I. The number labeled on each curve has the same meaning as in Fig. 4-5. Parameter values once again are from Table 4-1 with $\Gamma = 1.0\text{cm}^{-1}$.

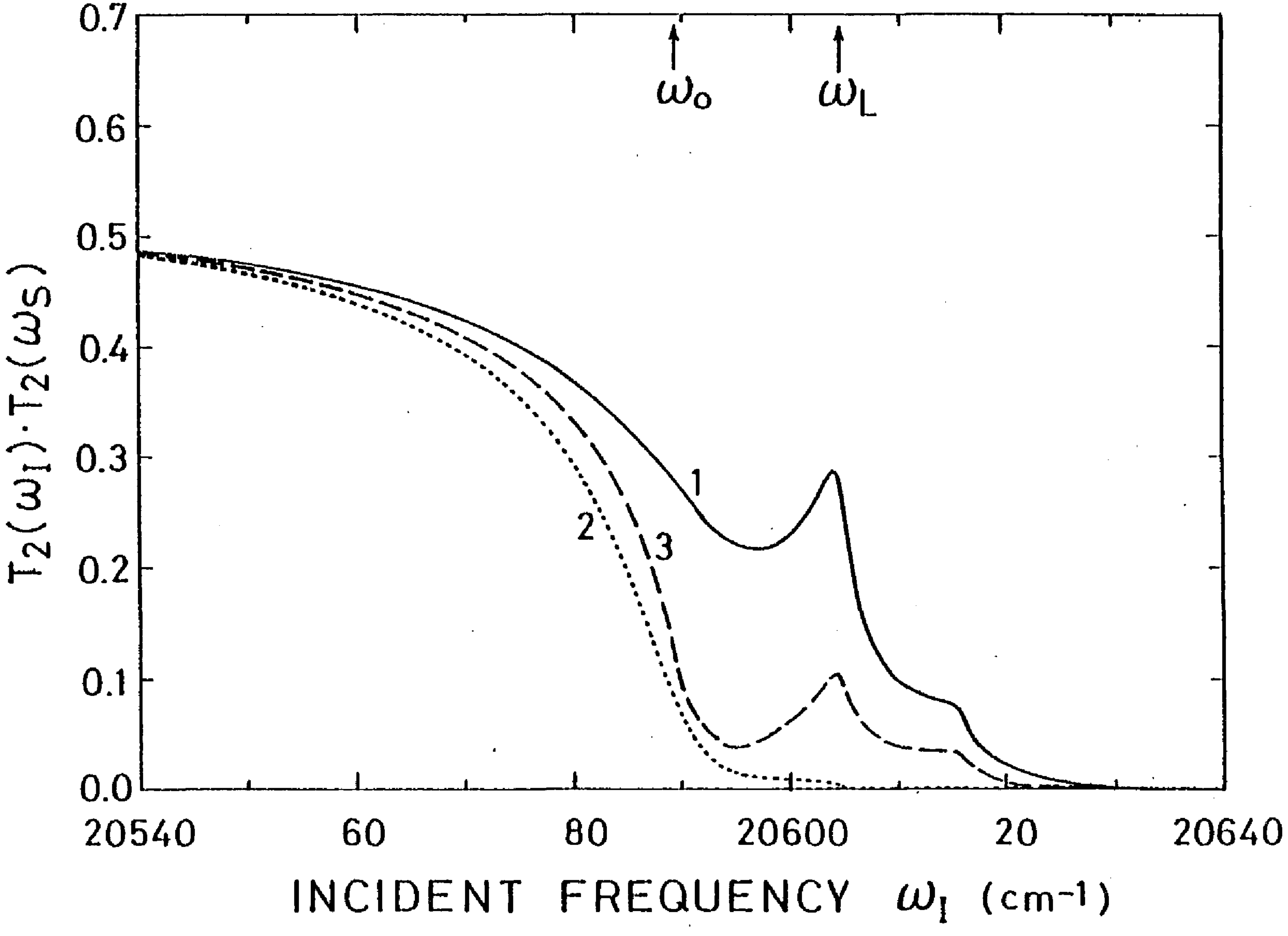
$T_2(\omega_I) \cdot T_2(\omega_S)$
0.7
0.6
0.5
0.4
0.3
0.2
0.1
0.0
20540
60
80
20600
20
20640
INCIDENT FREQUENCY ω_I (cm^{-1})
ω_o
ω_L
1
2
3

CHAPTER V

EXPERIMENT

A. INTRODUCTION

Laser Brillouin spectroscopy involves the following experimental arrangement. A beam of laser light is focused into a small volume of the sample to be studied. Light scattered from the sample, which contains a number of frequency components, is collected and frequency analyzed by a Fabry-Perot interferometer and/or tandem grating spectrometer. Elastic scattering usually produces the most intense component which is at the frequency of the laser light. Inelastic components appear at frequencies shifted with respect to the laser frequency on both the Stokes (low frequency) and anti-Stokes (high frequency) sides. Of interest in Brillouin scattering experiments are the frequency shifts, intensities and linewidths of the shifted components within 10-cm^{-1} of the laser frequency.

Reflectance measurements are performed on samples in the frequency region of electronic transitions. Light from a white light source is focused onto the sample in a near normal incidence scattering geometry. Reflected light is analyzed by a double-grating spectrometer. Of interest in the reflection spectrum are the shape, height and frequency position of the reflection maxima as well as the frequency distance between these maxima and their corresponding minima.

B. RBS EXPERIMENTS

1. Experimental Setup

The experimental arrangement used for the RBS studies is shown in Fig. 5-1. A krypton ion laser was used to pump a cw dye laser in order to obtain tunable single mode output radiation. The dye laser output was monitored via a pair of beamsplitters in order to (i) maintain a constant dye output power through the use of a dye laser light stabilizer; and (ii) monitor the mode spectrum of the output radiation using an optical spectrum analyzer and an oscilloscope. The light was then passed through a polarization rotator to obtain the desired polarization before being focused onto the sample.

The samples used were vapor-grown single crystal CdS platelets generously provided by Wright-Patterson and General Motors (GM). The crystals, with the crystallographic c-axis in the plane of the sample, had typical surface area dimensions of 3mm x 5mm with thicknesses $\sim 10^{-2}$cm. The sample was attached to a copper mount in the helium dewar via a grease mixture.

A backward light scattering geometry was used with incident wavevector of the dye laser light perpendicular to the surface of the crystal platelet ($\vec{k}\perp\hat{c}$). Light scattered by the sample was collected and focused onto a pinhole by a Nikon camera lens. A second Nikon lens then collimated the light emitted from the pinhole which acted as a point source. The parallel light so obtained was reflected from a system of two mirrors which served the purpose, along with the Nikon collimating lens, of aligning the collected light with the triple-pass Fabry-Perot interferometer. The light emerging from the ramped Fabry-Perot was then focused onto the vertical spectrometer slits which, along with a brass horizontal slit, formed a second pinhole. The speed of the lens used was chosen to match that of the spectrometer.

FIG. 5-1 Schematic of RBS experimental arrangement. L_1, L_2, L_3 and L_4 are sample focussing, pinhole focussing (Nikon), Fabry-Perot collimating (Nikon) and spectrometer focussing lenses respectively. Focal lengths of these lenses are 13 cm, 5.5 cm, 5.5 cm and 18.7 cm, respectively. Pinholes P_1 and P_2 have diameters of 200 and 150 microns, respectively.

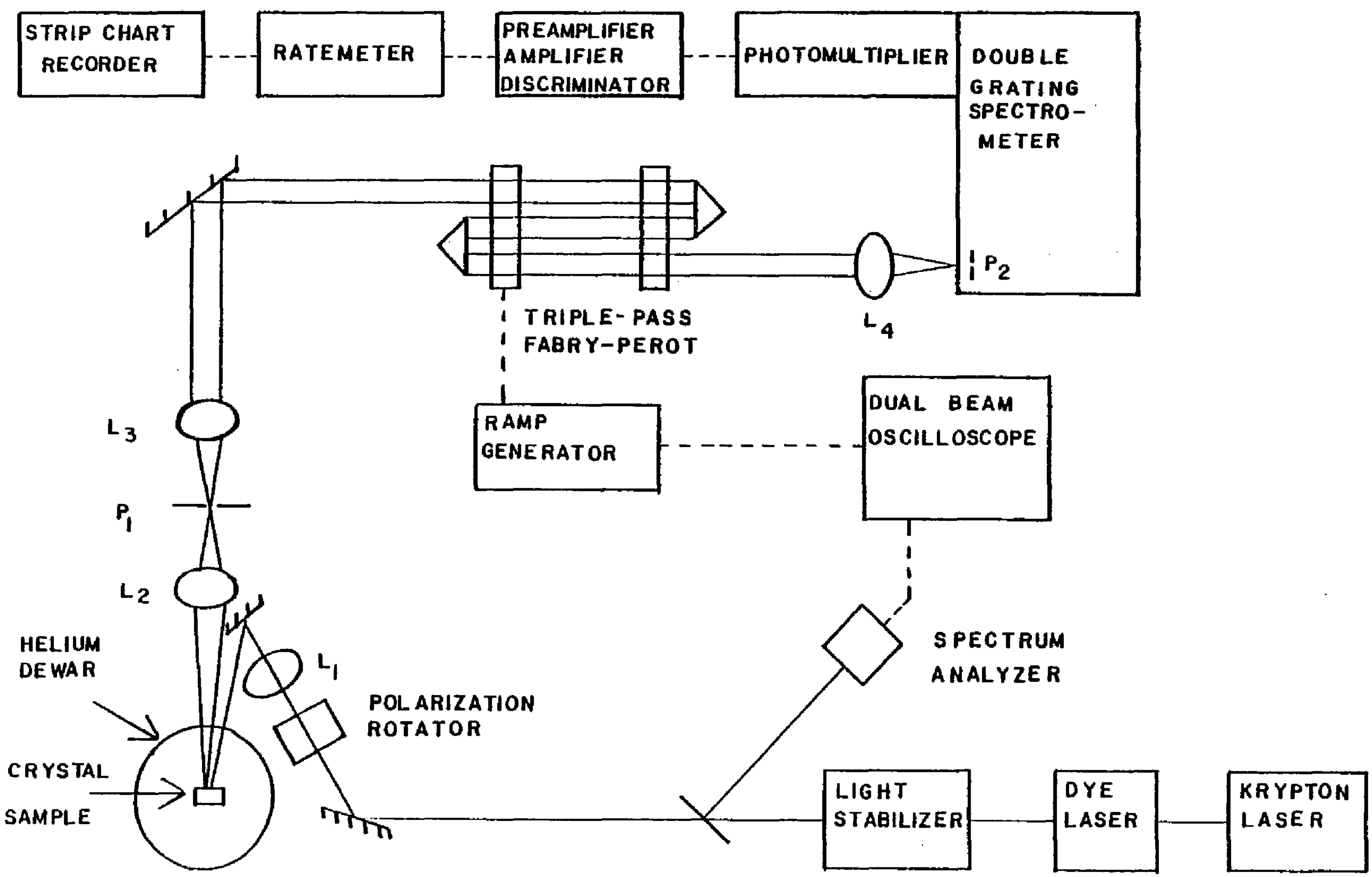
STRIP CHART RECORDER
RATEMETER
PREAMPLIFIER AMPLIFIER DISCRIMINATOR
PHOTOMULTIPLIER
DOUBLE GRATING SPECTRO-METER
P_2
L_4
TRIPLE-PASS FABRY-PEROT
RAMP GENERATOR
DUAL BEAM OSCILLOSCOPE
L_3
P_1
L_2
HELIUM DEWAR
L_1
POLARIZATION ROTATOR
SPECTRUM ANALYZER
CRYSTAL SAMPLE
LIGHT STABILIZER
DYE LASER
KRYPTON LASER

Light leaving the spectrometer was focused onto the cathode of a photomultiplier tube whose output was processed with photon counting electronics and recorded on a stripchart recorder, or occasionally multiscaled into a PDP-8E minicomputer.

2. Apparatus

A summary of the apparatus used in the RBS experiments is given in Table 5-1. Brief descriptions of the main components are given below.

Krypton Laser. A Spectra Physics model 171 krypton ion laser was used as a pump laser. The output power was between 2.0 and 2.5 watts for all lines in the deep blue (4067-4226Å). The output mode was TEM_{oo}. This laser was operated on the light control mode whereby its power supply current was constantly adjusted by an external dye laser light stabilizer (see below).

Dye Laser.(76) The output of the krypton laser was used to pump a Coherent Radiation model 590 dye laser in order to obtain a source of continuously tunable coherent single mode light. The dye medium was a methyl alcohol-ethylene glycol solution of the dye coumarin 480 which absorbs in the band 4000Å to 4200Å and emits at longer wavelengths 4700Å to 5150Å through fluorescence. Selection of monochromatic radiation from the broad dye fluorescence bandwidth is achieved through the use of a quartz birefringent filter consisting of three quartz plates of different thicknesses placed in the cavity at Brewster's angle. In addition, a double etalon system consisting of a thick (10mm) coated etalon and a thin (0.5mm) coated etalon was used to obtain a single mode monochromatic output with a frequency width of less than 100 MHz ($<0.003cm^{-1}$).

TABLE 5-1 LIST OF APPARATUS

Apparatus	Manufacturer	Model
Krypton laser	Spectra Physics	171
Dye laser	Coherent Radiation	590
Dye laser light stabilizer	Spectra Physics	373
Spectrum analyzer	Coherent Optics	470
Dual beam oscilloscope	Tektronix	556
Helium dewar	Janis	8DT
Fabry-Perot interferometer	Burleigh Instruments	RC-110
Ramp generator	Burleigh Instruments	RC-44
Double-grating spectrometer	Spex	1401
Photomultiplier tube	ITT	FW130
Refrigeration unit	Products for Research	TE-104
Power supply	Power Designs, Inc.	AK-20
Nim bin	Berkeley Nucleonics	AP.1
Preamplifier, Amplifier, Discriminator	Canberra	813
Ratemeter	Ortec	441
Strip chart recorder	Honeywell	194

Tuning of the output frequency was accomplished as follows: frequency changes on the order of a thin etalon mode hop (6-7cm^{-1}) were obtained by rotating the birefringent filter about its surface normal. Small frequency changes were made by tilting the thin etalon with respect to the cavity beam enabling the laser frequency to hop between thick etalon modes (0.3cm^{-1} changes).

Certain instabilities in the output frequency spectrum of the dye laser complicated the RBS experiments, the most important of which was the fluctuation of the output power which introduced thin etalon mode hopping. This problem was partially alleviated by incorporating a light stabilizer into the experimental setup. However, mode hops still occurred on the average of one every five minutes. Thus, the output mode spectrum of the dye laser had to be continuously monitored by a spectrum analyzer (see below) so that undesirable modes could be eliminated through the tilting of the thin etalon.

Dye Laser Light Stabilizer. The dye laser power was maintained at a 15mW output by the dye laser light stabilizer (Spectra Physics, model 373). This consisted of a detector head and a control unit. The detector head contained a beamsplitter which reflected 3.5% of the laser light onto a photocell detector. The signal created by the photocell (0.75μ A/mW) was amplified and compared with a DC reference signal specified by the level control (located on the front of the control unit) which set the desired operating power level of the light stabilizer. The amplified difference of the two signals produced a current that was returned to the krypton ion laser control circuitry which then compensated for the dye laser power variations by changing the pump laser output power.

The power output of the dye could be stabilized to within ±0.5% per hour for a fixed wavelength. In addition, the light stabilizer also acted as a power meter with its meter accurate to within ±10%.

Spectrum Analyzer. The spectrum of the dye laser light was observed with an optical spectrum analyzer (Coherent Optics, model 470) in conjunction with an oscilloscope (Tektronix, dual beam model 556) and an amplifier (Keithley Instruments, model 102C). The oscilloscope was used to both ramp the spectrum analyzer and display its amplified output. The free spectral range of the spectrum analyzer was 8GHz ($\sim 0.27\text{cm}^{-1}$).

Cryogenic System. The samples were vertically attached to a hexagonally shaped copper sample mount via a conductive vacuum grease mix consisting of crycon and N-grease. The sample mount was then placed in a Janis "Supervaritemp" liquid helium dewar (model 8DT). Optical access to the sample was provided by fused quartz windows on the dewar. Cooling of the sample was achieved by helium exchange gas flowing over the copper sample mount and by conduction between the sample and the mount. Temperature was measured using a copper-constantan thermocouple which was in thermal contact with the sample mount. Most experiments were performed at 4.2°K. Occasionally the liquid helium was allowed to fill the sample space and was pumped to obtain temperatures of 2.7°K.

Fabry-Perot Interferometer.(77) A triple-pass Fabry-Perot interferometer (Burleigh Instruments, model RC-110) was used for high resolution spectral analysis of the scattered light. This Fabry-Perot used two plane mirrors which were coated for 93% reflectivity in the spectral region 4500-5500Å and had $\lambda/200$ flatness. Piezoelectric ceramic transducers (PZT) were used to scan and align one of the plane mirrors with respect to the other mirror which remained fixed. The ramp voltage (0 to 1000 volts, sawtooth in time) applied in the scanning mode to each of the PZT elements was supplied by a Burleigh ramp generator (model RC-44). Two corner-cube retro-reflectors were utilized to obtain triple-pass operation. Several free spectral ranges (FSR) ranging from 2-13.5cm^{-1} were used. The finesse of the interferometer varied between 40 and 60 with a contrast of ~1x10^{6}.

Double Grating Spectrometer. After passing the interferometer the scattered light also traversed a 3/4 meter Spex model 1401 Czerny-Turner double grating spectrometer. The spectrometer served two purposes:

(i) determined the incident dye laser frequency by scanning the scattered Rayleigh light and (ii) acted as a tunable laser filter allowing only Rayleigh and Brillouin components to pass during the Fabry-Perot scan.

Photomultiplier Tube. The light leaving the spectrometer was focused onto the cathode of an ITT FW130 photomultiplier tube. The tube was maintained at -20°C by a model TE-104 thermoelectric refrigeration unit manufactured by Products for Research. The dark count of the cooled tube was about 3 counts/second. A Power Designs, Inc. model AK-20 power supply provided 1750 volts to the photomultiplier tube.

Photon-Counting Electronics. The photon-counting electronics comprised a "PAD" (Canberra, model 813) which combines a preamplifier, amplifier and discriminator in a single nim bin module. The output of the discriminator was fed to a ratemeter (Ortec, model 441) and recorded on a stripchart recorder (Honeywell, model 194).

3. Experimental Procedure(78)

The RBS experiments utilized a backscattering geometry with both the wavevector and polarization of the incident light perpendicular to the c-axis of the crystal ($\vec{k}\perp\hat{c}$, $\vec{E}\perp\hat{c}$). The incident power was maintained at 15mW by the dye laser light stabilzer discussed earlier.

The experimental procedure will now be described. The dye laser was first tuned to some frequency in the vicinity of the A-exciton in CdS (~20588cm^{-1}). During this time, the output of the 8GHz spectrum analyzer was carefully viewed on the oscilloscope in order to verify that the dye laser output consisted of a single frequency. The laser frequency was determined by allowing the Fabry-Perot interferometer to quickly ramp through its free spectral range (FSR)† with a ramp duration of 20 msec. Since the elastic Rayleigh component is dominant in the output of the Fabry-Perot, the laser frequency can be obtained by slowly scanning the grating spectrometer with narrow slitwidths over this elastic component. The slow scan (7.5cm^{-1}min^{-1}) allowed the experimenter to mark the strip chart record in 1cm^{-1} intervals by visual comparison with the spectrometer wavenumber indicator. Subsequent interpolation between the 1cm^{-1} marks allowed the laser frequency to be determined to the nearest 0.1cm^{-1}. Measurements made in this way were reproducible to about 0.2cm^{-1} (the calibration of the spectrometer was checked twice each day an experiment was conducted). After the frequency was determined, the spectrometer slits were opened to provide a

---

† The FSR is determined by the spacing d in cm between the Fabry-Perot mirrors and is given by the expression:

$$FSR = \frac{1}{2d}$$

in units of wavenumbers.

passband slightly larger than the FSR of the Fabry-Perot. The gratings of the spectrometer were then positioned so that either the Stokes or anti-Stokes Brillouin components would be passed by the spectrometer. The Fabry-Perot was then scanned through its FSR in ~100 seconds and the output of the combined Fabry-Perot-spectrometer system was recorded on a strip chart recorder. The frequency of the dye laser was then changed by tilting the thin etalon as previously described. The above procedure was then repeated. The end result was a series of Stokes and anti-Stokes Brillouin spectra for a range of dye laser frequencies through the A-exciton resonance region.

Fig. 5-2 gives an illustrative comparison between the RBS spectra obtained using the combined Fabry-Perot interferometer-grating spectrometer system, using the procedure described above, and the spectra resulting from a scanning grating spectrometer, the latter technique having been used in most of the previous RBS experiments. The Stokes (b) and anti-Stokes (c) TA(2-2') components are clearly resolved when the combined system is used (effective resolution ~0.15cm^{-1}) whereas the spectra recorded by the grating spectrometer alone (a) shows Stokes TA components which are not completely resolved while the anti-Stokes TA components are obscured by the wing of the Rayleigh line.

The FSR of the Fabry-Perot was chosen in such a way that the Brillouin components resulting from the scattering process could be easily observed. For example, to observe intrabranch scattering from the upper polariton branch (i.e., 1-1' scattering) a FSR equal to 2.11cm^{-1} was used.

FIG. 5-2 Brillouin spectrum of CdS with $\omega_i = 20584$ cm^{-1}, analyzed with; (a) double-grating spectrometer alone; (b) and (c) Fabry-Perot interferometer and grating spectrometer in series. For the Stokes (b) and anti-Stokes (c) high resolution spectra, the free spectral range of the Fabry-Perot was 6.1 cm^{-1} and the grating slits were adjusted to give the passband indicated in (a). The Brillouin components result from LA(2-2') and TA (2-2') scattering.

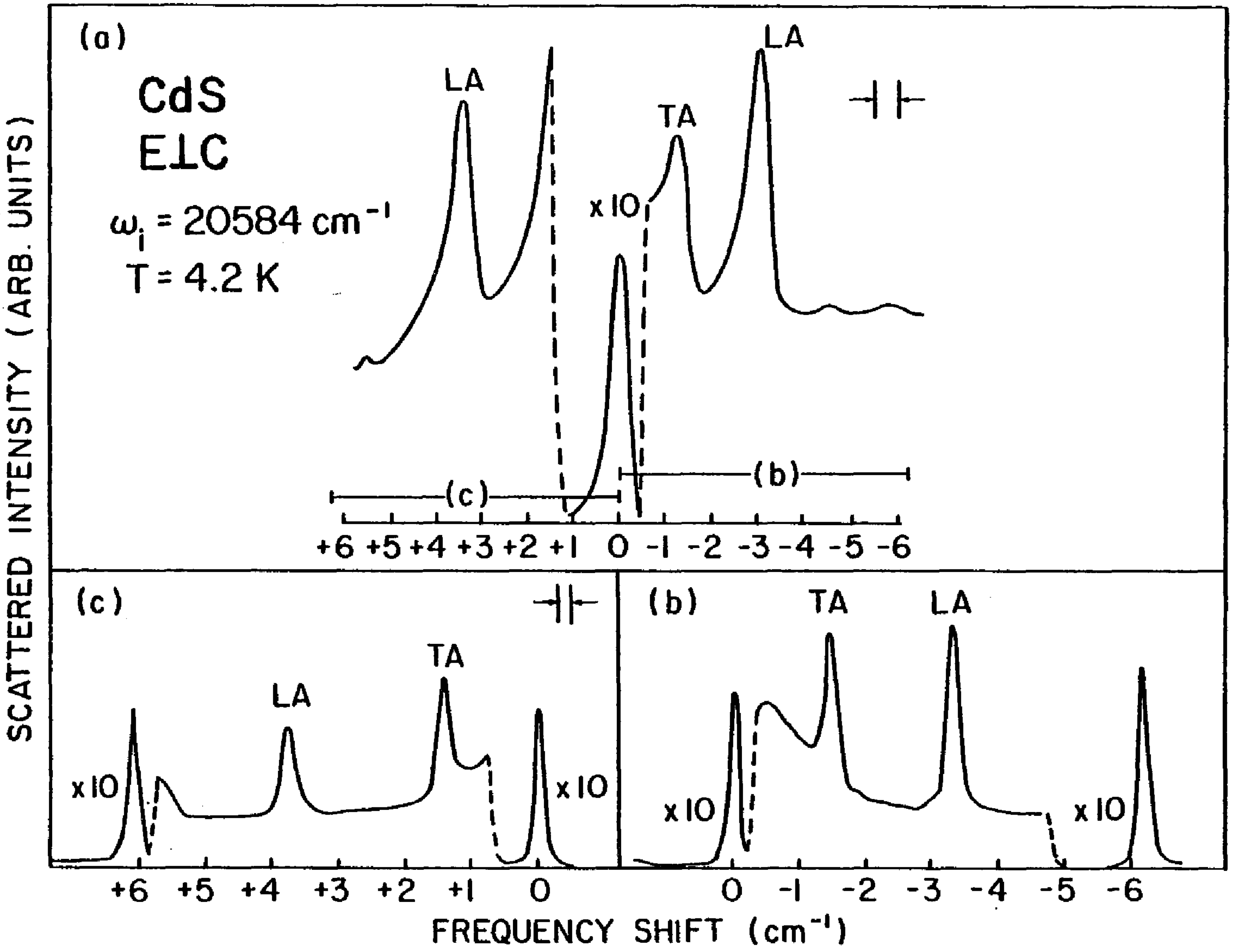
(a)
CdS
E⊥C
$\omega_i = 20584\ \mathrm{cm}^{-1}$
T = 4.2 K
LA
LA
TA
x10
(c)
(b)
+6 +5 +4 +3 +2 +1 0 -1 -2 -3 -4 -5 -6
(c)
LA
TA
x10
x10
(b)
TA
LA
x10
x10
+6 +5 +4 +3 +2 +1 0
0 -1 -2 -3 -4 -5 -6
SCATTERED INTENSITY (ARB. UNITS)
FREQUENCY SHIFT (cm^{-1})

The FSR of the Fabry-Perot was usually determined by deliberately allowing two thin etalon modes to be present in the dye laser output. This light was then scattered off a piece of teflon located within the helium dewar. The separation between these two modes was obtained by scanning the grating spectrometer over the scattered light. This turned out to be ~6.7cm^{-1}. The spectrometer was then positioned midway between the two modes while its slits were opened to pass both of them. The Fabry-Perot then scanned the modes, the spectrum of which was recorded on a strip chart recorder. Since the separation between the modes was known, the FSR could be determined from the strip chart record. A second method was to use a standard mercury or sodium doublet, (e.g., for Hg: 5789.66Å and 5790.66Å) instead of two adjacent thin etalon modes from the dye laser.

C. REFLECTIVITY EXPERIMENTS

1. Experimental Setup(27)

The experimental arrangement for the reflectivity studies is shown in Fig. 5-3. A tungsten lamp which operated at seven amps and nine volts dc acted as the white light source in the experiment. The power for the lamp was supplied by a Deltron regulated power supply (model H3615). The light first passed through an infrared filter (Corning, CS 1-75) before being focused onto a pinhole by a Nikon camera lens. Light emanating from the pinhole passed through a blue filter (Corning, CS 4-96) which transmitted light in the wavelength region 3800Å-5500Å (transmissivity of this filter was 85% in the range 4200Å-5200Å which easily covered the frequencies of the A and B excitons in CdS at a temperature of

FIG. 5-3 Schematic of reflectivity experimental arrangement. L_1, L_2, L_3, L_4 and L_5 are pinhole (P_1) focussing, pinhole collecting, sample focussing, sample collecting and spectrometer focussing lenses respectively. Focal lengths are 5.5 cm (Nikon), 25.4 cm, 33.6 cm, 19.1 cm and 18.7 cm, respectively. Pinholes P_1 and P_2 are 1 mm and 150 microns, respectively. F_1 and F_2 correspond to the infrared and blue Corning filters.

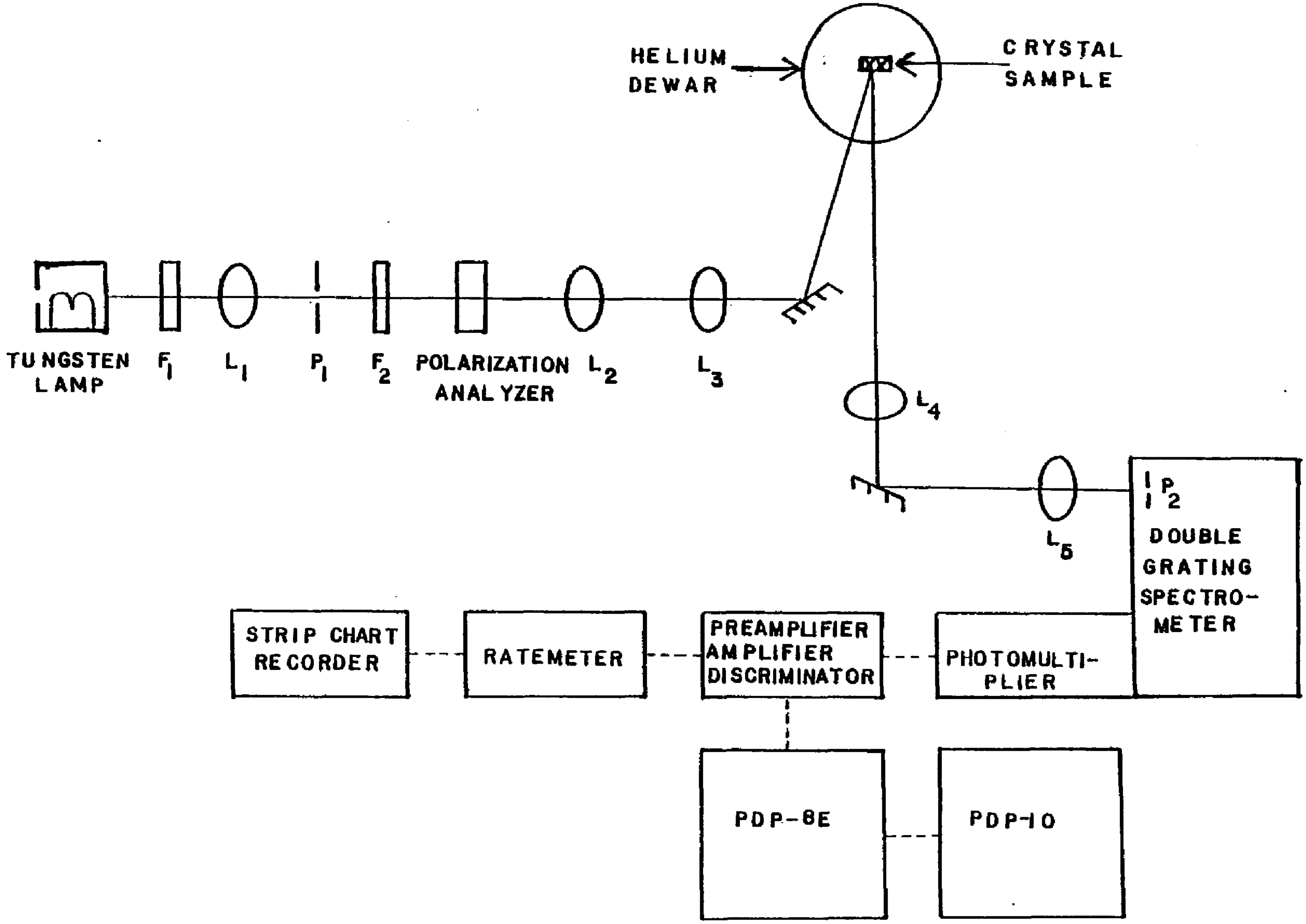
HELIUM DEWAR
CRYSTAL SAMPLE
TUNGSTEN LAMP
F_1
L_1
P_1
F_2
POLARIZATION ANALYZER
L_2
L_3
L_4
L_5
P_2
DOUBLE GRATING SPECTROMETER
STRIP CHART RECORDER
RATEMETER
PREAMPLIFIER AMPLIFIER DISCRIMINATOR
PHOTOMULTIPLIER
PDP-8E
PDP-10

4.2°K). After passing through a polarizer which allowed the light to be polarized either perpendicular or parallel to the crystal c-axis, the light was collimated and then focused onto the CdS sample vertically mounted in the Janis helium dewar. The spot size on the crystal was approximately 1mm. The wavevector of the incident light was perpendicular to the c-axis and formed an angle of about 5° with the surface normal of the sample. The reflected beam was collimated and focussed onto a pinhole in the double grating spectrometer using similar optics as in the case of the RBS experiments. The photoelectric counts resulting from the amplified and discriminated photomultiplier signal were then stored in a PDP-8E DEC minicomputer which operated as a multichannel analyzer.

2. Experimental Procedure

Reflectivity experiments were performed on the same CdS crystals used in the RBS experiments. The experimental procedure consisted of scanning the double grating spectrometer over a specific frequency range of the reflected light. This range was from 20816.2cm^{-1} to 20478.7cm^{-1} and included the n=1 frequencies of both the A and B excitons for CdS crystals at liquid helium temperature.

Each experimental run lasted for nine minutes with the spectrometer scanning at a rate of 37.5$\text{cm}^{-1}\text{min}^{-1}$. The photoelectric counts resulting from the frequency scan were stored in the 512[†] channels of a PDP-8E minicomputer which itself was scanning at a clock rate of 1.08 seconds/channel (this corresponded to a frequency rate of 0.675cm^{-1}/channel). The spectrometer and minicomputer scans were initiated simultaneously.

[†] Each channel contains two 12 bit words.

The contents stored in the memory of the minicomputer after each nine minute scan were then transferred to a PDP-10 computer and stored in a digital file. Similar frequency scans were also conducted on light reflected from a small mirror which was attached to the same copper mount as the CdS samples in the helium dewar. Such experimental runs were necessary in order to eliminate the spectral dependence of the experimental apparatus. The background level for both the crystal and mirror reflectivity spectra was determined by blocking the light entering the spectrometer over a specific frequency interval during each experimental run. Digital files of absolute reflectivity, which resulted from the normalized ratio of the crystal to mirror reflectivity spectra, were subsequently used for least-squares-fitting analysis. Results of this analysis are given in Chap. VI.

CHAPTER VI

RESULTS

A. INTRODUCTION

This chapter contains the results of experiments conducted in the course of the present research. As discussed in Chap. V, the experiments were of two types. The first type used resonant Brillouin scattering to study one phonon scattering processes from exciton-polaritons near the A-exciton in cadmium sulphide. These experiments resulted in measurements of the Brillouin shift, linewidth and external scattering cross sections of various longitudinal and transverse Brillouin components. Comparisons between these measurements and the theoretical expressions derived in Chap. IV are given in Section B. The second type of experiment compared the reflectivity measurements over the A-exciton resonance with the theoretical reflectivity expression which used parameters obtained through the RBS analysis. This discussion is given in Section C. Both the RBS and reflectivity results utilized the three ABCs in their respective analysis. These two experiments were further supplemented by optical density measurements given in Section D. All experiments were performed on the same CdS sample, a platelet grown by vapor transport at the General Motors Research Laboratory, provided by Dr. D. M. Roessler.

B. RBS RESULTS

1. Brillouin Shifts

As noted in Chap. V, the RBS experiments were performed with both the incident wavevector and polarization perpendicular to the crystal c-axis. Two illustrations of Stokes Brillouin spectra are given in Figs. 6-1 and 6-2 with the free spectral range (FSR) of the Fabry-Perot equal to 12.63 cm^{-1} and 2.11 cm^{-1} respectively. These illustrations clearly show (1-2' and 2-1') interbranch and (1-1') intrabranch acoustic phonon scattering processes which had not been observed in previous RBS experiments on CdS(28, 30).

Fig. 6-3 shows all the observed one-phonon Brillouin shifts obtained from a single CdS crystal sample (21E-2). Three free spectral ranges of the Fabry-Perot were employed: 2.11 cm^{-1}, 5.87cm^{-1} and 12.63 cm^{-1}. The solid lines through the data points represent the best fit of the theoretical Brillouin shift [Eq. (4.31)] to the data by non-linear least squares fitting procedure. The four exciton parameters resulting from the fit, along with the longitudinal and transverse sound velocities, are listed in Table 6-1. Also included in this table are the best fits obtained by Winterling and Koteles(60). It should be noted that the theoretical Brillouin shifts are independent of the exciton damping constant Γ (chosen here to be 0.5 cm^{-1}) for $0 \leq \Gamma < 5 cm^{-1}$.

2. Brillouin Linewidths

The theoretical analysis of BZB(1) predicted that the linewidth of the Brillouin components should increase as the incident laser frequency approaches the exciton resonance from below. The exciton damping constant Γ, seen in the polariton dispersion relation [Eq. (4.25)] is responsible for the linewidth increase of these components. Broadening of both the LA and TA (2-2') components was observed in the RBS experiments. Fig. 6-4 shows the approximate full width at half maximum Δ of the Stokes TA (2-2') components determined by subtraction of the instrumental linewidth (FWHM of the Rayleigh line) from the

FIG. 6-1 Brillouin spectrum of CdS with $\omega_I = 20612.3\text{cm}^{-1}$. The Fabry-Perot free spectral range was 12.63cm^{-1} with the spectrometer set to pass Stokes Brillouin components. These one phonon components result from LA (1-1'), TA $\begin{pmatrix}1\text{-}2' \\ 2\text{-}1'\end{pmatrix}$, TA (2-2'), LA (1-2') and LA (2-2'). The large unlabeled peak illustrates two phonon scattering.

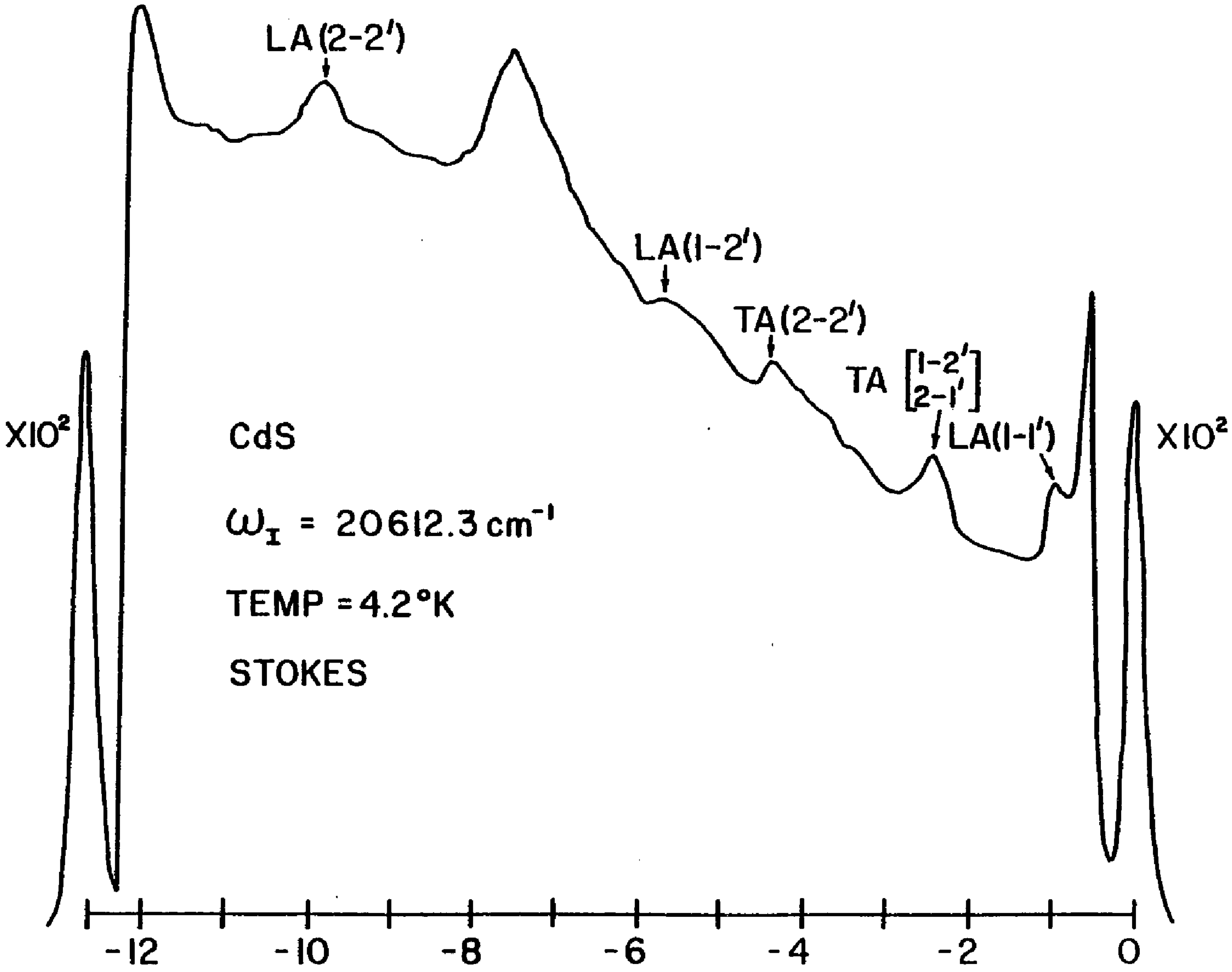
LA(2-2′)
LA(1-2′)
TA(2-2′)
TA [1-2′ 2-1′]
LA(1-1′)
X10²
X10²
CdS
ω_I = 20612.3 cm⁻¹
TEMP = 4.2°K
STOKES
-12
-10
-8
-6
-4
-2
0

FIG. 6-2 Brillouin spectrum of CdS with $\omega_I = 20613.6\mathrm{cm}^{-1}$. The Fabry-Perot FSR equaled $2.11\mathrm{cm}^{-1}$ with the spectrometer set to pass Stokes Brillouin components. These Brillouin components result from LA (1-1') and TA (1-1') scattering. Hatched region of LA (1-1') component represents the area measured by a planimeter.

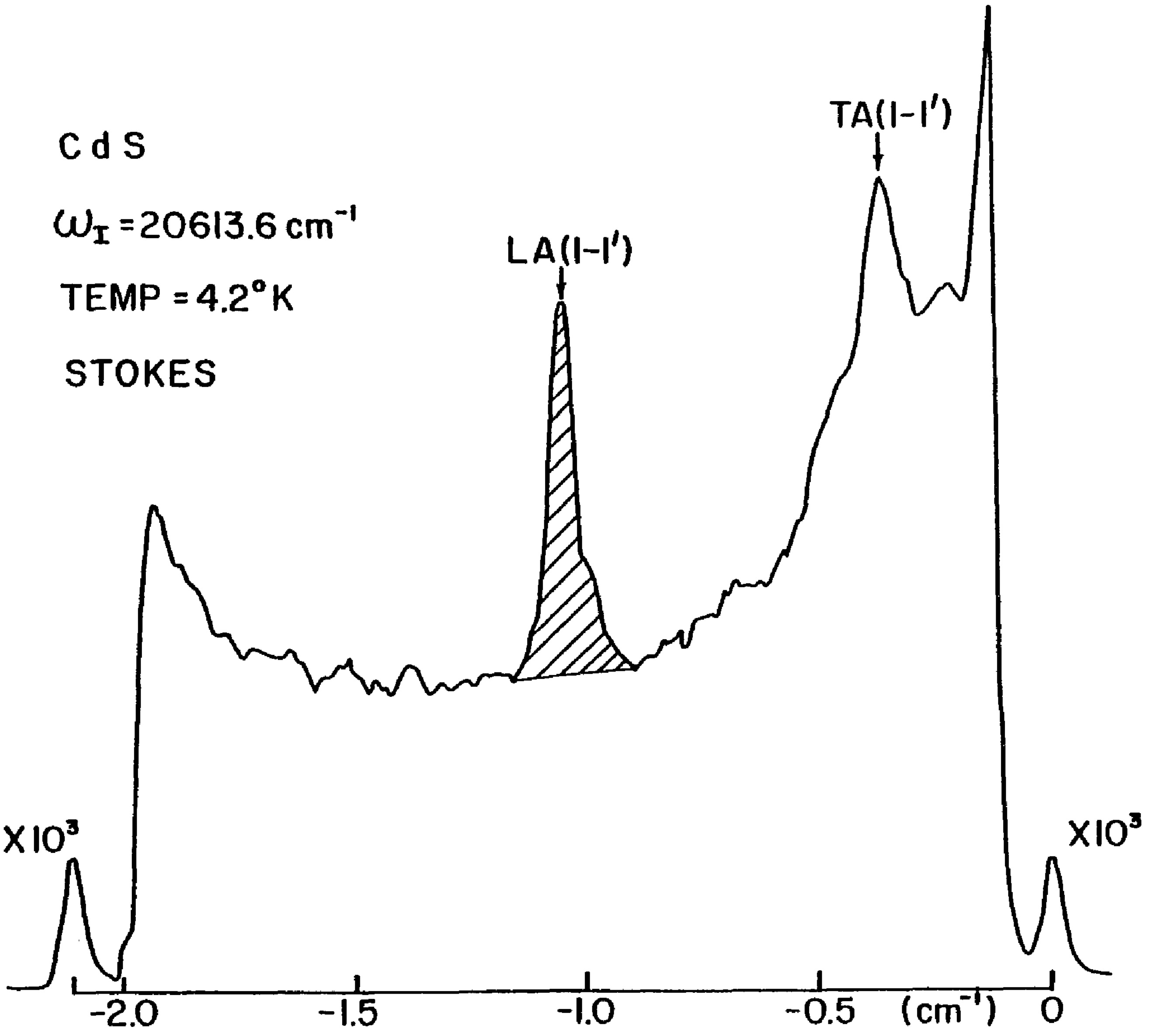
CdS
ω_I = 20613.6 cm⁻¹
TEMP = 4.2° K
STOKES
LA(1-1′)
TA(1-1′)
X10³
X10³
-2.0
-1.5
-1.0
-0.5
(cm⁻¹)
0

FIG. 6-3 Brillouin shifts of observed one phonon Stokes and anti-Stokes peaks as a function of incident laser frequency. Experimental Brillouin shift data was obtained by using three different FSRs of the Fabry-Perot equal to 2.11cm^{-1}, 5.87cm^{-1} and 12.63cm^{-1}. Solid lines represent the best fit of the theoretical Brillouin shift to the data.

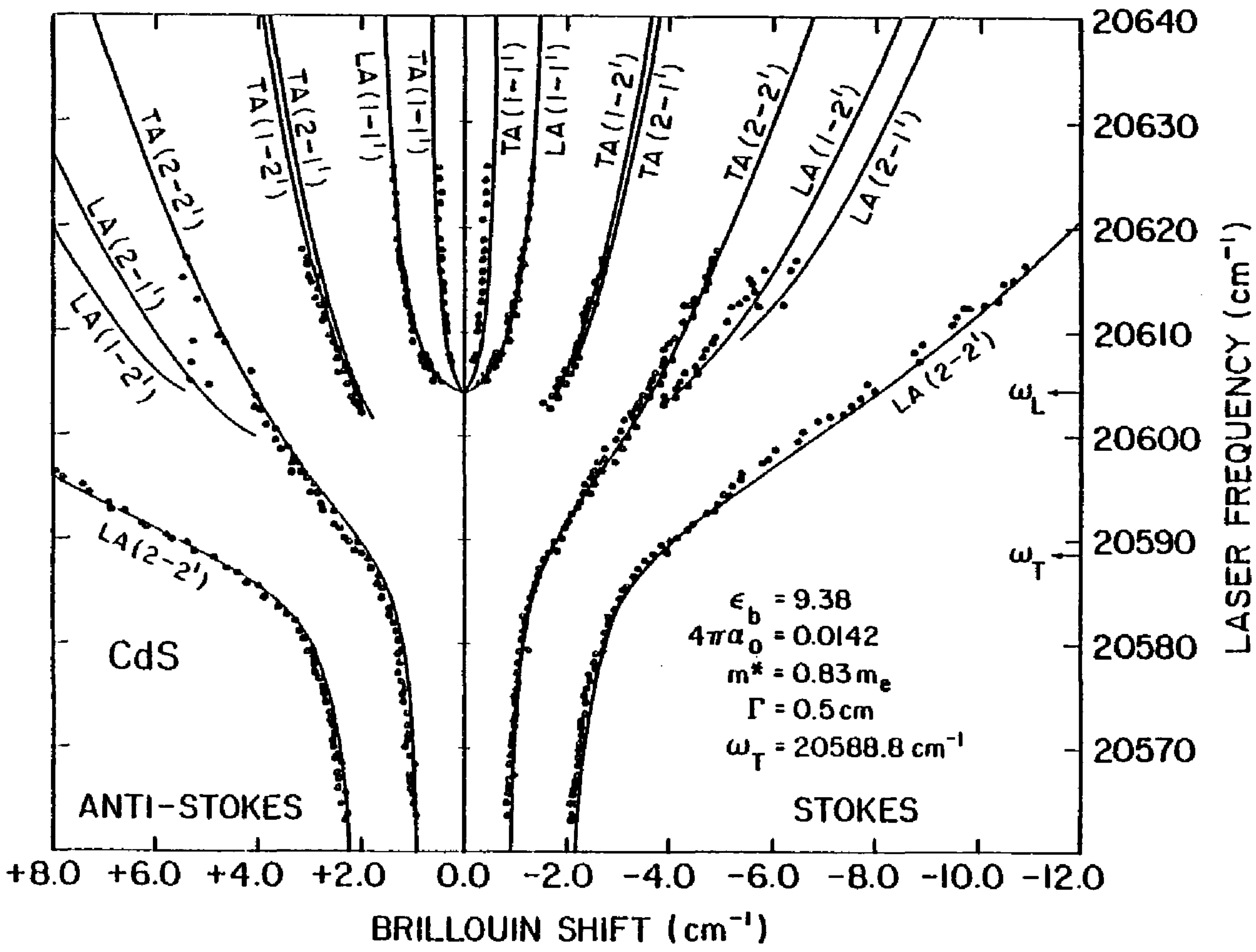
CdS
ANTI-STOKES
STOKES
TA(2-2')
LA(2-1')
LA(1-2')
TA(1-2')
TA(2-1')
LA(1-1')
TA(1-1')
TA(1-1')
LA(1-1')
TA(1-2')
TA(2-1')
TA(2-2')
LA(1-2')
LA(2-1')
LA(2-2')
LA(2-2')
$\epsilon_b = 9.38$
$4\pi\alpha_0 = 0.0142$
$m^* = 0.83\, m_e$
$\Gamma = 0.5$ cm
$\omega_T = 20588.8$ cm^{-1}
ω_L
ω_T
+8.0
+6.0
+4.0
+2.0
0.0
-2.0
-4.0
-6.0
-8.0
-10.0
-12.0
BRILLOUIN SHIFT (cm^{-1})
20640
20630
20620
20610
20600
20590
20580
20570
LASER FREQUENCY (cm^{-1})

Brillouin linewidth. (Some of the data was digitally recorded after which both the Rayleigh and Brillouin components were fitted to Lorentzian lineshapes. An illustration of this is given in Fig. 6-5.) The solid curves in Fig. 6-4 are the theoretical predictions(1) with four different values of Γ:

$$\Delta = 2c_s \left(K''_{I_i} + K''_{s_j}\right) \tag{6.1}$$

where c_s is the sound velocity. K''_{I_i} and K''_{s_j} are the imaginary parts of the incident and scattered polariton wavevectors obtained from the dispersion relation [see Eq. (4.25)] using known values of the exciton parameters determined in Sec. B (Table 6-1). These curves in Fig. 6-4 are computed with Γ taken as a frequency-independent constant. However, $\Gamma(\omega)$ may be an increasing function of ω for $\omega > \omega_T$, as suggested by K. Cho, which would improve the agreement between experiment and theory.

3. External Scattering Cross Sections

The theoretical curves for both the internal [see Eq. (4.38)] and external [see Eq. (4.53)] Stokes scattering cross sections will now be displayed for both the deformation potential and piezoelectric interactions [Eqs. (4.18) and (4.23) respectively]. The values used for these two interactions are listed in Table 6-2. The curves in Fig. 6-6 result from the substitution of Eq. (4.18) into Eqs. (4.38) and (4.53) while using the values listed in Tables 6-1 and 6-2 (Deformation potential). This figure shows the logarithm of the internal scattering cross section (curve a)+, the external scattering

---

+ The internal scattering cross section is the same for all three ABCs in Eq. (4.39).

FIG. 6-4 Approximate experimental linewidths of the Stokes TA (2-2') Brillouin components (FWHM with laser linewidth subtracted) as a function of incident laser frequency. The solid lines are theoretical predictions with four different values of the exciton damping parameter Γ.

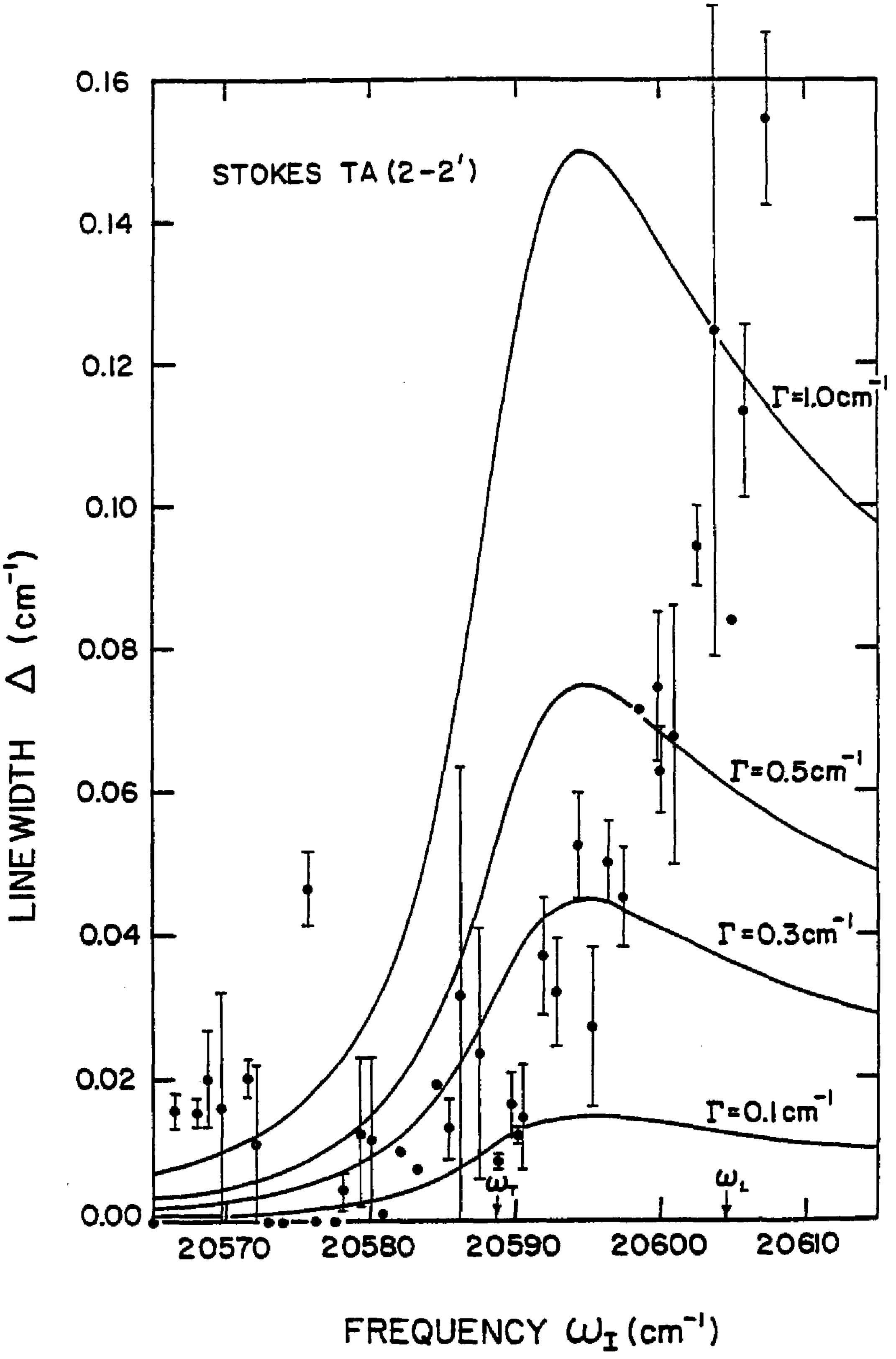

STOKES TA (2-2′)
0.16
0.14
0.12
0.10
0.08
0.06
0.04
0.02
0.00
LINEWIDTH Δ (cm⁻¹)
Γ=1.0cm⁻¹
Γ=0.5cm⁻¹
Γ=0.3cm⁻¹
Γ=0.1cm⁻¹
ω_T
ω_L
20570
20580
20590
20600
20610
FREQUENCY ω_I (cm⁻¹)

FIG. 6-5 Brillouin spectrum showing both Rayleigh and Stokes Brillouin lines fitted to Lorentzians after being digitally recorded. Fabry-Perot FSR equaled 1.75cm^{-1} with laser frequency equal to 20590.2cm^{-1}.

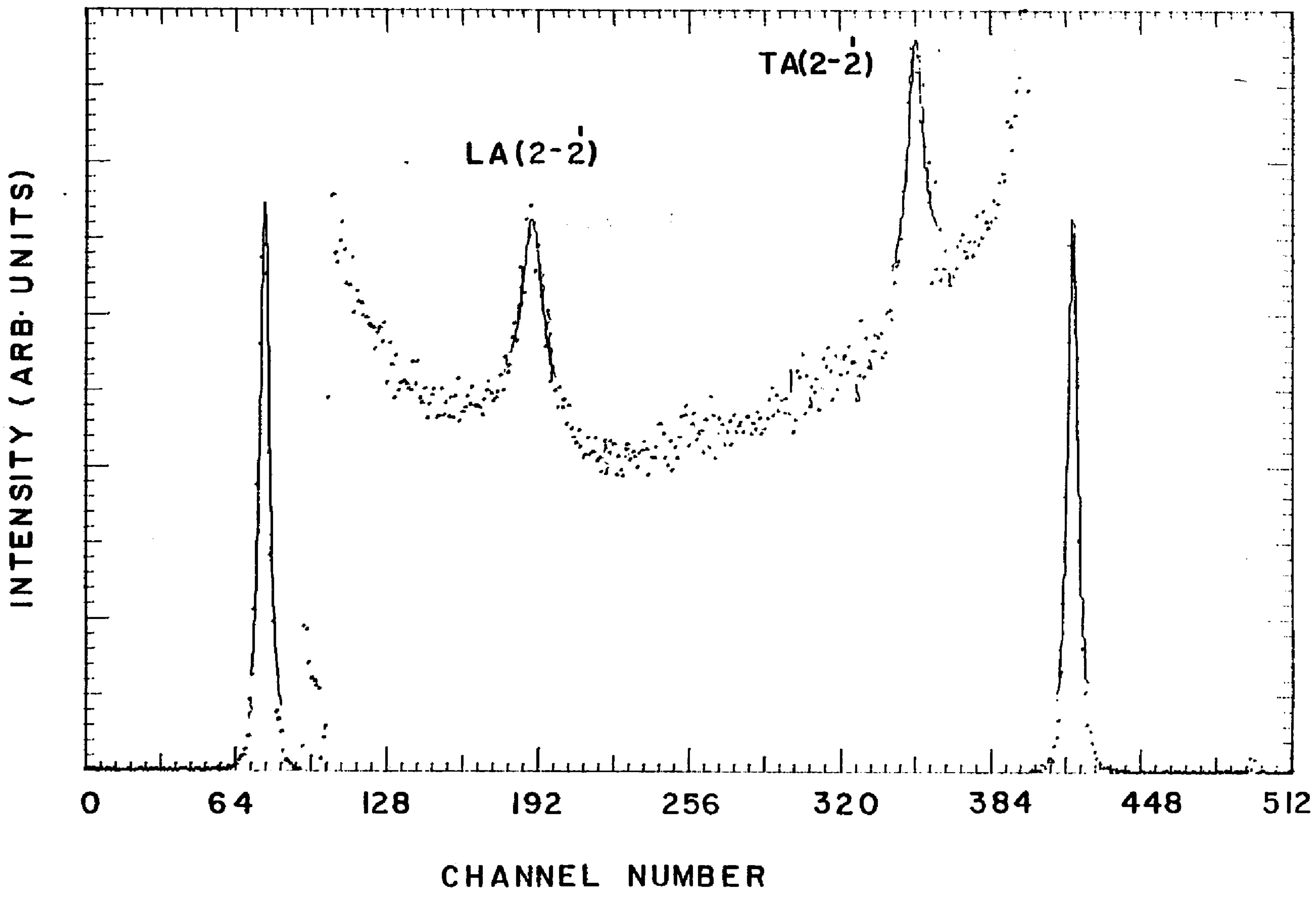
INTENSITY (ARB· UNITS)
LA(2-2̄)
TA(2-2̄)
0
64
128
192
256
320
384
448
512
CHANNEL NUMBER

cross section with the solid angle correction factor (curve b) and the external scattering cross section without the solid angle correction factor (curve c) for ABC 1 [Eq. (4.39)] as a function of incident frequency ω_I for the Stokes LA (2-2') scattering process. One can see how curve b is generated by comparing curve a with Fig. 4-6 which shows the product of the incident and scattered transmissivities for ABC 1. Fig. 6-7 gives a similar illustration for the internal and external scattering cross sections for the Stokes TA (2-2') component utilizing the piezoelectric interaction as discussed in Chap. IV.

In. Fig. 6-8, the logarithm of the intensity measurements on the Stokes LA (2-2') Brillouin components resulting from RBS experiments utilizing two different FSRs of the Fabry-Perot are shown along with the three theoretical external scattering cross sections. The three theoretical curves result from Eq. (4.53) with $\Gamma_o(q)$ given by Eq. (4.18) and $T_i(\omega_I)$ and $T_j'(\omega_S)$ computed via Eqs. (4.48) and (4.50) for the three different ABCs [Eq. (4.39)]. The data in this figure has been normalized in the frequency region where the three theoretical curves are approximately equal ($20560\text{cm}^{-1} \leq \omega_I \leq 20570\text{cm}^{-1}$). The normalization constant for the data obtained using a FSR equal to 12.63cm^{-1} (closed circles) was ~8.2 while the normalization constant for the data obtained with FSR equal to 5.87cm^{-1} (open circles) was ≈8.54. Each data point was determined by measuring the actual Brillouin lineshape from the strip chart record using a planimeter. The equation used to determine the intensity of each Brillouin line is (before taking the logarithm):

$$I = A \left(\frac{FSR}{L}\right) \left(\frac{R}{100}\right) \tag{6.2}$$

Here A is the averaged area (in square inches) of the Brillouin component as measured several times with the planimeter (see Fig. 6-2 for an illustration of the area measured), FSR is the free spectral range of the Fabry-Perot (in cm^{-1}), L is the physical distance (in inches) between the two Rayleigh lines and R is the full scale reading of the ratemeter (in counts/second).

A similar illustration for the intensity of the Stokes TA (2-2') data with the FSR equal to $5.87cm^{-1}$ is given in Fig. 6-9. Each data point here has been normalized by the same normalization constant (~8.54) used for the Stokes LA (2-2') data recorded with FSR equal to $5.87cm^{-1}$ (open circles in Fig. 6-8). The three curves in Fig. 6-9 represent the external scattering cross sections for the three ABCs in the case of the piezoelectric polariton-phonon interaction [Eq. (4.21)].

The logarithm of the intensities of the Stokes LA (1-1') Brillouin lines obtained using two FSRs equal to $2.11cm^{-1}$ and $12.63cm^{-1}$, are shown in Fig. 6-10 along with the three theoretical scattering cross section curves obtained from Eq. (4.53) with $\Gamma_o(q)$ given by (4.18). The open circles are the data with FSR = $2.11cm^{-1}$ which have been normalized to the theoretical curves. The closed circles represent data obtained from two FSRs equal to $2.11cm^{-1}$ and $5.87cm^{-1}$ which have been normalized by the same normalization constant (~8.2) used for the Stokes LA (2-2') with FSR = $12.63cm^{-1}$.

Additional analysis and discussion concerning the external scattering cross section results from RBS is given in Chap. VII.

FIG. 6-6 Log_{10} of the theoretical internal (a), external with solid angle correction factor (b) and external without solid angle correction factor (c) scattering cross sections for LA (2-2') scattering as a function of laser frequency ω_I. ABCl is assumed for curves (b) and (c). Parameters used in the figure are from Tables 6-1 and 6-2.

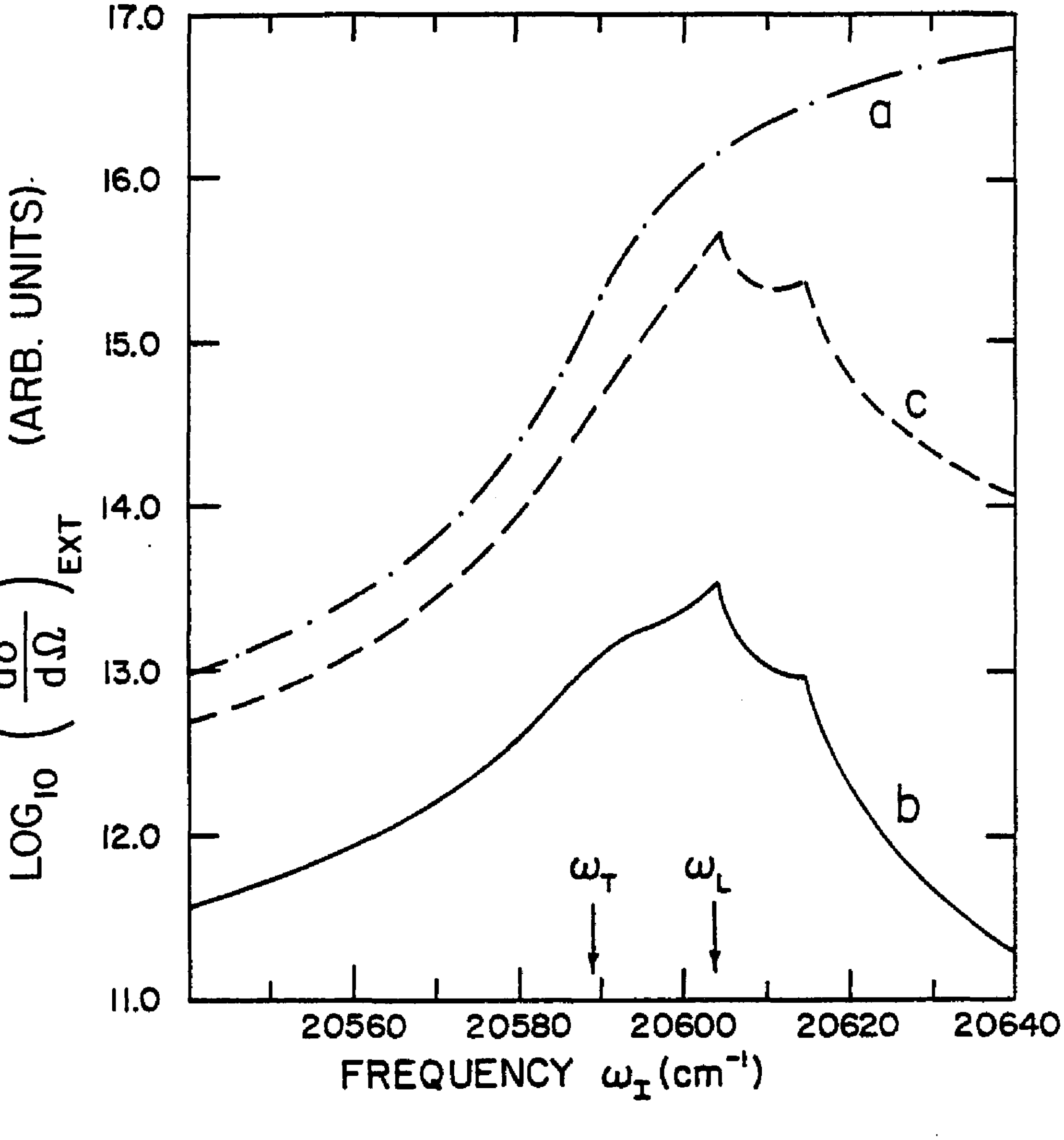
17.0
16.0
15.0
14.0
13.0
12.0
11.0
LOG$_{10}$ $\left(\frac{d\sigma}{d\Omega}\right)^{LA(2\to2')}_{EXT}$ (ARB. UNITS)
a
c
b
ω_T
ω_L
20560
20580
20600
20620
20640
FREQUENCY ω_I (cm^{-1})

FIG. 6-7 Log_{10} of the theoretical internal (a), external with solid angle correction factor (b) and external without solid angle correction factor (c) scattering cross section for TA (2-2') scattering as a function of laser frequency ω_I. ABC1 is assumed for curves (b) and (c). Parameters used in the figure are from Tables 6-1 and 6-2.

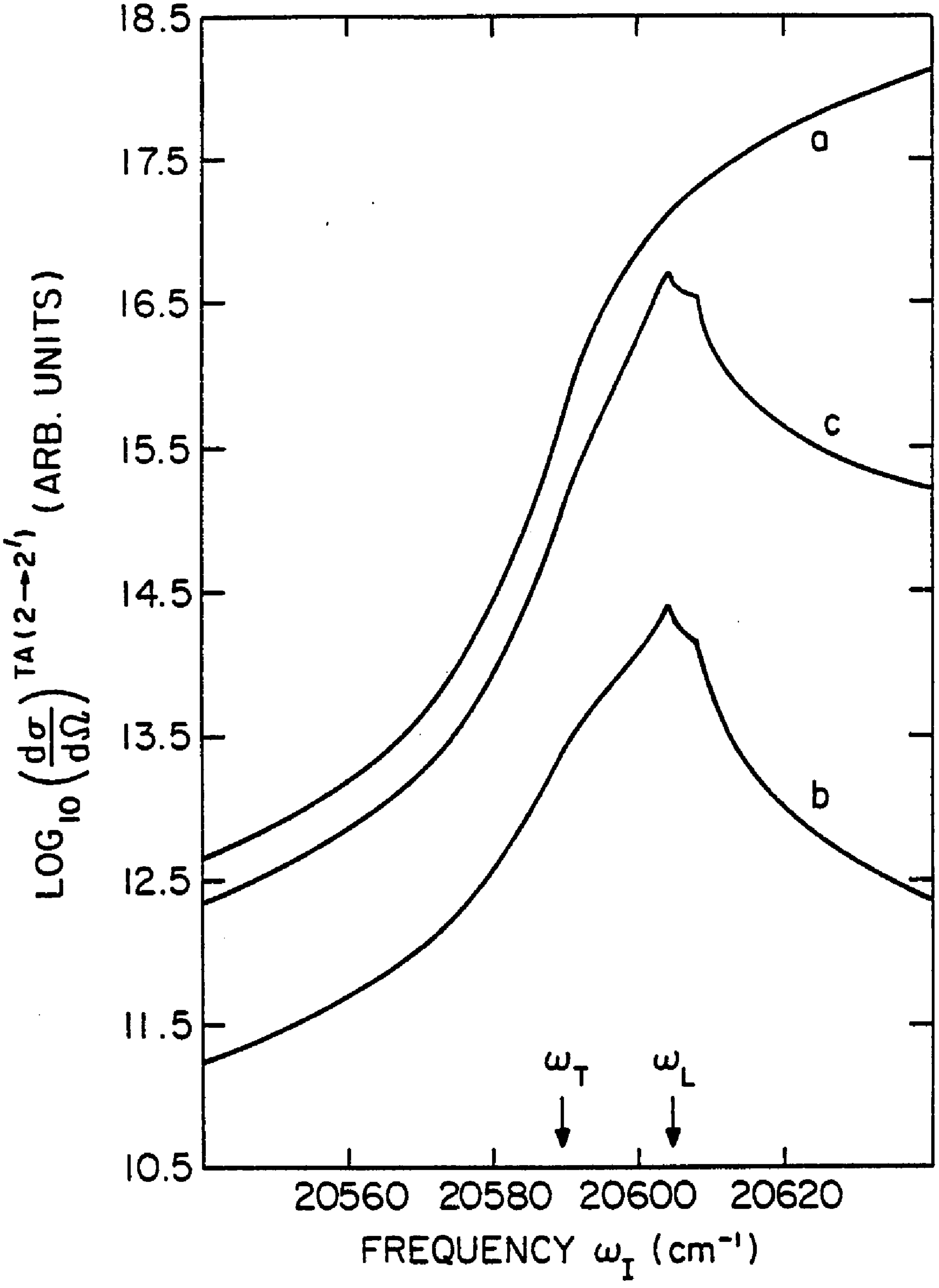
18.5
17.5
16.5
15.5
14.5
13.5
12.5
11.5
10.5
$\mathrm{LOG}_{10}\left(\frac{d\sigma}{d\Omega}\right)^{\mathrm{TA}(2\to 2')}$ (ARB. UNITS)
a
c
b
ω_T
ω_L
20560
20580
20600
20620
FREQUENCY ω_I (cm^{-1})

FIG. 6-8 Log_{10} comparison of the theoretical external scattering cross section for the Stokes LA (2-2') scattering for various ABCs with the $\log_{10}$ of the experimentally measured Brillouin intensity. Open (closed) circles represent the data which has been obtained with a FSR equal to $5.87\mathrm{cm}^{-1}$ ($12.63\mathrm{cm}^{-1}$). Both sets of data have been normalized to the curves in the frequency region $20560\mathrm{cm}^{-1} \leq \omega_I \leq 20570\mathrm{cm}^{-1}$.

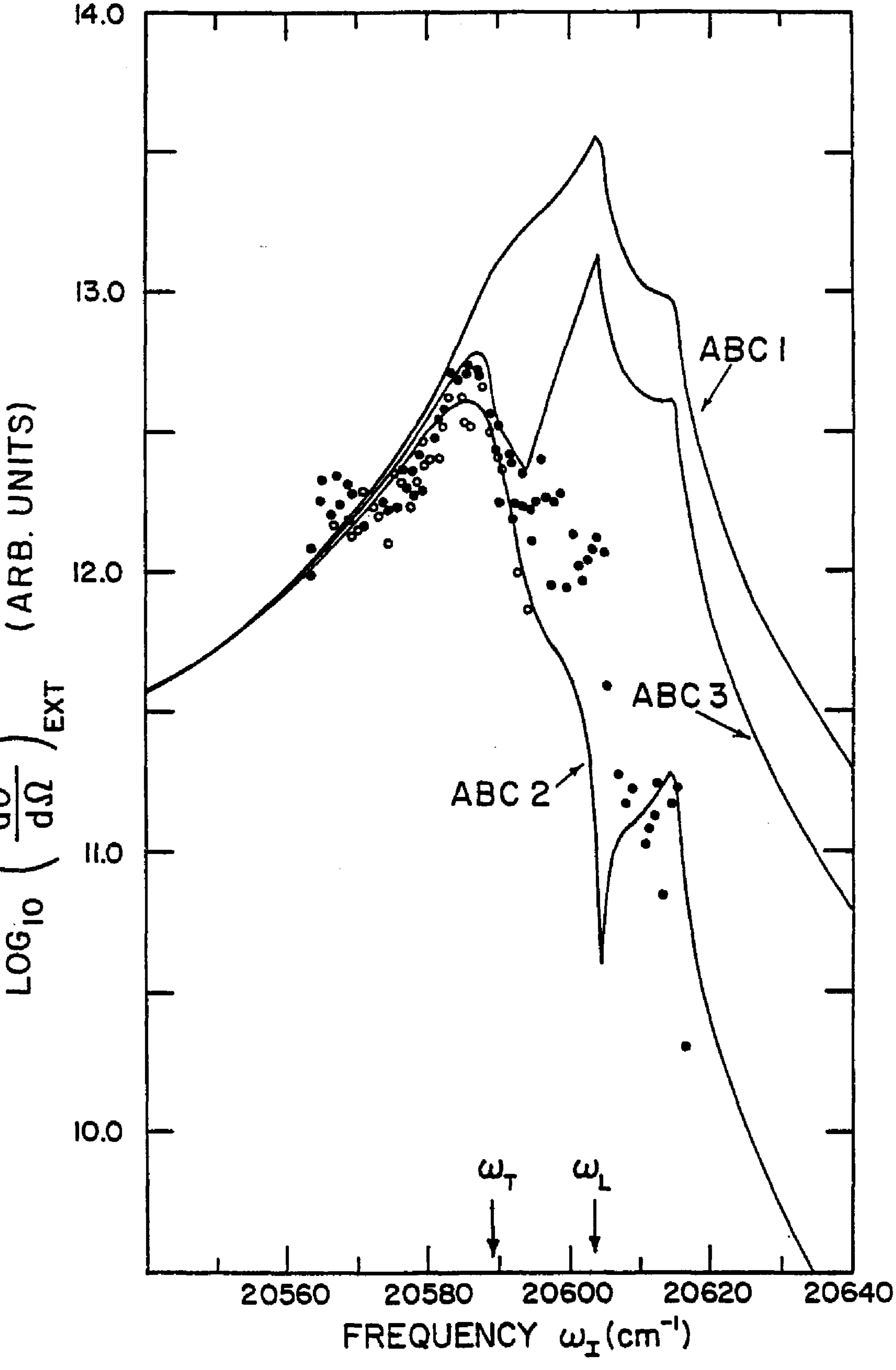
14.0
13.0
12.0
11.0
10.0
$\mathrm{LOG}_{10}\left(\frac{d\sigma}{d\Omega}\right)^{LA(2\to2')}_{EXT}$ (ARB. UNITS)
ABC 1
ABC 3
ABC 2
ω_T
ω_L
20560
20580
20600
20620
20640
FREQUENCY ω_I (cm^{-1})

FIG. 6-9 Log_{10} comparison of the theoretical external scattering cross section for the Stokes TA (2-2') scattering for various ABCs with the $\log_{10}$ of the experimentally measured Brillouin intensity. The closed circles represent the data which has been obtained via a FSR equal to $5.87\mathrm{cm}^{-1}$. This data has been normalized by the same constant used for the open circle data in Fig. 6-8.

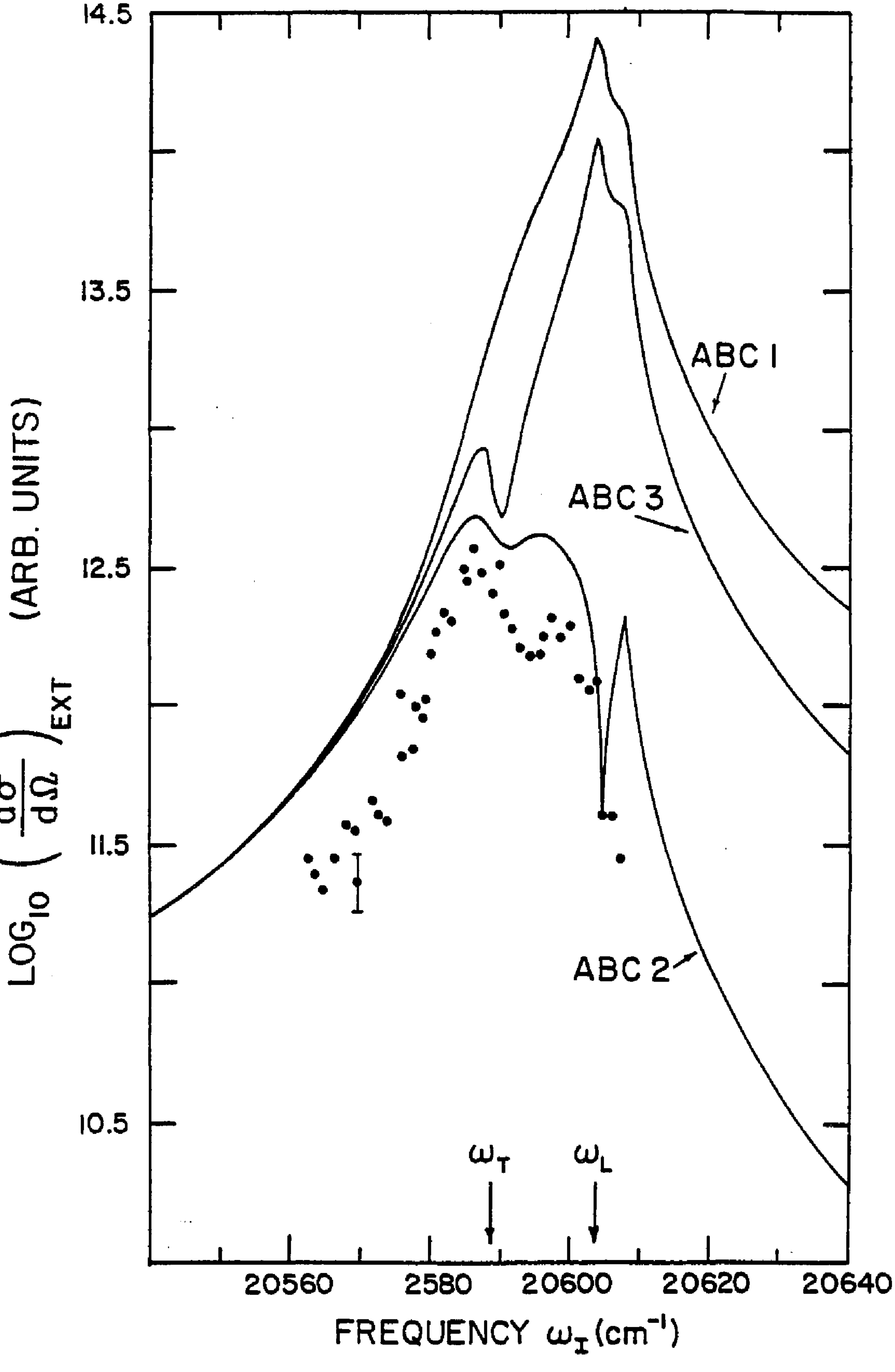

14.5
13.5
12.5
11.5
10.5
ABC 1
ABC 3
ABC 2
ω_T
ω_L
20560
2580
20600
20620
20640
FREQUENCY ω_I (cm^{-1})
$\mathrm{LOG}_{10}\left(\frac{d\sigma}{d\Omega}\right)^{TA(2\to2')}_{EXT}$ (ARB. UNITS)

FIG. 6-10 $\log_{10}$ comparison of the theoretical external scattering cross section for the Stokes LA (1-1') scattering for various ABCs with the $\log_{10}$ of the experimentally measured Brillouin intensity. Open circles plotted along the theoretical curves represent data which has been normalized to the theory (FSR = 2.11 cm^{-1}). Closed circles represent data which has been normalized by the same constant used for the Stokes LA (2-2') data with FSR = 12.63 cm^{-1}. The open triangles represent data obtained with FSR = 2.11cm^{-1} which have now been normalized to the closed circle data.

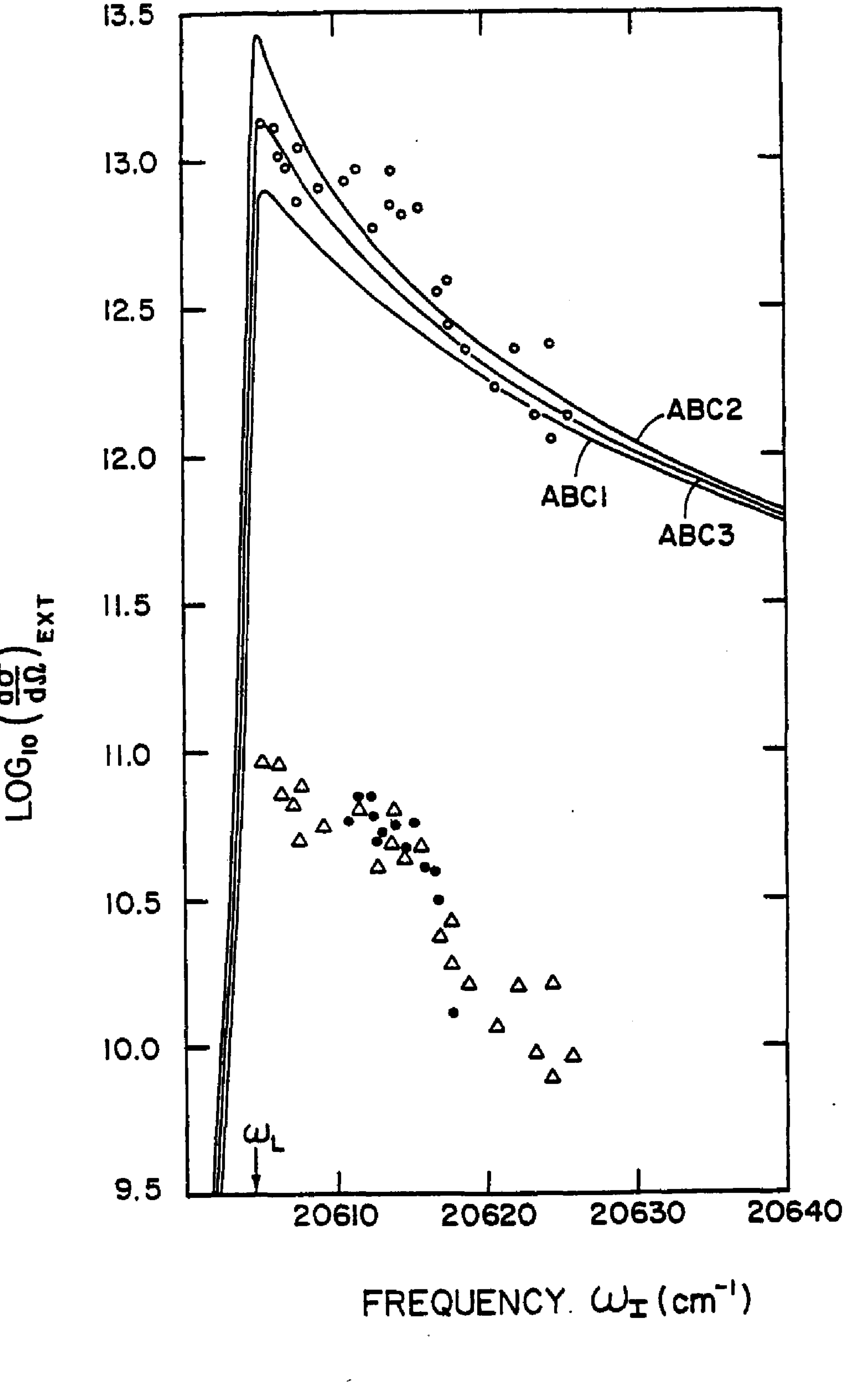
13.5
13.0
12.5
12.0
11.5
11.0
10.5
10.0
9.5
$\mathrm{LOG}_{10}\left(\frac{d\sigma}{d\Omega}\right)^{LA(1-1')}_{EXT}$
ABC2
ABC1
ABC3
ω_L
20610
20620
20630
20640
FREQUENCY ω_I (cm^{-1})

C. REFLECTIVITY RESULTS

As was discussed in Sec. C of Chap. V, the reflectivity experiments covered a frequency region which included both the n=1 A and B exciton resonances in CdS. The ratio of the digital record of the CdS reflectivity spectrum obtained from the sample to that of the lamp spectrum obtained from a mirror resulted in a corrected experimental reflectivity expression as a function of channel number:

$$J(I) = \frac{\tilde{C}(N(I)-\bar{N}_B)\ \{1+(N(I)-\bar{N}_B)\ R_c\}}{(\langle M(I)\rangle - \bar{M}_B)\ \{1+(\langle M(I)\rangle - \bar{M}_B)\ R_c\}} \tag{6.3}$$

where I is the channel number ranging from 1 to 500 (corresponding to a frequency range from 20816.2cm^{-1} to 20478.7cm^{-1}). The constant $\tilde{C}$ normalizes the expression in (6.3) to approximately 25% in the frequency region between 20492.2cm^{-1} to 20485.5cm^{-1}.(9) N(I) corresponds to the CdS reflectivity digital reading in counts per channel while M(I) similarly corresponds to the reflectivity reading of the lamp spectrum off the mirror. The term <M(I)> is a linearized version of M(I) which was created to smooth out the correct reflectivity expression J(I). $\bar{N}_B(\bar{M}_B)$ is an averaged background for the CdS (mirror) reflectivity which was established in the frequency region from 20807.2cm^{-1} to 20792.2cm^{-1}. The R_c term which equals 1.76 X 10^{-6} is a factor used to correct for the non-linear response of the photon counting electronics.

The theoretical reflectivity expression will now be formulated. Since both the A and B exciton resonances were observed in the experimental runs, the theoretical formulation must include both contributions. This can be accomplished most easily by describing the A-exciton dispersion equation by Eq. (4.25) while the B-exciton is included as a classical oscillator [Eq. (4.25) with m^* set equal to infinity]. These two contributions can be included in Eq. (4.25) by allowing the background dielectric constant to become a classical oscillator function of ω:

$$\varepsilon_b \longrightarrow \varepsilon_b(\omega) = \bar{\varepsilon}_b + \frac{4\pi\alpha_B\omega_{\circ B}^2}{\omega_{\circ_B}^2 - \omega^2 - i\omega\Gamma_B} \qquad (6.4)$$

Here $\bar{\varepsilon}_b$ is the background dielectric constant which excludes a contribution from the B-exciton, $4\pi\alpha_{\circ_B}$ is proportional to the B-exciton's oscillator strength, $\omega_{\circ_B}$ is the B-exciton's transverse frequency and Γ_B is its damping constant. Since the main concern in this analysis is to fit the reflectivity curve of the A-exciton, the values of $4\pi\alpha_{\circ_B}$, $\omega_{\circ_B}$ and Γ_B, which are displayed in Table 6-3, were obtained on a trial and error basis (no fitting between the theoretical classical oscillator model and the experimental B-exciton reflectivity was performed).

Substitution of Eq. (6.4) into Eq. (4.25) results in the polariton dispersion equation (in cm^{-1}):

$$\frac{k^2}{\omega^2} = \varepsilon_b(\omega) + \frac{4\pi\alpha_\circ\omega_\circ^2}{\omega_\circ^2 + Bk^2 - \omega^2 - i\omega\Gamma} \qquad (6.5)$$

which results, once again, in two simultaneous propagating polariton modes, $\bar{k}_i$. The complex refractive index for each of these modes is obtained through the relation

$$\bar{n}_{c_i} = \frac{\bar{k}_i(\omega)}{\omega} \qquad i = 1,2 \qquad (6.6)$$

The theoretical expression for the reflectivity, given by Eq. (4.49) now becomes:

$$\bar{R} = \left| \frac{\bar{a}_2\left(1-\bar{n}_{c_1}\right) - \bar{a}_1\left(1-\bar{n}_{c_2}\right)}{\bar{a}_2\left(1+\bar{n}_{c_1}\right) - \bar{a}_1\left(1+\bar{n}_{c_2}\right)} \right|^2 \qquad (6.7)$$

where the three ABC expressions in Eq. (4.39) are now expressed as:

$$\bar{a}_i = \bar{n}_{c_i}^2 - \varepsilon_b(\omega) \qquad \text{ABC1} \qquad (6.8a)$$

$$\bar{a}_i = \bar{n}_{c_i}(\bar{n}_{c_i}^2 - \varepsilon_b(\omega)) \qquad \text{ABC2} \qquad (6.8b)$$

$$\bar{a}_i = \frac{1}{\bar{n}_{c_i} - n_e} \qquad \text{ABC3} \qquad (6.8c)$$

$$i = 1,2$$

The theoretical reflectivity expression given by Eq. (6.7) above was then fitted to the corrected experimental reflectivity expression Eq. (6.3) for each of the three ABCs [Eq. (6.8a) - (6.8c)] via a non-linear least square fitting program. During this analysis, the A and B exciton parameters displayed in Tables 6-1 and 6-3 were held fixed while the A-exciton damping constant Γ and the background dielectric constant $\bar{\varepsilon}_b$ were allowed to vary. Fitting occurred over the frequency region from 20654.2cm^{-1} to 20482.1cm^{-1} which included the A-exciton resonance only. Figs. 6-11, 6-12 and 6-13 illustrate the best fits between the theoretical and experimental reflectivity expressions for ABC1, 2 and 3 respectively, while Table 6-4 shows the best fit values of Γ and $\bar{\varepsilon}_b$ for each of the ABCs. Further discussion on these results will be continued in Chap. VII.

D. ABSORPTION MEASUREMENTS

In a separate attempt to determine the value of the exciton damping constant Γ, absorption measurements were performed on the same CdS sample used in the RBS and reflectivity experiments previously

FIG. 6-11 Non-linear least squares fit of the theoretical reflectivity expression using ABCl to the experimental reflectivity. Best fit coefficients are listed in Table 6-4. The theoretical curves are the solid lines while the experimental expression is illustrated by the data points. The arrows indicate the frequency region in which fitting was taking place. Reflectivity percentage is shown along the y-axis.

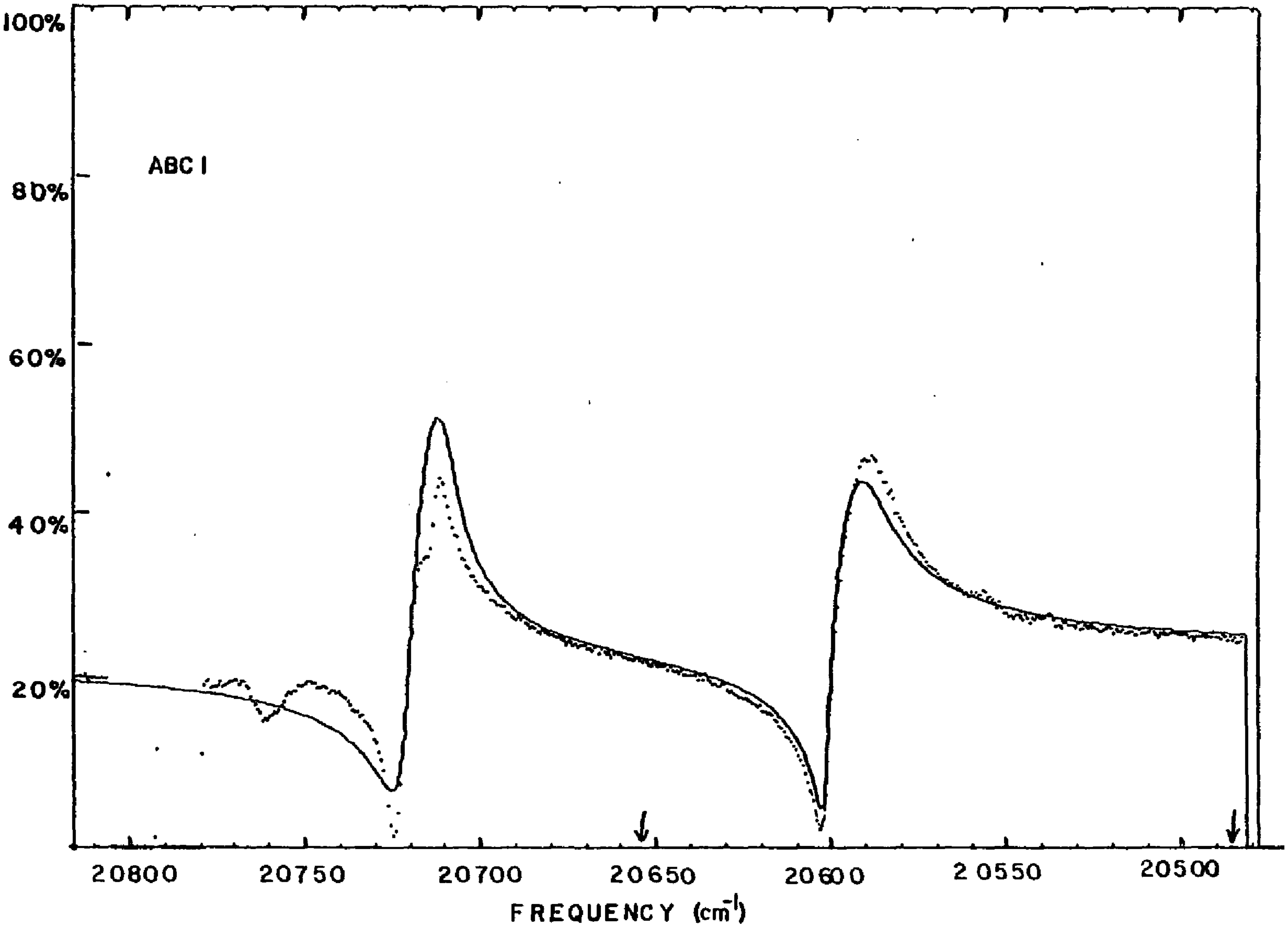
ABC I
100%
80%
60%
40%
20%
20800
20750
20700
20650
20600
20550
20500
FREQUENCY (cm^{-1})

FIG. 6-12 Non-linear least squares fit of the theoretical reflectivity expression using ABC2 to the experimental reflectivity. Best fit coefficients are listed in Table 6-4. The theoretical curves are the solid lines while the experimental expression is illustrated by the data points. The arrows indicate the frequency region in which fitting was taking place. Reflectivity percentage is shown along the y-axis.

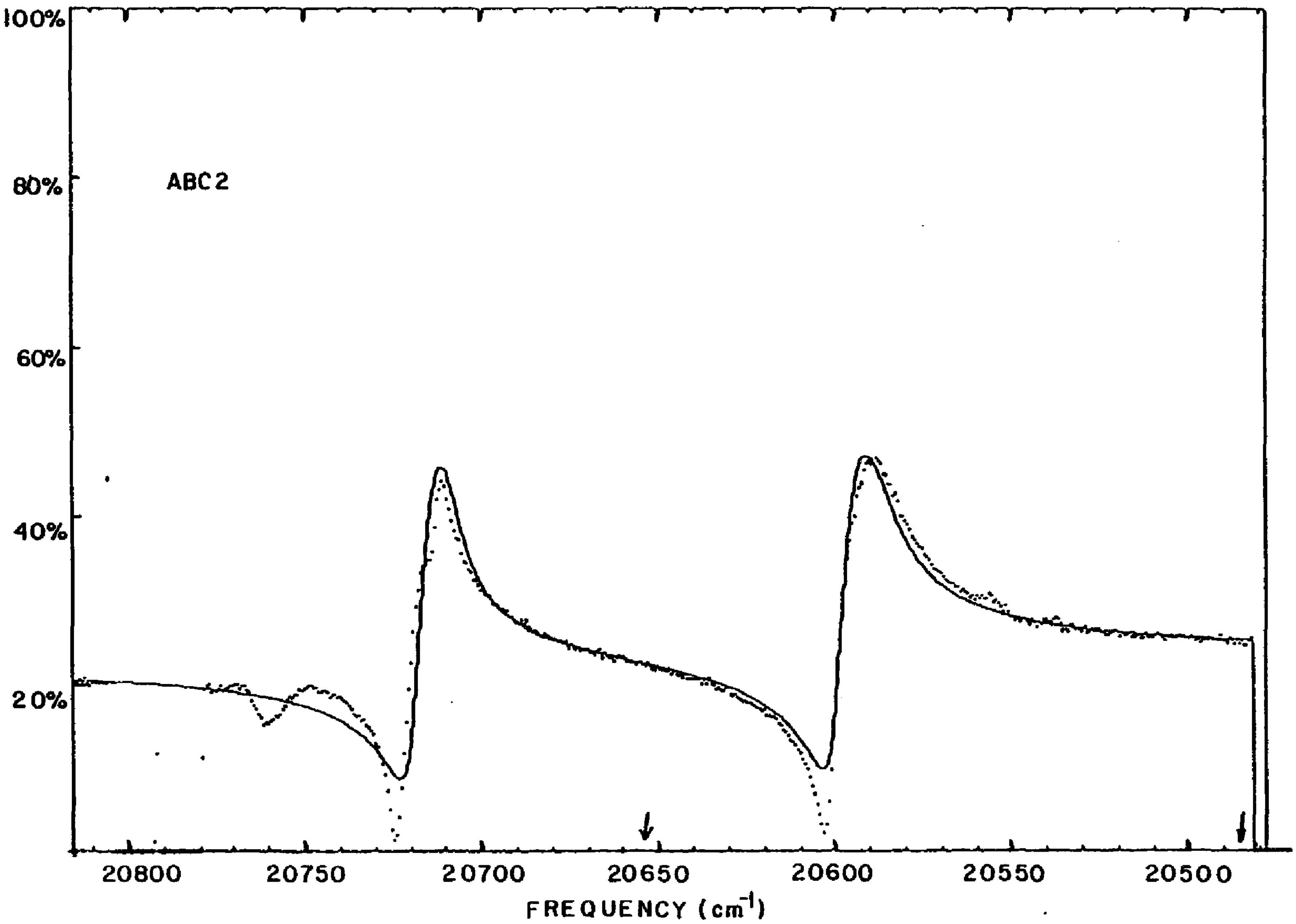
ABC2
100%
80%
60%
40%
20%
20800
20750
20700
20650
20600
20550
20500
FREQUENCY (cm^{-1})

FIG. 6-13 Non-linear least squares fit of the theoretical reflectivity expression using ABC3 to the experimental reflectivity. Best fit coefficients are listed in Table 6-4. The theoretical curves are the solid lines while the experimental expression is illustrated by the data points. The arrows indicate the frequency region in which fitting was taking place. Reflectivity percentage is shown along the y-axis.

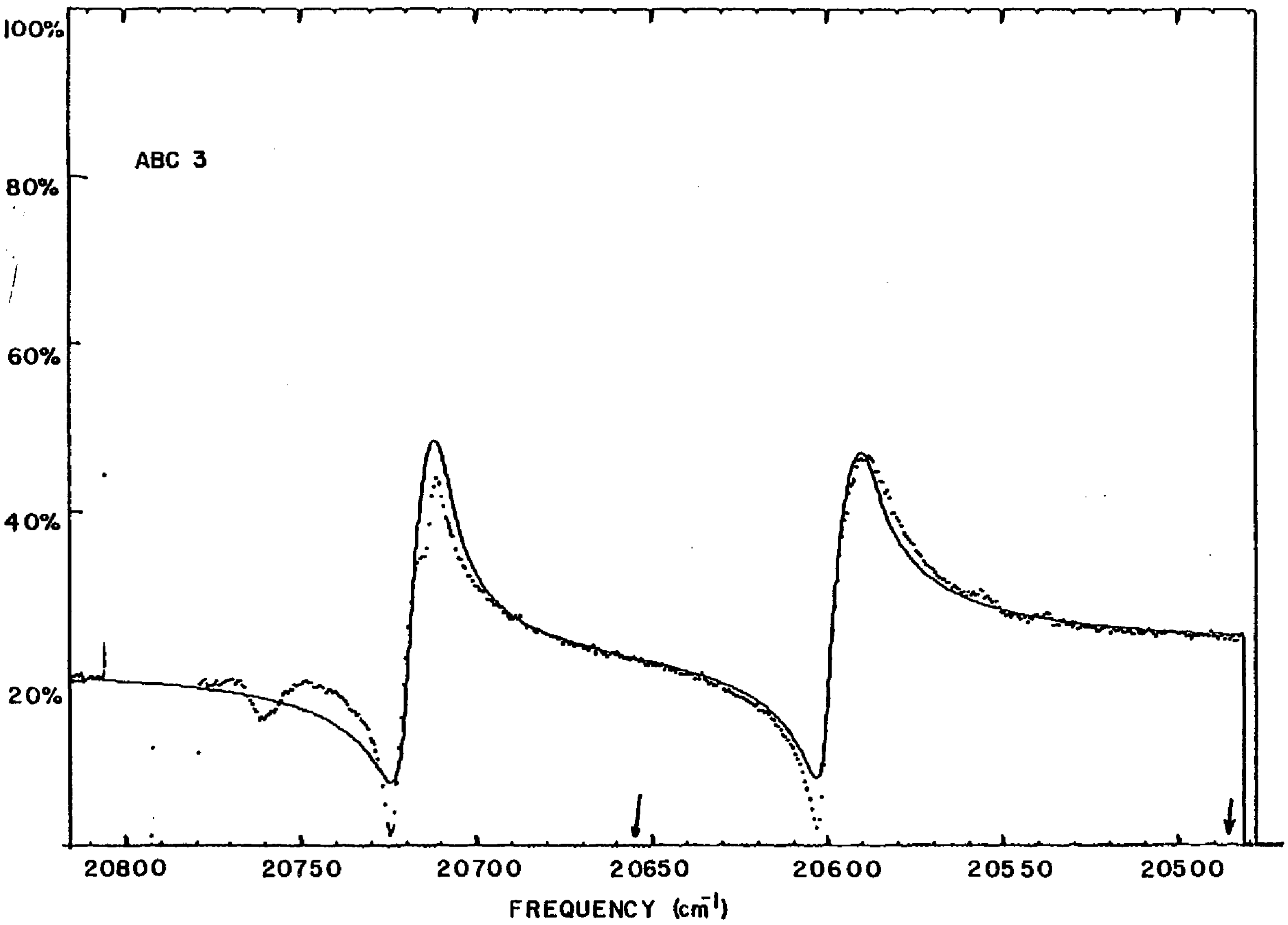
ABC 3
100%
80%
60%
40%
20%
20800
20750
20700
20650
20600
20550
20500
FREQUENCY (cm^{-1})

discussed in Sections B and C. The absorption measurements were performed at 4.2°K over the frequency region $20540 \leq \omega_I \leq 20670\text{cm}^{-1}$ $(\vec{k}_I \perp \hat{c}, \vec{E}_I \perp \hat{c})$. The experiment utilized the dye laser to change the incident frequency over this region. The intensity of the transmitted light through the crystal, in addition to the intensity of a reference beam used to correct for equipment variations at different laser frequencies, was measured by scanning the grating spectrometer over the incident laser frequency. It was noticed, however, that small depolarization effects from the polarization rotator and the fused quartz dewar windows resulted in the incident polarization having a small component parallel to $\hat{c}$ and thus yielding a larger transmission through the sample. In an attempt to partially remedy this problem, a small polarizer was placed inside the helium dewar to insure a maximum incident polarization perpendicular to the c-axis.

The theoretical calculation of the optical density is performed with the use of Eqs. (4.47), (4.48) and (4.50). The ratio of the transmitted light through the crystal to the incident laser light is given by:

$$\frac{I_T^{ext}}{I_I^{ext}} = \sum_{i=1}^{2} T_i(\omega_I)\, e^{-2K_{I_i}''L}\, T_i'(\omega_I) \qquad (6.9)$$

where $T_i(\omega_I)$ is given by Eqs. (4.47) and (4.48) (for $i = 1$ and 2 respectively) and $T_i'(\omega_I)$ is given by Eq. (4.50). K_{I_i}'' is the imaginary part of the i^{th} polariton wavevector and L is the sample thickness. (Interference effects between the two propagating modes in addition to multiple reflections from the sample surfaces have been neglected in the calculation of (6.9)). The optical density is:

$$\text{O.D.} = \log_{10} \left(\frac{I_T^{ext}}{I_I^{ext}} \right) \tag{6.10}$$

The curves resulting from the substitution of Eq. (6.9) into Eq. (6.10) using ABC1 [Eq. (4.39)] are shown in Fig. 6-14 for six different values of Γ. Plotted also are the experimentally measured optical densities for several different incident laser frequencies. The Γ-value of ~0.05cm^{-1} in the frequency region between 20560 and 20580cm^{-1} seems to be the most appropriate one. One can then state that this value of Γ should be considered as a lower bound since more light is probably being transmitted through the crystal due to the depolarization effects mentioned earlier.

FIG. 6-14 Comparison between theoretical and experimental optical density expressions. The theoretical optical density expression utilizes transmissivity expressions from Chap. IV using ABC1. Six values of Γ have been chosen.

(a) $\Gamma = 0.01\ \text{cm}^{-1}$, (b) $\Gamma = 0.02\ \text{cm}^{-1}$

(c) $\Gamma = 0.05\ \text{cm}^{-1}$, (d) $\Gamma = 0.1\ \text{cm}^{-1}$

(e) $\Gamma = 0.2\ \text{cm}^{-1}$, (f) $\Gamma = 0.5\ \text{cm}^{-1}$

Other parameters used are from Table 6-1.

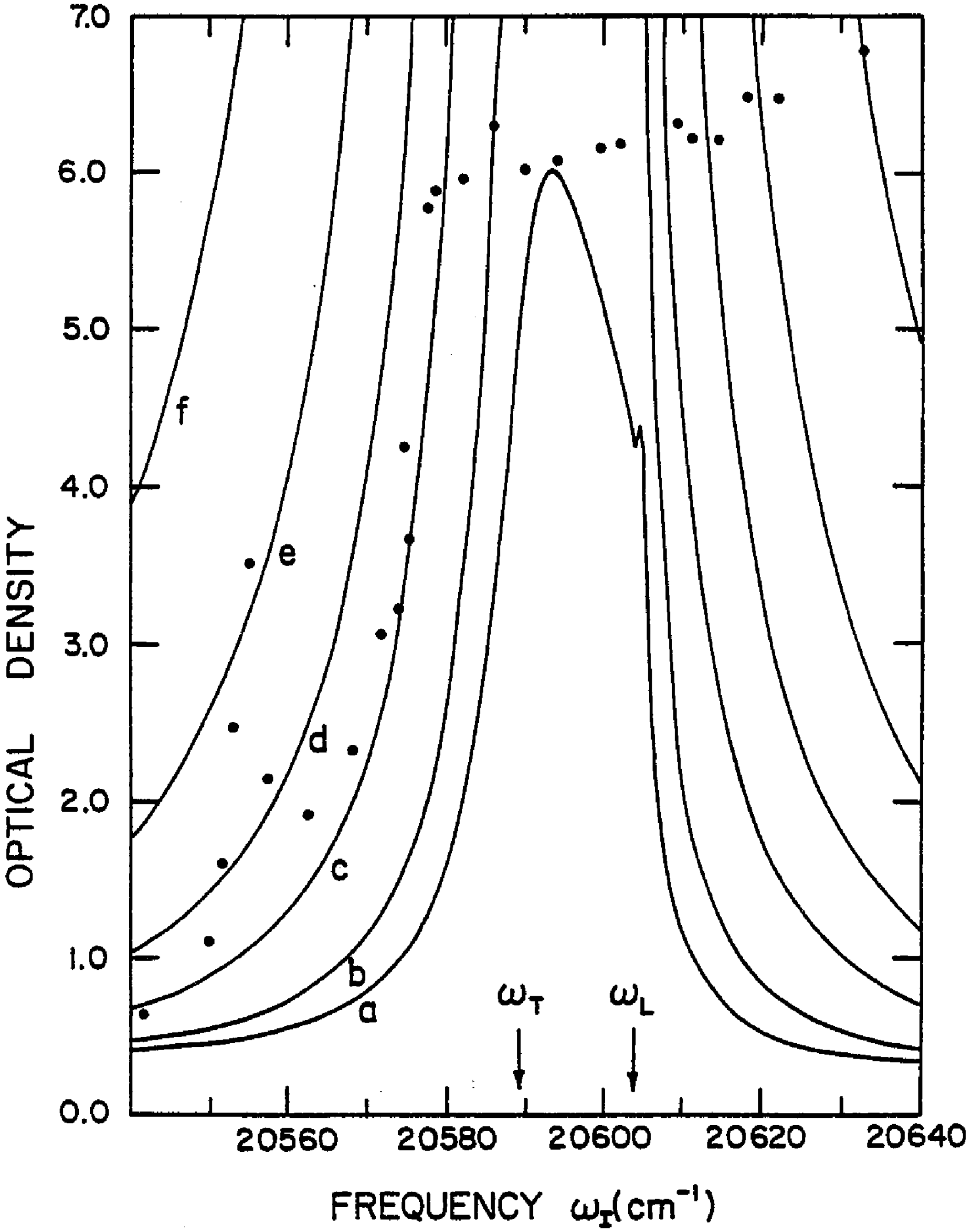
7.0
6.0
5.0
4.0
3.0
2.0
1.0
0.0
OPTICAL DENSITY
20560
20580
20600
20620
20640
FREQUENCY ω_I(cm^{-1})
f
e
d
c
b
a
ω_T
ω_L

TABLE 6-1 BEST FIT VALUES OF THE EXCITON PARAMETERS FOR THE n = 1 A-EXCITON IN CdS

	Current Values	Winterling and Koteles (60)
Dielectric Constant ϵ_b	9.38	9.3
Effective Mass m^*	$0.83m_e$	$0.89m_e$
Oscillator Strength $4\pi\alpha_o$	0.0142	0.0139
Transverse Frequency ω_T	20588.8cm^{-1}	20589.5cm^{-1}

TABLE 6-2 VALUES USED IN THE EXPRESSIONS FOR THE DEFORMATION POTENTIAL AND PIEZOELECTRIC INTERACTIONS

Sound Velocities(80)

$C_{s_{LA}} = 4.25 \times 10^5$ cm/sec

$C_{s_{TA}} = 1.76 \times 10^5$ cm/sec

Crystal Density(80)

$\rho = 4.84$ gm/cm^3

Piezoelectric Constant(59)

$e_{15} = -0.21$ coul/m^2

Deformation Potentials(81)

$D_e = 4.5$ eV

$D_h = -2.9$ eV

A-Exciton Bohr Radius(53)

$a_B = 28$Å

Effective Hole Mass (60)

$m_h^* = 0.7\ m_e$

Effective Electron Mass(51)

$m_e^* = 0.2\ m_e$

TABLE 6-3 VALUES USED FOR THE CLASSICAL OSCILLATOR DESCRIPTION OF THE B-EXCITON

Oscillator Strength	
$4\pi\alpha_{o_B}$	0.01
Transverse Frequency	
ω_{o_B}	20710.0 cm^{-1}
Damping Constant	
Γ_B	7.0 cm^{-1}

TABLE 6-4 BEST FIT VALUES FOR Γ AND $\bar{\varepsilon}_b$ RESULTING FROM REFLECTIVITY ANALYSIS FOR EACH OF THE THREE ABCs

	ABC1	ABC2	ABC3
Γ	2.09 cm^{-1}	6.97 cm^{-1}	5.04 cm^{-1}
$\bar{\varepsilon}_b$	9.54	11.02	10.17

CHAPTER VII

DISCUSSION

A. INTRODUCTION

Discussions concerning the RBS and reflectivity results will be presented in this chapter. Some additional comparisons between the experimental reflectivity expression and a slightly revised theoretical reflectivity expression will also be made. Some general remarks will be made concerning the theoretical calculation of Chap. IV and the experiment of Chap. V. A summary of the conclusions is then given along with suggestions for future calculations and experiments.

B. DISCUSSION OF THE RBS RESULTS

The non-linear least squares fitting of the theory (Chap. VI. Sec. B) to the Brillouin shift measurements resulted in revised values of the CdS A-exciton parameters: $4\pi\alpha_o$, m^*, ε_b, ω_T (see Table 6-1). These values were then incorporated into the theoretical linewidth expression given by Eq. (6.1) for comparison with the measured full width at half maximum of the Stokes TA (2-2') components. These comparisons showed that for $\omega < \omega_T$ a value of Γ between 0.3 cm^{-1} and 0.5 cm^{-1} might be appropriate.† However, in the frequency region between ω_T and ω_L, the observed FWHM of the TA lines increases monotonically. A similar trend was also observed for the Stokes LA (2-2') components. K. Cho(82) has suggested that for branch 2 polaritons near resonance $(\omega_T \leq \omega \leq \omega_L)$, new decay channels should come into effect due to the

---

† Flynn and Geschwind(83) have also conducted linewidth measurements on CdS. They observed from their samples much narrower linewidths for both TA and LA Brillouin components.

increase in momentum. This would then result in an increase of Γ with increasing frequency, in qualitative agreement with our FWHM data.

The theoretical external differential scattering cross section analysis utilized the values of the exciton parameters obtained from the Brillouin shift analysis. The value of Γ was taken to be 0.5 cm^{-1} as discussed above. The comparisons seen in Figs. 6-8 and 6-9 indicate that ABC2 most closely reflects the behavior of the Brillouin intensity data for the Stokes LA (2-2') and TA (2-2') components. No attempt was made to further fit the three theoretical curves in Figs. 6-8 and 6-9.

The implication of Fig. 6-10 is that the general trend of the Stokes LA (1-1') Brillouin intensity versus incident frequency follows the theoretical predictions with <u>any</u> of the three ABCs. However, when normalized against the Stokes LA (2-2') intensities of Fig. 6-8 (closed circles) one sees that the intensity ratio I(1-1')/I(2-2') is about 100 times smaller than predicted. Since both processes are mediated by deformation potential scattering, their relative strengths are governed by differences in transmissivity, exciton strength functions, energy and group velocities, and the real and imaginary parts of the polariton wavevectors. The group (or energy) velocity is particularly significant because the inner branch polaritons participating in (1-1') scattering have very small velocities leading to a large predicted cross section since $v_{E_i}(\omega_I)$ and $v_{G_j}(\omega_S)$ both occur in the denominator of Eq. (4.53).

C. DISCUSSION ON THE REFLECTIVITY RESULTS

The reflectivity fits between theory (Eq. 6.7) and experiment (Eq. 6.3) in Chap. VI were not very good for the RBS values listed in Table 6-1. All fits resulted in large values for both the background dielectric constant $\bar{\varepsilon}_b$ and the exciton damping constant Γ. In an attempt to improve the fits of the reflectivity, a dead layer (see Chap. I, Sec. C) was incorporated into the analysis.† Once again, the A and B exciton parameters of Tables 6-1 and 6-3 were held fixed while four parameters; Γ, $\bar{\varepsilon}_b$, ℓ, n were varied. Here ℓ is the thickness of the dead layer which is described by a real index of refraction n. Utilization is now made of the reflectivity expression derived by Hopfield and Thomas(9):

$$R = \frac{|1-n_s|^2}{|1+n_s|^2} \qquad (7.1)$$

where

$$n_s = n \left[\frac{(n_A+n)e^{-2ik\ell}-n+n_A}{(n_A+n)e^{-2ik\ell}+n-n_A} \right] \qquad (7.2)$$

Now the three ABCs become

$$n_A = \frac{\bar{n}_{c_1}\bar{n}_{c_2}+\varepsilon_b(\omega)}{\bar{n}_{c_1}+\bar{n}_{c_2}} \qquad \text{ABC1} \qquad (7.3a)$$

$$n_A = \frac{\bar{n}_{c_1}\bar{n}_{c_2}(\bar{n}_{c_1}+\bar{n}_{c_2})}{(\bar{n}_{c_1})^2+\bar{n}_{c_1}\bar{n}_{c_2}+(\bar{n}_{c_2})^2-\varepsilon_b(\omega)} \qquad \text{ABC2} \qquad (7.3b)$$

$$n_A = \bar{n}_{c_1}+\bar{n}_{c_2}-n_e \qquad \text{ABC3} \qquad (7.3c)$$

where $\bar{n}_{c_i}$ is defined by Eq. (6.6) and $\varepsilon_b(\omega)$ by Eq. (6.4).

By substituting each one of the equations in Eq. (7.3) into Eq. (7.2) and then substituting the latter into Eq. (7.1), the theoretical reflectivity for each ABC could be fitted to the corrected experimental

---

† A dead layer effect was not considered in Chap. VI, Sec. C since the experimental reflectivity did <u>not</u> show a spike at ω_L.(9)

reflectivity in Eq. (6.3). The results of this analysis are given in Figs. 7-1, 7-2, and 7-3. The best fit coefficients for each ABC is given in Table 7-1. Once again, all fitting was done between 20654.2cm^{-1} and 20482.1cm^{-1}. It can now be seen that the minimum of the theoretical reflectivity spectrum in the A-exciton resonance region has decreased for all ABCs when compared with Figs. 6-11 through 6-13. ABC1 in Fig. 7-1 fits the region around ω_L of the A-exciton extremely well. However, each ABC gives a relatively good fit.

D. GENERAL REMARKS

Although the theoretical external scattering cross section given in Eq. (4.53) differs in origin from that of BZB's scattering efficiency in which they considered the entire scattering process as a single unified event, it can be shown to be very similar if the deformation potential interaction kernel $\Gamma_o^{dp}(q)$ given in Eq. (4.18) is assumed to be independent of wavevector q. Choosing the exciton damping parameter Γ to be 10 cm^{-1} and setting $\Gamma_o^{dp}(q)$ = constant results in a theoretical external scattering cross section yielding plots for the three ABCs which are similar to Fig. 5 of the BZB paper.(1)

However, the q dependence in the expression for the deformation potential interaction kernel is essential for the comparison between theory (using ABC2) and experiment. This is illustrated in Fig. 7-4 where $\Gamma_o^{dp}(q)$ is assumed to be q-independent. The values in Table 6-1 are used once again with $\Gamma = 0.5\ \text{cm}^{-1}$. The data now seems to fall between ABC2 and ABC3. It is unclear which of these ABCs, if either, best describes the data. Hence, the q-factor in $\Gamma_o^{dp}(q)$ is extremely

FIG. 7-1 Non-linear least squares fit of the theoretical reflectivity expression using ABC1 plus a dead layer to the experimental reflectivity expression. Best fit coefficients are listed in Table 7-1. The theoretical curves are the solid lines while the experimental expression is illustrated by the data points. The arrows indicate the frequency region in which fitting was taking place. Reflectivity percentage is shown along the y-axis.

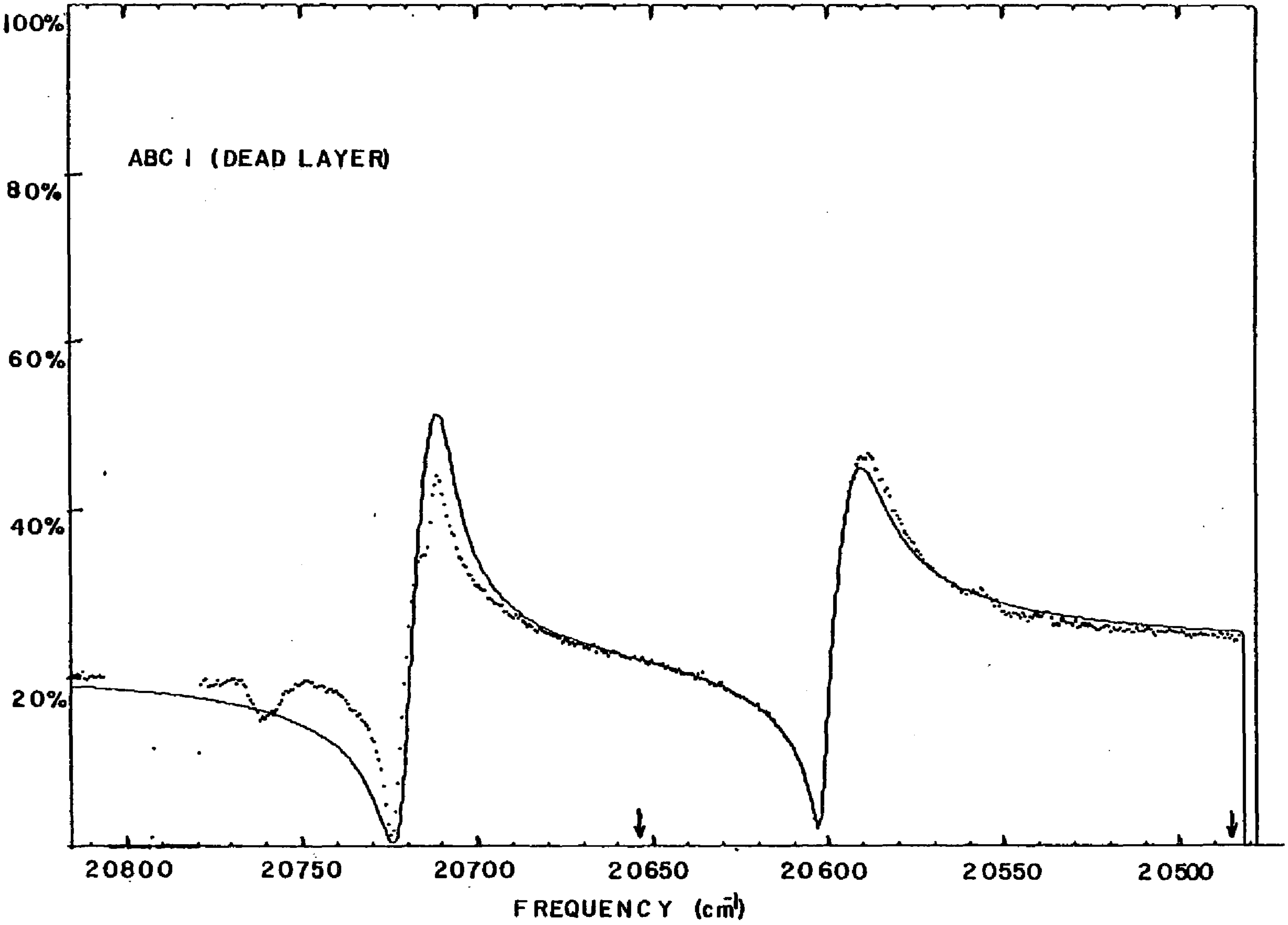
ABC I (DEAD LAYER)
100%
80%
60%
40%
20%
20800
20750
20700
20650
20600
20550
20500
FREQUENCY (cm⁻¹)

FIG. 7-2 Non-linear least squares fit of the theoretical reflectivity expression using ABC2 plus a dead layer to the experimental reflectivity expression. Best fit coefficients are listed in Table 7-1. The theoretical curves are the solid lines while the experimental expression is illustrated by the data points. The arrows indicate the frequency region in which fitting was taking place. Reflectivity percentage is shown along the y-axis.

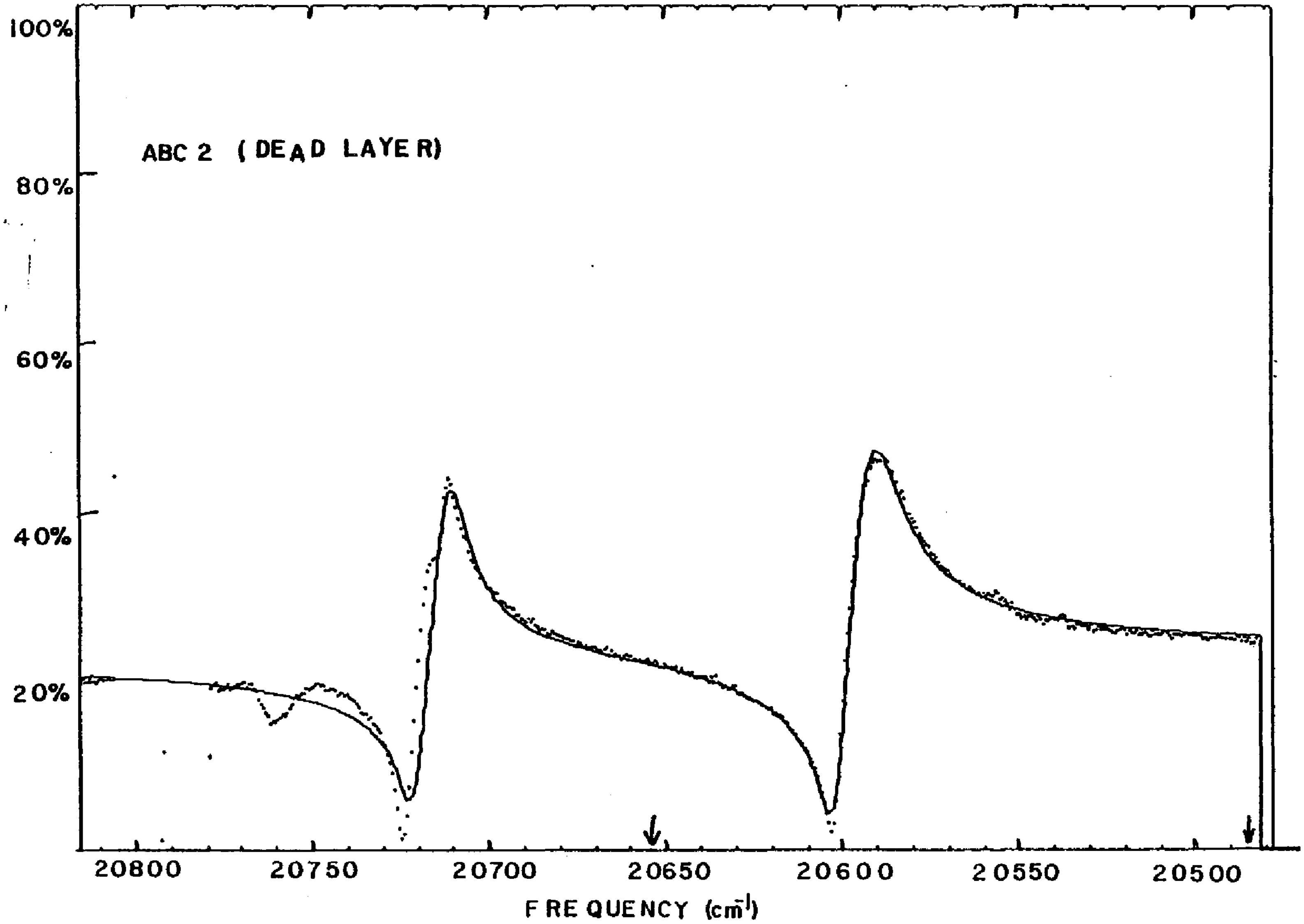
ABC 2 (DEAD LAYER)
100%
80%
60%
40%
20%
20800
20750
20700
20650
20600
20550
20500
FREQUENCY (cm⁻¹)

FIG. 7-3 Non-linear least squares fit of the theoretical reflectivity expression using ABC3 plus a dead layer to the experimental reflectivity expression. Best fit coefficients are listed in Table 7-1. The theoretical curves are the solid lines while the experimental expression is illustrated by the data points. The arrows indicate the frequency region in which fitting was taking place. Reflectivity percentage is shown along the y-axis.

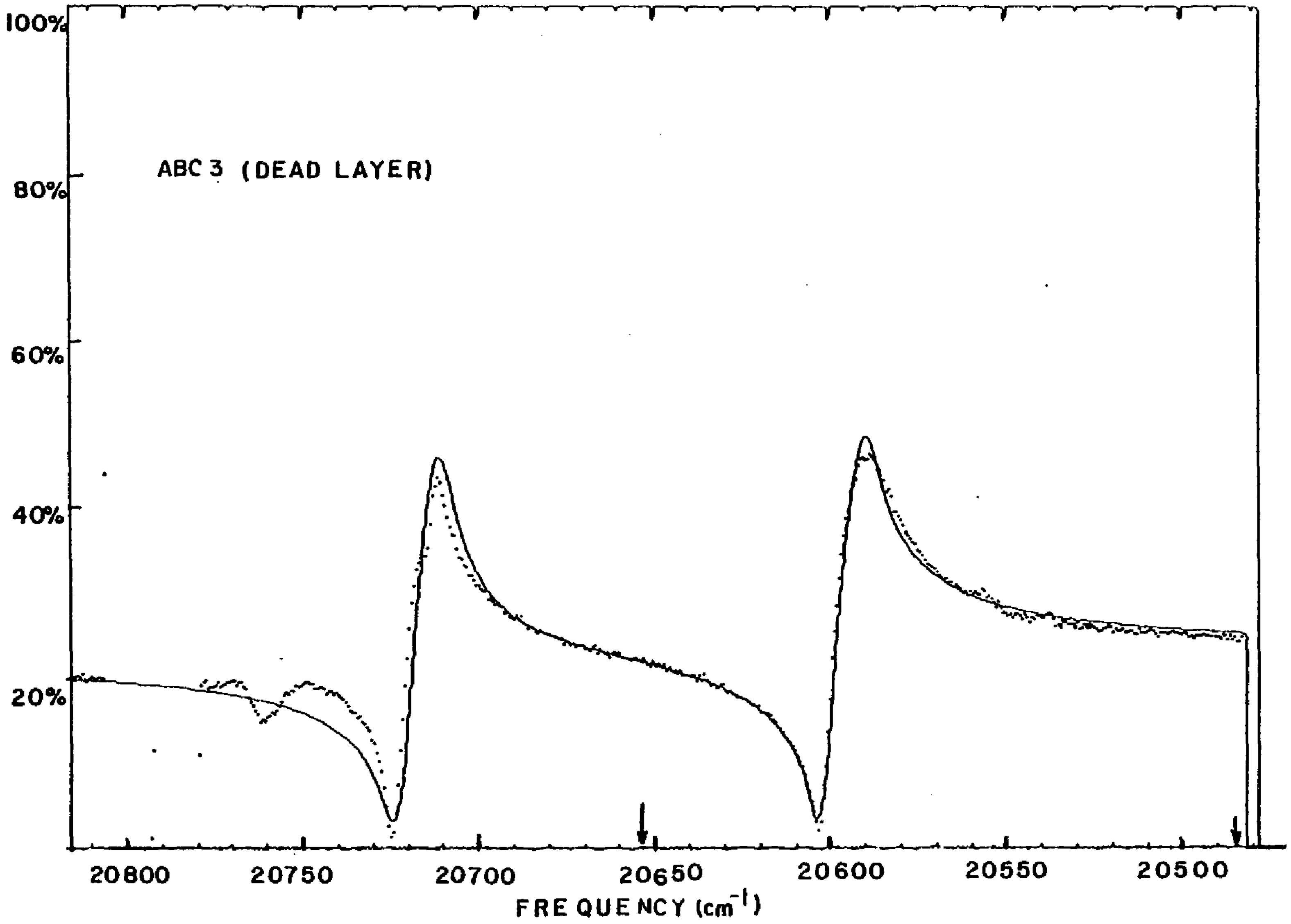
ABC 3 (DEAD LAYER)
100%
80%
60%
40%
20%
20800
20750
20700
20650
20600
20550
20500
FREQUENCY (cm⁻¹)

FIG. 7-4 Log_{10} comparison of the theoretical external scattering cross section for the Stokes LA (2-2') scattering for various ABCs with the $\log_{10}$ of the experimentally measured Brillouin intensities. The theoretical cross section was calculated here assuming the deformation potential interaction was a constant. Open squares (closed circles) represent the data which has been obtained with a FSR equal to 5.87 cm^{-1} (12.63 cm^{-1}).

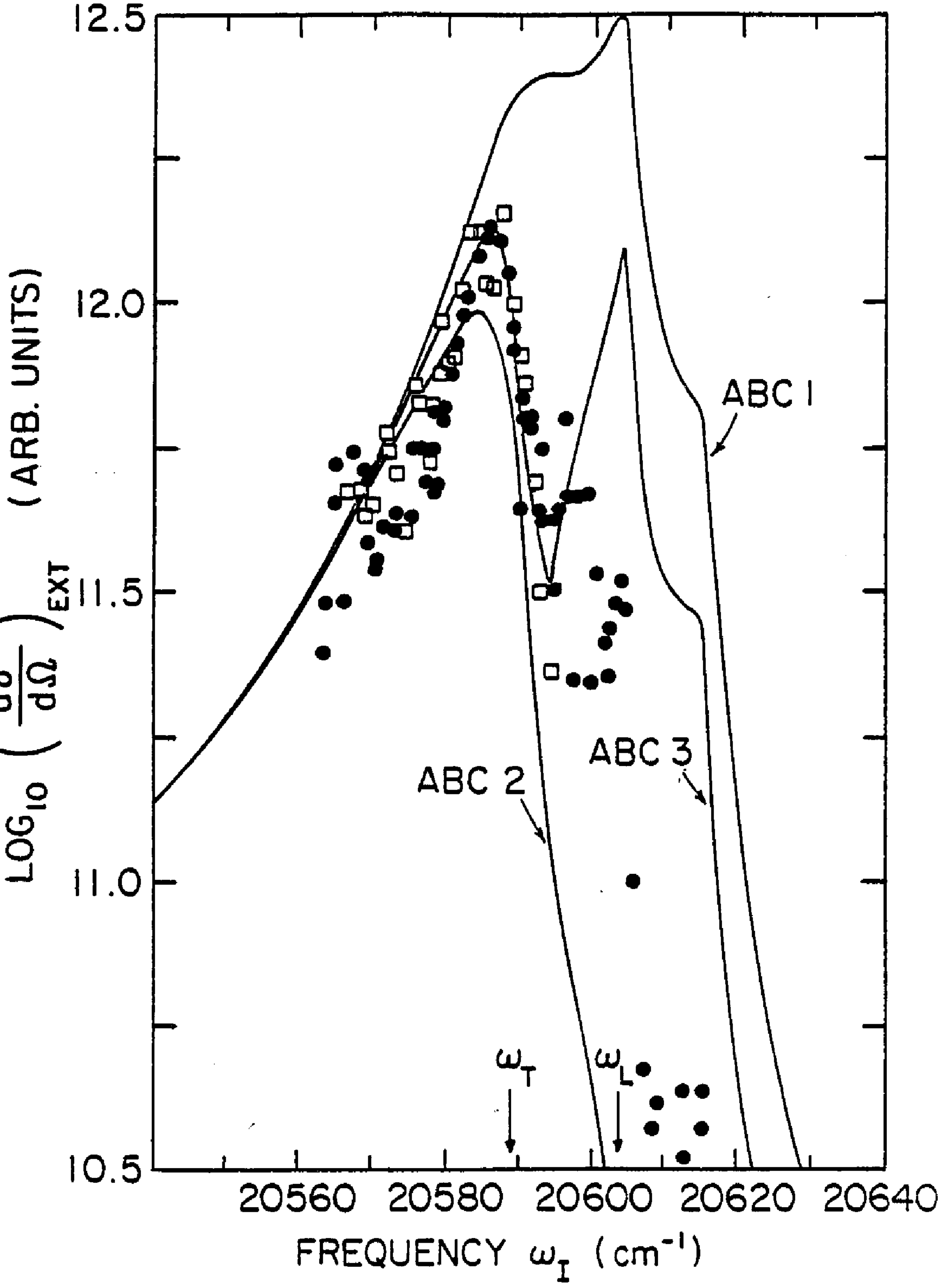

12.5
12.0
11.5
11.0
10.5
$\mathrm{LOG}_{10}\left(\frac{d\sigma}{d\Omega}\right)^{2'\leftarrow 2}_{\mathrm{EXT}}$ (ARB. UNITS)
20560
20580
20600
20620
20640
FREQUENCY ω_I (cm^{-1})
ABC 1
ABC 2
ABC 3
ω_T
ω_L

important and can not be ignored when comparing the scattering cross section (or efficiency) with Brillouin intensity data.

Several problems were present, both in the experiment and the calculation. As was discussed in Chap. IV, Sec. B, mode hops occurred on the average of one every five minutes. In addition, the data, at times, showed differences in the Rayleigh line intensities. Since several scans were usually recorded for each frequency of the dye laser, the records that showed no additional thin etalon modes and were of approximately equal Rayleigh intensity for both lines during the scan were the ones that were analyzed.

A serious problem arises when calculating the transmissivity. According to the analysis, when evaluating the sum of the transmissivities [Eqs. (4.47) and (4.48)] from vacuum to medium and the reflectivity [Eq. (4.49)], the result $T_1(\omega) + T_2(\omega) + R(\omega) = 1.0$ holds at all frequencies when $\Gamma = 0$ and when ABC1 and ABC2 are considered. But when Γ is increased, ABC1 gives a sum more than 1.0 and ABC2 yields a sum less than 1.0 in the frequency region between ω_T and ω_L. Both ABC1 and ABC2 yield a sum much more than one for $\Gamma \gtrsim \Gamma_c$ [see Eq. (4.27)] near ω_T. ABC3 does not yield the correct sum of 1.0 even when $\Gamma = 0$ since it does not satisfy energy conservation at the surface.(79) ABC3 yields the same strange behavior near ω_T for $\Gamma \gtrsim \Gamma_c$ as ABC1 and ABC2. Calculations of the transmissivity of mode-2 polaritons exhibit a sharp peak near ω_T for $\Gamma \gtrsim \Gamma_c$, the height of which goes well beyond 1.0. A similar problem exists for the transmissivity from medium to vacuum.

E. SUMMARY OF RESULTS AND POSSIBLE EXTENSIONS OF THE THEORETICAL CALCULATIONS AND EXPERIMENTAL INVESTIGATIONS

High resolution resonant Brillouin scattering was performed on a cadmium sulphide crystal. These RBS investigations were supplemented by reflectivity experiments conducted on the same sample. The results of all these experiments, when compared with theory, are summarized below:

The observation of both the inner and outer polariton branches participating in the scattering of acoustic phonons, has resulted in additional Brillouin shift measurements not seen in previous RBS experiments.(28,30) The accurate determination of these shifts, when compared with theory, have yielded revised values of the A-exciton parameters.

Broadening of both LA and TA (2-2') Stokes components was observed. Linewidth measurements have set an upper limit on the exciton damping parameter Γ of 0.5 cm^{-1} for $\omega \leq \omega_T$. However, for $\omega > \omega_T$, linewidths of both the LA and TA components increase monotonically with increasing frequency. This increase in linewidth may be associated with an increase in the number of decay channels available to the mode 2 polariton as its frequency is increased through the A-exciton resonance.

Brillouin intensity measurements of different one phonon scattering processes were compared with a theoretical external differential scattering cross section calculation which included a factorization procedure. The intensity measurements of the Stokes LA (2-2') and TA (2-2') components (which result from deformation potential and piezoelectric interactions respectively) were in much better agreement with the theoretical calculation including ABC2 than with either ABC1 or ABC3. However, the relative intensity of the Stokes LA (1-1') to the Stokes LA (2-2') was a factor of 100 smaller than predicted by the theory with any of the ABCs.

Comparisons between reflectivity measurements and theory showed that much better fits could be obtained when a dead layer was incorporated into the analysis, even though no reflectivity "spike" was observed near the ω_L frequency. With the dead layer included, a good fit between theory and experiment could be obtained for all the ABCs.

The reflectivity analysis suggests that in future calculations the dead layer effect should be incorporated into the theoretical external differential scattering cross section. Non-linear least squares fit between this revised theoretical cross section calculation and the measured Brillouin intensity data can then be made for each ABC. This type of analysis has already been done to some extent by Yu and Evangelisti.(29) These authors incorporated a lossy dead layer into their theory and, upon comparison with their measured data, found that ABC3 produced the best fit to the Stokes LA (2-2') components. However, their intensity measurements were obtained using a grating spectrometer which has a much lower resolution than the triple pass Fabry-Perot interferometer utilized in the RBS experiments discussed in this thesis, and were limited to the 2-2' Brillouin components.

Future experimental investigations which should be considered include (i) deconvolution of digitally recorded resonant Brillouin scattering spectra which would result in more accurate measurements of the Brillouin linewidth and intensity; (ii) extending the magnetic field experiments of Broser and Rosenzweig which were discussed in

Chap. I by utilizing Fabry-Perot interferometry. These experiments will be initiated in our laboratory by Mr. Lu and Professor Shigenari.

TABLE 7-1 BEST FIT VALUES FOR Γ, $\bar{\varepsilon}_b$, ℓ AND n RESULTING FROM THE REFLECTIVITY ANALYSIS FOR EACH OF THE THREE ABCs

	ABC1	ABC2	ABC3
Γ	0.582 cm^{-1}	6.36 cm^{-1}	3.765 cm^{-1}
$\bar{\varepsilon}_b$	8.788	7.46	7.414
ℓ	161.5 Å	148.3 Å	112.2 Å
n	1.92	2.68	2.83

APPENDIX

ANALYTIC EXPRESSION FOR THE ENERGY VELOCITY

It has been shown by several authors(74,79) that the energy density and the Poynting vector, when evaluated near an exciton resonance in a spatially dispersive medium, have both electromagnetic and mechanical contributions:

$$W = \frac{1}{8\pi}(\varepsilon_b E^2 + H^2) + W_{ex} \tag{A.1}$$

$$\vec{S} = \frac{c}{4\pi}(\vec{E} \times \vec{H}) + \vec{S}_{ex} \tag{A.2}$$

The first terms on the right hand side in Eqs. (A.1) and (A.2) are the normally defined electromagnetic energy density and Poynting vector while

$$\vec{S}_{ex} = \frac{-v^2}{\alpha_o \omega^2_o}\left[\dot{\vec{P}}_{ex} \times (\nabla \times \vec{P}_{ex}) + \dot{\vec{P}}_{ex}(\nabla \cdot \vec{P}_{ex})\right] \tag{A.3}$$

and

$$\begin{aligned} W_{ex} = \frac{1}{2\alpha_o\omega_o^2} & \left[(\dot{\vec{P}}_{ex})^2 + \omega_o^2\,(\vec{P}_{ex})^2\right. \\ & \left. + v^2(\nabla\cdot\vec{P}_{ex}) + v^2(\nabla\times\vec{P}_{ex})\right] \end{aligned} \tag{A.4}$$

are the respective mechanical (excitonic) contributions. Here $\vec{P}_{ex}$ is just the exciton part of the polarization. The equation of motion of $\vec{P}_{ex}$ is given in Eq. (1.5) in Chap. 1 with

$$v^2 \equiv \frac{\hbar\omega_o}{m^*} \tag{A.5}$$

Eqs. (A.1) to (A.4) can be shown to satisfy the energy balance equation

$$\int \vec{S}\cdot d\vec{\sigma} + \int \dot{W} dv + \frac{\Gamma}{\alpha_o\omega_o^2}\int (\dot{P}_{ex})^2 dv = 0 \tag{A.6}$$

The energy velocity is defined as

$$v_E = \frac{\bar{S}}{\bar{W}} \tag{A.7}$$

where $\bar{W}$ and $\bar{S}$ are the time average of the absolute value of the energy density and Poynting vector. As is well known, the electromagnetic contributions have the form$^{(62)}$

$$\bar{W}_{EM} = \frac{\varepsilon_b + n^2 + \kappa^2}{16\pi} \; |E|^2 \tag{A.8}$$

$$\bar{S}_{EM} = \frac{cn}{8\pi} \; |E|^2 \tag{A.9}$$

For transverse plane wave polariton modes ($\nabla \cdot \vec{P}_{ex} = 0$), the mechanical contributions become

$$\bar{W}_{ex} = \frac{1}{4\alpha_o \omega_o^2} \; \{\omega^2 + \omega_o^2 + \beta^2\omega^2(n^2+\kappa^2)\} \; |\chi_{ex}(\vec{k},\omega)|^2 \; |E|^2 \tag{A.10}$$

$$\bar{S}_{ex} = \frac{cn\omega^2\beta^2}{2\alpha_o\omega_o^2} \; |\chi_{ex}(\vec{k},\omega)|^2 \; |E|^2 \tag{A.11}$$

where Eq. 1.1 from Chap. I has been used to relate P_{ex} and E with

$$\chi_{ex}(k,\omega) = \frac{\alpha_o \omega_o^2}{\omega_o^2 + k^2v^2 - \omega^2 - i\omega\Gamma} \tag{A.12}$$

which is just Eq. (1.6) minus the background susceptibility term. Here, $\beta^2 = v^2/c^2$. Substituting Eq. (A.12) into the Eqs. (A.10) and (A.11) and then adding these expressions to Eqs. (A.8) and (A.9) yield

$$\bar{S} = \frac{cn}{8\pi} \; \frac{\Gamma}{\Gamma - 2\beta^2\omega n\kappa} \; |E|^2 \tag{A.13}$$

$$\bar{W} = \frac{n}{8\pi} \left[n + \frac{2\omega(1+\beta^2\kappa^2)\kappa}{\Gamma - 2\beta^2\omega n\kappa}\right] |E|^2 \tag{A.14}$$

Use has been made of the dispersion Eq. (4.25) via its real and imaginary parts in order to obtain the concise expressions for $\bar{S}$

and $\bar{W}$ above. Substitution of Eqs. (A.13) and (A.14) into (A.7) results in the analytic expression for the energy velocity of an exciton polariton mode

$$v_E = \frac{c}{n + \frac{2\omega\kappa}{\Gamma} + \frac{2\beta^2\omega\kappa}{\Gamma}\,(\kappa^2 - n^2)} \tag{A.15}$$

For $\beta = 0$, Eq. (A.15) becomes equal to the energy velocity expression derived by Loudon for an absorbing medium described by the simple classical dielectric model.

REFERENCES

1. W. Brenig, R. Zeyher and J. L. Birman, Phys. Rev. B 6, 4617 (1972).

2. D. L. Mills and E. Burstein, Rep. Prog. Phys. 37, 817 (1974).

3. J. J. Hopfield, J. of the Phys. Soc. of Japan 21, suppl. 77 (1966).

4. K. Huang, Proc. Roy. Soc. A 208, 352 (1951).

5. H. Poulet, Ann. Phys. Paris 10, 908 (1955).

6. U. Fano, Phys. Rev. 103, 1702 (1956).

7. J. J. Hopfield, Phys. Rev. 112, 1555 (1958).

8. S. I. Pekar, Sov. Phys. JETP 6, 785 (1958); Sov. Phys. JETP 34, 813 (1958).

9. J. J. Hopfield and D. G. Thomas, Phys. Rev. 132, 563 (1963).

10. B. Bendow, Polariton Theory of Resonance Raman Scattering in Solids in Springer Tracts in Modern Physics Vol. 82 (Springer, Berlin, 1978) p. 69.

11. R. G. Ulbrich and C. Weisbuch, Festkorperprobleme XVIII - Advances in Solid State Physics edited by J. Treusch, Braunschweig: Vieweg, (1978) p. 217.

12. P. Y. Yu, in: Light Scattering in Solids edited by J. L. Birman, H. Z. Cummins and K. K. Rebane (Plenum Press, New York, 1979) p. 143.

13. E. S. Koteles, in: Excitons edited by E. Rashba and M. Sturge (North-Holland Press, Amsterdam, 1982) p. 83.

14. A. S. Barker and R. Loudon, Rev. Mod. Phys. 44, 18 (1972).

15. An excellent review of this subject is given by J. L. Birman in: Excitons edited by E. Rashba and M. Sturge (North-Holland Press, Amsterdam, 1982) p. 27.

16. F. Evangelisti, A. Frova and F. Patella, Phys. Rev. B 10, 4253 (1974).

17. J. L. Birman and J. J. Sein, Phys. Rev. B 6, 2482 (1972); J. J. Sein, Phys. Letters 32A, 141 (1970).

18. A. A. Maradudin and D. L. Mills, Phys. Rev. B 7, 2787 (1973).

REFERENCES (Continued)

19. G. S. Agarwal, D. N. Pattanyak and E. Wolf, Phys. Rev. Lett. 27, 1022 (1971); Phys. Rev. B 8, 4768 (1973).

20. V. M. Agranovich and V. L. Ginzburg, *Spatial Dispersion in Crystal Optics and the Theory of Excitons*, (Wiley, New York, 1963) Chap. 3.

21. M. J. Frankel and J. L. Birman, Phys. Rev. B 13, 2587 (1976).

22. R. Zeyher, J. L. Birman and W. Brenig, Phys. Rev. B 6, 4613 (1972).

23. C. S. Ting, M. Frankel and J. L. Birman, Solid State Comm. 17, 1285 (1975).

24. R. G. Ulbrich and C. Weisbuch, Phys. Rev. Lett. 38, 865 (1977).

25. B. Sermage and G. Fishman, Phys. Rev. Lett. 43, 1043 (1979); Phys. Rev. B 23, 5107 (1981).

26. A. S. Pine, Phys. Rev. B 5, 3003 (1972).

27. R. H. Bruce and H. Z. Cummins, Phys. Rev. B 16, 4462 (1977).

28. G. Winterling and E. S. Koteles, Solid State Commun. 23, 95 (1977).

29. P. Y. Yu and F. Evangelisti, Solid State Commun. 27, 87 (1978).

30. G. Winterling, E. S. Koteles and M. Cardona, Phys. Rev. Lett. 39, 1286 (1977).

31. E. S. Koteles and G. Winterling, Phys. Rev. Lett. 44, 948 (1980).

32. P. Y. Yu and F. Evangelisti, Phys. Rev. Lett. 42, 1642 (1979).

33. I. Broser and M. Rosenzweig, Solid State Commun. 36, 1027 (1980).

34. C. Hermann and P. Y. Yu, Solid State Commun. 28, 313 (1978); Phys. Rev. B 21, 3675 (1980).

35. T. Goto and Y. Nishina, Solid State Commun. 31, 751 (1979).

36. C. Y. So, Ph.D. Thesis, University of Toronto, Toronto, 1981, unpublished.

37. R. W. Wyckoff; Crystal Structures (Interscience, New York, 1960) Vol. 1, p. 111.

38. G. F. Koster, J. O. Dimmock, R. G. Wheeler and H. Statz; Properties of the Thirty-Two Point Groups (M.I.T. Press, Cambridge, 1963).

39. J. L. Birman, Phys. Rev. 114, 1490 (1959).

40. Theoretical calculations for the normal mode frequencies have been performed by M. A. Nusimovici and J. L. Birman, Phys. Rev. 156, 925 (1967).

41. M. Balkanski, J. M. Besson and R. LeToullec in: Proceedings of the International Conference on Semiconductors, Paris (Academic Press Inc., New York, 1964) p. 1091. R. Marshall and S. S. Mitra, Phys. Rev. 134, A1019 (1964).

42. R. J. Collins, J. Appl. Phys. 30, 1135 (1959).

43. J. J. Hopfield, J. Phys. Chem. Solids 10, 110 (1959). K. Colbow, Phys. Rev. 141, 742 (1966).

44. B. Tell, T. C. Damen and S. P. S. Porto, Phys. Rev. 144, 771 (1966).

45. J. F. Nye, Physical Property of Crystals (Oxford: Claredon Press, 1957).

46. L. D. Landau and E. M. Lifshitz, Theory of Elasticity (Pergamon Press, New York, 1959).

47. H. Z. Cummins and P. E. Schoen in: Laser Handbook, Vol. 2 edited by Arecchi and Schultz (Dubois - North-Holland, Amsterdam, 1972) p. 1029.

48. A similar breakdown in selection rules has also been observed in resonant Raman scattering in cadmium sulphide. See R. M. Martin and T. C. Damen, Phys. Rev. Lett. 26, 86 (1971).

49. E. F. Gross, B. S. Razbirin and M. A. Iakobsen, Zh. Techn. Fiz. 27, 1149 (1957) [Translation: Soviet Phys. - Tech. Phys. 2, 1043 (1957)].

50. D. B. Dutton, Phys. Rev. 112, 785 (1958).

51. D. G. Thomas and J. J. Hopfield, Phys. Rev. 116, 573 (1959).

52. R. J. Elliot, Phys. Rev. 108, 1384 (1957).

REFERENCES (Continued)

53. J. J. Hopfield and D. G. Thomas, Phys. Rev. 122, 35 (1961).

54. R. C. Casella, Phys. Rev. Lett. 5, 371 (1960); Phys. Rev. 114, 1514 (1959).

55. G. D. Mahan and J. J. Hopfield, Phys. Rev. 135, A428 (1964).

56. K. Cho, Phys. Rev. B 14, 4463 (1976).

57. W. Hayes and R. Loudon: Scattering of Light by Crystals (WILEY - Interscience, New York, 1978) p. 336.

58. D. Berlincourt, H. Jaffe and L. R. Shiozawa, Phys. Rev. 129, 1009 (1963).

59. A. R. Huston, J. Appl. Phys. Suppl. 32, 2287 (1961).

60. G. Winterling and E. S. Koteles, in: Lattice Dynamics edited by M. Balkanski (Flammarion Sciences, Paris, 1978) p. 170.

61. K. Cho, in: Excitons edited by K. Cho (Springer-Verlag, New York, 1979).

62. R. Loudon, J. Phys. A: General Phys. 3, 233 (1970).

63. R. Loudon, J. Phys. C: Solid State Phys. 11, 403 (1978).

64. J. R. Sandercock, Phys. Rev. Lett. 28, 237 (1972).

65. J. S. Nkoma and R. Loudon, J. Phys. C. Solid State Phys: 8, 1950 (1975).

66. D. R. Tilley, J. Phys. C: Solid State Phys. 13, 781 (1980).

67. G. R. Fowles, Introduction to Modern Optics (Holt, Rinehart and Winston, New York, 1968).

68. K. H. Beckmann and B. Casper, Philips. Res. Repts. 20, 190 (1965).

69. R. J. Elliot, in: Polarons and Excitons edited by C. G. Kuper and G. D. Whitfield (Plenum Press, New York, 1963) p. 269.

70. E. Burstein, D. L. Mills, A. Pinczuk and S. Ushioda, Phys. Rev. Lett. 22, 348 (1969); ibid., 22, 913 (1969) (Erratum).

71. R. Loudon, Proc. R. Soc. A275, 218 (1963).

72. Y. Toyozawa, Prog. Theor. Phys., Suppl. 12, 111 (1959).

REFERENCES (Continued)

73. P. Y. Yu, in: *Excitons* edited by K. Cho (Springer-Verlag, New York, 1979) p. 211.

74. W. C. Tait, Phys. Rev. **B 5**, 648 (1972).

75. P. Y. Yu, Solid State Commun. **32**, 29 (1979).

76. A. Dienes, in: *Laser Applications to Optics and Spectroscopy* edited by S. F. Jacobs, M. Sargent III, J. F. Scott and M. O. Scully (Addison, Massachusetts, 1975).

77. J. R. Sandercock, in: *Proceedings of the Second International Conference on Light Scattering in Solids* edited by M. Balkanski (Flammarion, Paris, 1971) p. 9.

78. J. Wicksted, M. Matsushita and H. Z. Cummins, Solid State Commun. **38**, 777 (1981).

79. M. F. Bishop and A. A. Maradudin, Phys. Rev. **B 14**, 3384 (1976).

80. D. Gerlich, J. Phys. Chem. Solids, **28**, 2575 (1967).

81. D. W. Langer, R. N. Euwena, K. Era and T. Koda, Phys. Rev. **B 2**, 4005 (1970)

82. K. Cho, private communication.

83. E. J. Flynn and S. Geschwind, Bull. Am. Phys. Soc. **26**, 488 (1981).